

https://dspace.org/

Microwave-assisted synthesis of mn2po4f and application in rechargeable aqueous sodium-ion batteries

Nzimande, Nkosikhona Thabani Mphephethwa

2020

https://hdl.handle.net/10539/31516

Downloaded from a DSpace repository. https://dspace.org/

Microwave-Assisted Synthesis of Mn_2PO_4F and Application in Rechargeable Aqueous Sodium-ion Batteries



UNIVERSITY OF THE
WITWATERSRAND,
JOHANNESBURG

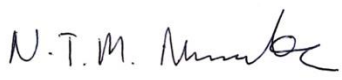
MSc dissertation by Nkosikhona Thabani Mphephethwa Nzimande
669123

Master of Science in the field of Chemistry

April 2020

Declaration

I declare that this dissertation, which is hereby submitted for a degree of Masters of Science in the Faculty of Science, School of Chemistry, University of the Witwatersrand, Johannesburg is my own unaided work and has not been submitted for examination at any institution.



(*signed)* Nkosikhona Nzimande

On this____20____ day of ____April____2020

Dedications

"The LORD is my shepherd; I shall not be in want. he restores my soul. He guides me in paths of righteousness for his name's sake. Even though I walk through the valley of the shadow of death, I will fear no evil, for you are with me; your rod and your staff, they comfort me"

Psalm 23

I dedicate my MSc research report to my beloved mother, sisters, brothers, friends, family, Ozoemena Research Group, CATMAT Research Group, the University of Witwatersrand and to the ever-growing scientific community.

"**K**eep your dreams alive. Understand to achieve anything requires faith and belief in yourself, vision, hard work, determination, and dedication. Remember all things are possible for those who believe"

Gail Devers

Acknowledgments

To Prof. Kenneth Ikechukwu Ozoemena a leader, pioneer, teacher and enthusiast in the field of energy research. I would like to express my wholehearted appreciation and respect for the time that you have taken to transfer your valuable knowledge and wisdom. Thank you for all the created opportunities and experiences that will forever remain close to my heart. As you have said recently, “You are tougher than tough”. Thank you.

The financial assistance from the National Research Foundation (NRF) is highly acknowledged. Thank you to the South African Nuclear Energy Corporation for accepting me as a visiting student and allowing me to use your equipment. I am thankful for NIMSA on assisting me with XPS and SEM analysis, your work is highly appreciated. I want to acknowledge the following individuals; Dr. Rudolph Erasmus on assistance with Raman, to Lerato Mokoloko for the late night TEM sessions, to Tsepo Molefe on helping me with BET, Aderemi Haruna for the constant support during synthesis and, electrochemical analysis, as well as sharing your immense wisdom. To the entire Ozoemena Research Group you are all highly appreciated for your constant motivation and sound advice.

Most importantly I am highly grateful for my lovely mother Miss BP Majola who has raised me up to the man I am today, without you I would not be where I am today, thank you for the sacrifices, the love, support, wisdom and many more of which I cannot mention. To my sisters Sindisiwe, Thabisile B. and Nokulunga T. Nzimande, thank you for all the support, love and the trust you have bestowed upon me, and to the rest of my family members, I appreciate you all for what you have done for me. To my best friends Lindokuhle Mtshali, Allan Mpofu, Thokozani Tsoari and Ethan Mudavanhu you guys are world class besties and to the rest of my friends including and not limited to Ludumo Magubane, Vuma Ntobela, Samukelo Nkosi, Morena Motsiri, Honore Paps, Palesa Dlamini, Boitumelo Tlhaole and Palesa Moloi. I appreciate the love and support; your friendship goes a long way. **THANK YOU**

Abstract

Sodium-ion batteries (SiBs) are set to be an alternative energy storage system to help ease the lithium-ion batteries (LiBs) market demands and availability. On the other hand, zinc-metal based anode aqueous batteries are paving the way in cost-effective, environmentally friendly, and non-toxic batteries. Here, we attempt to develop a zinc-metal based anode that uses sodium-ion as an electrolyte to form an aqueous battery that is mildly acidic. The material under investigation is the triplite (Mn_2PO_4F) also known as DiManganese fluorophosphate (MPF), it is a pinkish mineral that has no known reported electrochemical properties such as behaviour and performance. This is the main reason why it sparked our interest.

It is known that manganese-based battery materials suffer from these major obstacles: (i) Mn dissolution and (ii) Jahn teller distortions that lead to capacity fading and poor electrochemical performance. Knowing this, our purpose was to synthesize the triplite (Mn_2PO_4F) using microwave synthesis and use 2%-CeO_2 as a coating to help stabilizes the materials integrity and improve its electrochemical performance, also coat the material using 15% carbon (from citric acid) as an in-situ and ex-situ (from carbon black) coating agents to aid in improving the materials conductivity and electrochemical performance. This gave rise to four materials to be studied, MPF, MPF-CeO_2, MPF-CeO_2-CB and MPF-CeO_2-C (CB – carbon black, C – citric acid) and put into test using a T-type-cell as a battery.

To generate more detailed results, we decided to separate the results, with MPF and MPF-CeO_2 forming chapter four of the results sections and MPF-CeO_2-CB and MPF-CeO_2-C forming chapter five of the results section. In chapter four the results obtained for MPF at 0.1C had 2.2 $mAhg^{-1}$ maintaining 60% of its initial capacity with $\pm$ 99% CE and MPF-CeO_2 at 0.1C had 101.61 $mAhg^{-1}$ maintaining 90% of its initial capacity lasting only 400 cycles cycled at 5C with $\pm$ 99% CE. The analysis of the kinetic responses reveal that MPF at 1.0 C is seen to represent transitions between battery-type and pseudocapacitive reactions or process which are mainly kinetically dominated by diffusion-controlled process making it a good candidate for battery materials and MPF-CeO_2 electrochemical reactions are simultaneously controlled by

semi-infinite linear ionic diffusion and partially by surface-controlled capacitive behavior making it a much better battery material than MPF. Overall MPF-CeO_2 is the best material to be used in aqueous SiBs mainly due to the CeO_2 coating. Chapter five results obtained for MPF-CeO_2-CB at 0.1C. had 22.60 $mAhg^{-1}$ maintaining 64.24% of its initial capacity after 1000 cycles cycled at 1C with $\pm$ 99% CE and MPF-CeO_2-C at 0.1C had 195.16 $mAhg^{-1}$ maintaining 19.91% of its initial capacity after 100 cycles with $\pm$ 99% CE. The kinetic responses reveal that MPF-CeO_2-CB kinetically dominated by the diffusion-controlled process and MPF-CeO_2-C is simultaneously controlled by both ionic-diffusion and capacitive-control, this makes MPF-CeO_2-C the most desirable battery material for zinc-metal anode aqueous sodium-ion batteries, however, MPF-CeO_2-CB ex-situ coating is more stable than MPF-CeO_2-C over 100 cycles. Overall MPF-CeO_2 from chapter four and MPF-CeO_2—C from chapter 5 are the best suited materials to be used for rechargeable aqueous sodium-ion batteries.

Research Outputs

1. Attended two conferences in the year 2019 were I presented a poster on “Manganese oxide modified carbon-nanofiber-onion-like carbon composites as supercapacitor electrode”.

   Attended conferences:

   - Energy Storage and industry 4.0: “*Challenges and Prospects”* (ENSTIN 2019) held at KwaMaritane Bush Lodge, Pilanesburg National Park, South Africa, 31 July to 2nd August 2019.
   - International Society of Electrochemistry (ISE), 70th Annual meeting in Durban, South Africa, 4th to the 9th of August 2019

2. Currently working on an Invention Disclosure for my current MSc research project, hence why I did not present the data at the above mentioned conferences. The title has been submitted and is as follows “Microwave-assisted synthesis of manganese fluorophosphate ($Mn_2(PO_4)F$) for the development of high-voltage rechargeable aqueous metal ion batteries”. This is an Invention Disclosure being prepared for submission to the University of the Witwatersrand for provisional patent.

Table of Contents

CHAPTER ONE *15*

Introduction *15*

1.1 Motivation for Research **15**

1.1.1 Energy Landscape 15

1.1.2 Opportunities in Africa For Renewable Technologies, Energy Storage and Utilization of Resources 18

1.1.3 Problem Statement 22

1.2 Research and Objectives **22**

CHAPTER TWO *23*

Literature Review *23*

2.1 Introduction **23**

2.2 Electrical Energy Storage (EES) Systems **24**

2.3 Research in Energy Materials for Storage Systems **27**

2.4 Batteries **29**

2.4.1 Applications of Batteries 30

2.4.2 Battery Performance 35

2.4.3 Battery Engineering and Designs 43

2.4.4 Battery Technologies 48

2.5 Sodium-ion Batteries **54**

2.5.1 Sodium-Ion Anode Materials 58

2.5.2 Zinc Metal Anodes for SiBs 59

2.5.3 Sodium-Ion Battery (SiB) Electrolyte 61

2.6 Triplite (Mn_2PO_4F) As Energy Storage Material for SiBs **62**

2.7 Strategies for Improving Electrochemical Performance And Cyclability **65**

2.7.1 CeO_2 Coating 66

2.7.1 Carbon Coating 68

CHAPTER THREE *70*

Characterization and Techniques *70*

Importance of Surface Techniques **70**

3.1 Physical Characterization **71**

3.1.1 Powder X-Ray-Diffraction 71

3.1.2 Raman Spectroscopy 72

3.1.3 BET Surface Area Analysis 74

3.1.4 Scanning Electron Microscopy 77

3.1.5 Transmission Electron Microscopy 78

3.1.6 X-Ray Photoelectron Spectroscopy 79

3.2 Electroanalytical Techniques **83**

3.2.1 Cyclic Voltammetry 83

3.2.2 Chronopotentiometry 86

3.2.3 Electrochemical Impedance Spectroscopy (EIS) 87

CHAPTER FOUR *89*

Comparison of Pristine-MPF and MPF-CeO_2 ..... *89*

4.1 Methodology **89**
4.1.1 Synthesis of Pristine-MPF (Mn_2POF) 89
4.1.2 Synthesis of MPF-CeO_2 90
4.1.3 Characterization 92
4.1.4 Electrode Processing 93
4.1.5 Coin and T-type Cell Fabrication 93
4.2 Results and Discussion **95**
4.2.1 Materials characterization 95
4.2.2 Electrochemical Characterization 107
4.2.3 Application 120
4.3 Conclusion **122**
CHAPTER FIVE ***124***
Comparison of MPF-CeO_2-CB And MPF-CeO_2-C ***124***
5.1 Methodology **124**
5.1.1 Synthesis of MPF-CeO_2-CB 124
5.1.2 Synthesis of MPF-CeO_2-C 125
5.1.3 Characterization 127
5.1.4 Electrode Processing 127
5.1.5 Coin and T-type Cell Fabrication 127
5.2 Results and Discussion **128**
5.2.1 Materials Characterization 128
5.2.2 Electrochemical Characterization 142
5.2.3 Application 155
5.3 Conclusion **157**
Appendix **158**
References **161**

List of Figures

Chapter 1

Fig. 1. 1 | Future vision for energy infrastructure. Smart grid integrated with smart technologies.[93] 17
Fig. 1. 2 | Nasa Visible Earth, earth lights. Earth night areal map depicting Africa's lack of energy at night.[94] 18
Fig. 1. 3 | Photovoltaic power potential in the Sub-Saharan Africa (**a**)[95], Wind power classes surrounding Africa as potential energy resource (**b**)[96], Mapping Africa's natural resources (**c**).[97] 20
Fig. 1. 4 | Sources of energy generation in South Africa.[79] 21

Chapter 2

Fig. 2. 1 | Schematic of the two EES criteria. Adapted from ref [5] 25
Fig. 2. 2 | Schematic showing examples of EES. PHS (**a**), CAES (**b**), Flow battery (**c**), NaS battery (**d**), Flywheel system (**e**), Hydrogen fuel cell (**f**). [5] 26
Fig. 2. 3 | Battery applications and uses.[80] 30
Fig. 2. 4 | Medical devices. wireless implantable medical devices (a), portable electronic medical equipment (b).[81,82] 31
Fig. 2. 5 | Electric vehicles. Tesla electric vehicle (a), schematic of an electric vehicle with battery pack (b).[83,84] 32
Fig. 2. 6 | Grid energy storage. where batteries play a role in intermittent energy generation.[85] 34
Fig. 2. 7 | Capacity curves. The effect of discharge loads on battery discharge (**a**), The capacity for a battery discharged with a resistor calculated using area under voltage vs time curve (**b**), Using rectangular numerical integration for estimating battery capacity (**c**).[90] 38
Fig. 2. 8 | C-rate discharge profile. the discharge time (h) at various cell potentials (V) expressed in different C-rates.[90] 42
Fig. 2. 9 | Basic components of a battery.[90] 44
Fig. 2. 10 | Battery shapes and sizes. common cylindrical cells (a), button cells (b), coin cells (c) sizes with the diameter of the cells outlined at the bottom depicted as shaded circles.[90] 45
Fig. 2. 11 | Recent advances in the performance of secondary batteries. Specific energy ($Whkg^{-1}$) (**a**), Energy density (WhL^{-1}) (**b**).[90] 51
Fig. 2. 12 | Sodium-ion battery showing cathode, anode and electrolyte materials.[17] 57
Fig. 2. 13 | Zinc metal-anode batteries. Number of publications (a), Ragone plot of active materials used in Zinc-metal-anode based batteries (b), Schematic of a Zinc-metal-anode used in batteries (c). ref [26] 60
Fig. 2. 14 | Monoclinic space group C2/c of $Mn_2(PO_4)F$ (**a**), crystal structure of $Mn_2(PO_4)F$ (**b**).[35] 64

Fig. 2. 15 | Schematic of the electronic path length (L_e). Nanoparticles without coating (**a**), nanoparticles with carbon coating (**b**). ref.[37] 69

Chapter 3

Fig. 3. 1 | X-Ray diffraction diagram. Bragg diffraction.[86] 71
Fig. 3. 2 | Raman instrumentation. (**a**), **Raman mechanism of scattering** (**b**).[38]..73
Fig. 3. 3 | BET classification.[38].....76
Fig. 3. 4 | BET Hysteresis classification.[38].....76
Fig. 3. 5 | Scanning electron microscopy diagram.[87] 77
Fig. 3. 6 | Transmission electron microscopy diagram.[88] 78
Fig. 3. 7 | Schematic of an XPS equipment.[92] 80
Fig. 3. 8 | Schematic of an XPS equipment. (**a**) and Photo emission signal due to inelastic scattered signal which is different form the primary photoemission signal that give rise to the elemental peak (**b**).[45,92] 82
Fig. 3. 9 | Cyclic Voltammetry. Two methods used to report CV data (**a**), CV of reversible diffusion-controlled process (**b**), CV of quasi-reversible process (**c**), CV of irreversible process (**d**).[42].....85
Fig. 3. 10 | Potential curve. at constant current for reversible reduction of active species.[9] 86
Fig. 3. 11 | Typical equivalence circuit. for a cell with an impedance that is kinetically controlled, r_s = faradic component, C_{nf} = non-faradic capacitance, r_e = electrolyte resistance.[9] 87
Fig. 3. 12 | Impedance Spectroscopy. Cell impedance for a charge-transfer process with kinetic control (**a**), Cell impedance for a charge-transfer process with kinetic and diffusion-controlled process (**b**).[9].....88

Chapter 4

Fig. 4. 1 | Schematic representation of both preparation of pristine-MPF (4.1.1) and MPF-CeO_2 (4.1.2) 91
Fig. 4. 2 | Image showing finished products with their respective colours 91
Fig. 4. 3 | Coin cell. Traditional coin-cell assemble.[89].....93
Fig. 4. 4 | T-type-cell. T-type-cell basic schematic (**a**), T-type-cell detailed schematic representation (**b**).....94
Fig. 4. 5 | PXRD Pattern comparison of Triplite, MPF, MPF-CeO_2.....95
Fig. 4. 6 | SEM micrographs for MPF (a, b, c) and MPF-CeO_2 (d, e, f)……..97
Fig. 4.7 | TEM micrographs for MPF (**a, b, c**) and MPF-CeO_2 (**d, e, f**)……98
Fig. 4. 8 | Raman spectrum of MPF and MPF-CeO_2 (a), **Infrared spectrum** of MPF and MPF-CeO_2 (b)……...100
Fig. 4.9 | Brunauer-Emmett-Teller (BET) surface area analysis using N_2 adsorption-desorption studies, MPF (**a**) and MPF-CeO_2 (**b**) BET isotherm plots ……....103
Fig. 4.10 | X-Ray Photo spectroscopy (XPS) of MPF. Elemental ID and

quantification (**a**), Mn2p (**b**), P2p3 (**c**), O1s (**d**) and F1s (**e**)……104
Fig. 4. 11 | Electrochemical behaviours of MPF and MPF-CeO_2 batteries with 4 M $NaClO_4$ as electrolyte. Cyclic voltammograms (CVs) at 2.5 to 70 mVs^{-1} MPF (**a**), MPF-CeO_2 (**b**), CV comparison at 20 mVs^{-1} (**c**) and galvanostatic charge-discharge (GCD) curve comparison for both MPF and MPF-CeO_2 at 0.25 Ag^{-1} (**d**)……107
Fig. 4. 12 | Electrochemical performance of MPF and MPF-CeO_2 batteries with 4 M $NaClO_4$ as electrolyte. Charge/discharge curve comparison of MPF and MPF-CeO_2 coin-cell battery at 0.1C (**a**), Rate performance of MPF at 0.1, 0.2 and 0.5C using a T-cell battery (**b**) , Rate performance of MPF-CeO_2 from 0.1C to 6C using a T-cell battery (**c**), cyclic performance of MPF using T-cell battery (**d**), cyclic performance of MPF-CeO_2 using T-cell battery (**e**)……109
Fig. 4.13 | Electrochemical analysis of different kinetic responses. Active electrode material electrochemical CV curves for MPF (a) and MPF-CeO_2 (b) at sweep rates 2.5 to 20 mVs^{-1}, The dependence of parameter b on: MPF (c) and MPF-CeO_2 (d)……..114
Fig. 4.14 | Differentiating capacitive effect from diffusion-controlled process using Dunn's Method. CV curves with the capacitive contribution fraction depicted by the shaded area at sweep rate 2.5 mVs^{-1} MPF (a) and MPF-CeO_2 (b), Capacitive contribution bar chart at sweep rates 2.5, 5, 10 and 20 mVs^{-1} MPF (c) and MPF-CeO_2 (d)respectively……..……..116
Fig. 4.15 | Electrochemical impedance spectroscopy (EIS). MPF before cycling stability (**a**) and after cycling (**b**), MPF-CeO_2 before cycling stability (**c**) and after cycling (**d**)……...118
Fig. 4.16 | Application tests. MPF lasted for 02 mins:20.81 secs (**a**), MPF-CeO_2 lasted for 11 mins:07.80 secs (**b**)……120

Chapter 5

Fig. 5. 1 | Schematic representation of the preparation of MPF-CeO_2-CB (a, 5.1.1) and MPF-CeO_2-C (b, 5.1.2).....126
Fig. 5. 2 | Image showing finished products with their respective colours 127
Fig. 5. 3 | PXRD Pattern comparison of Triplite, MPF-CeO_2-CB, MPF-CeO_2-C....128
Fig. 5.4 | SEM micrographs of MPF-CeO_2-CB (**a-c**), MPF-CeO_2-C (**d-f**)…… ..130
Fig. 5.5 | TEM micrographs of MPF-CeO_2-CB (**a-f**), MPF-CeO_2-C (**g-j**)……132
Fig. 5.6 | Raman spectrum of MPF-CeO_2-CB and MPF-CeO_2-C (**a**), **Infrared spectrum** of MPFCeO_2-CB and MPF-CeO_2-C (**b**)……134
Fig. 5.7 | Brunauer-Emmett-Teller (BET) surface area analysis using N_2 adsorption-desorption studies, MPF-CeO_2-CB (**a**) and MPF-CeO_2C (**b**) BET isotherm plot……..……137
Fig. 5.8 | X-Ray Photo spectroscopy (XPS) of MPF-CeO_2-CB. XPS survey spectra (**a**), Mn2p (**b**), P2p3 (**c**), O1s (**d**) and F1s (**e**)……139
Fig. 5.9 | Electrochemical behaviours of MPF-CeO_2-CB and MPF-CeO_2-C batteries with 4 M $NaClO_4$ as electrolyte. Cyclic voltammograms (CVs) at 2.5 to 70 mVs^{-1} MPF-CeO_2-CB (**a**), MPF-CeO_2-C (**b**), CV comparison of MPF-CeO_2-CB and MPF-CeO_2-C at 20 mVs^{-1} (**c**) and galvanostatic charge-discharge (GCD) curve comparison for both MPF-CeO_2-CB and MPF-CeO_2-C at 0.25 Ag^{-1} (**d**)……142
Fig. 5.10 | Electrochemical performance of MPF-CeO_2-CB and MPF-CeO_2-C batteries with 4 M $NaClO_4$ as electrolyte. Charge/discharge curve comparison of

MPF-CeO_2-CB and MPF-CeO_2-C coin-cell battery at 0.1C (**a**), Rate performance of MPF CeO_2-CB at 0.1, 0.5, 0.5C and 1C using a T-cell battery (**b**) , Rate performance of MPF-CeO_2-C from 0.1C to 10C using a T-cell battery (**c**), cyclic performance of MPF-CeO_2-CB using T-cell battery (**d**), cyclic performance of MPF-CeO_2-C using T-cell battery (**e**)……..145
Fig. 5.11 | Electrochemical analysis of different kinetic responses. Active electrode material electrochemical CV curves for MPF-CeO_2-CB (a) and MPF-CeO_2-C (b) at sweep rates 2.5 to 20 mVs^{-1}, the dependence of parameter b on: MPF-CeO_2-CB (c) and MPF-CeO_2-CB (d)……148
Fig. 5.12 | Differentiating capacitive effect from diffusion-controlled process using Dunn's Method. CV curves with the capacitive contribution fraction depicted by the shaded area at sweep rate 2.5 mVs^{-1} MPF-CeO_2-CB (**a**) and MPF-CeO_2-C (**b**), Capacitive contribution bar chart at sweep rates 2.5, 5, 10 and 20 mVs^{-1} MPF-CeO_2-CB (**c**) and MPF-CeO_2-C (**d**) respectively……150
Fig. 5.13 | Electrochemical impedance spectroscopy (EIS). MPF-CeO_2-C before cycling stability (**a**) and after cycling (**b**), equivalent circuit (**c**)……152
Fig. 5.14 | Application tests. MPF-CeO_2-CB 11 mins:07.80 secs (**a**), MPF-CeO_2-C 35 mins:05.76 secs (**b**)……...155

List of tables

Chapter 2

Table 2. 1: Battery Terms, units, and abbreviations 35
Table 2. 2: C-rates and discharge time.....41
Table 2. 3: Conditions that make up a good electrolyte, anode and cathode material 47
Table 2. 4: Systems, Characteristics and Applications of Primary Batteries 49
Table 2. 5: Systems, Characteristics and Applications of Secondary Batteries.....52

Chapter 4

Table 4. 1 : Parameters obtained from XRD patterns, interplanar 97
Table 4. 2 : Raman Spectra.....101
Table 4. 3 : Tabulated summary of BET data 101
Table 4. 4 : MPF and MPF-CeO_2 Elemental ID and Quantification.....105
Table 4. 5 : MPF and MPF-CeO_2 Peak ID and Quantification 105
Table 4. 6 : Electrochemical impedance spectroscopy 118

Chapter 5

Table 5. 1 : Parameters obtained from XRD patterns, interplanar distance, lattice parameters and strain.....129
Table 5. 2 : Tabulated Raman data 136
Table 5. 3 : Tabulated summary of BET data 136
Table 5. 4 : MPF-CeO_2-CB and MPF-CeO_2-C Survey Elemental ID and Quantification 140
Table 5. 5 : MPF-CeO_2-CB and MPF-CeO_2-C Peak ID and Quantification 140
Table 5. 6 : Electrochemical Impedance spectroscopy 153

List of abbreviations

AC – Alternating current
ANSI – American National Standards Institute
BET – Brunauer-Emmett Teller
C – Citric acid
CB – Carbon black
CE – Coulombic efficiency
CST - Concentrated solar thermal
CPV -Concentrated solar thermal
CSP - Concentrated Solar Power
CAES - Capacitors, supercapacitors, Magnetic or current energy storage
CV – Cyclic Voltammetry
CPE – Constant Phase Element
CeO_2 - Cerium Oxide
EES – Electrical Energy Storage
EVs – Electrical Vehicles
EIS – Electrochemical Impedance Spectroscopy
EDLC – Electrochemical Double Layer Capacitance
FTIR – Fourier Transmission Infrared
GW – GigaWatts
IEC – International Electrotechnical Commission
KWh – KiloWatt hours
LA – Lead Acid
LiBs- Lithium-ion Batteries
LSE – Large-Scale energy
Mn – Manganese
MW – MegaWatts
MPF – Mn_2PO_4F and DiManganese fluorophosphate
PV – Photovoltaic
PHS - Capacitors, supercapacitors, Magnetic or current energy storage
RSA – Republic of South Africa
RE - renewable energy
SiBs – Sodium-ion batteries
SDGs - Sustainable Development Goals
SMES - Capacitors, supercapacitors, Magnetic or current energy storage
SEI – Solid Electrolyte Interface
SEM – Scanning Electron Microscopy
SMES – Capacitors, supercapacitors, magnetic storage
TWh – TearWatt hours
TES - Thermal energy storage
TEM – Transmission Electron Microscopy
XPS – X-Ray Photoelectron Spectroscopy
PXRD – X-Ray Diffraction
Zn – Zinc

CHAPTER ONE

Introduction

1.1 Motivation for Research

1.1.1 Energy Landscape

Modern society's energy needs are increasing every day, with the increasing population the energy needs might double in the next 30 years. The burning of fossil fuels poses a huge threat to our environment. Today, the world is setting various ambitious policies to protect the environment, for example, France announced its decision to ban sales of petrol and diesel cars by 2040. Access to electricity plays a crucial part in the development of modern-day to day needs, since it contributes to labor productivity and capital, encourages export and import of countries and creates employment. Furthermore, energy promotes healthcare services and education, improves socio-economic development, supports meeting domestic and residential needs and alleviates poverty. The United States (US) economy has estimated that

poor power supply causes productivity losses of about $400 billion each year.[1] Also, it is very apparent that we need to move closer towards achieving Goal 7: Affordable and clean energy which is one of the Sustainable Development Goals (SDGs) which also has an impact on the others ten goals including good health and well-being (Goal 3), zero hunger (Goal 2), no poverty (Goal 1), quality education (Goal 4), clean water and sanitation (Goal 6), decent work and economic growth (Goal 8), climate action (Goal 13), sustainable cities and communities (Goal 11), responsible consumption, production (Goal 12), Industry, innovation, infostructure (Goal 19). Making sustainable clean modern energy an indispensable factor for sustainable development.[2]

New energy technologies and climate change policies are propelling us towards a shift in the way we generate electricity to a more low-carbon friendly ecosystem. The current electricity generation contributes to 83% of global greenhouse gases.[5] A shift in energy generation requires a more robust combination of different distributed energy system models including, renewables, conventional fossil fuels, combined cycle gas turbines, and energy storage systems. Conventional fossil fuel power plants can generate capacities of 500 MW of energy and the shift towards renewables are at a point of reaching capacities of 100 MW (one-fifth of the capacity generated by fossil fuel power plants. Thus economies of scale have shifted investments towards larger RE systems to be built especially in the USA, China and Europe to strive towards achieving significant emission reduction in all sectors while maintaining sustainable, efficient low-cost electricity supply and industry output. To achieve low-carbon emissions, there has to be a strong shift away from utilizing fossil fuel use in industry, commercial, transport sector, residential and buildings which are the large consumers of electricity.[3] The future vision for energy infrastructure is to be able to integrate the grid with smart technologies which are renewable and green (**Fig. 1.1**).[2]

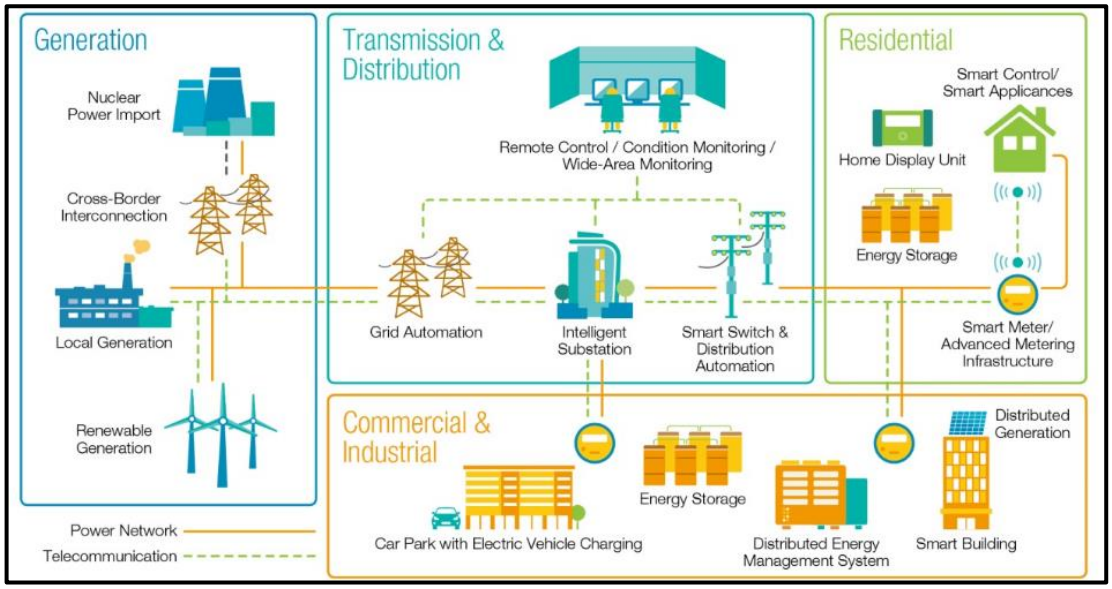


Fig. 1. 1 | Future vision for energy infrastructure. Smart grid integrated with smart technologies.[93]

Energy management and storage are becoming an important factor as many countries have decided to move towards the utilization of RE resources. This brings about the renewables intermittency challenge, which is the unplanned variations in power generation in solar, wave and wind capacity which are rooted in generating electricity only when there are reliable weather conditions, thus affecting energy supply and can only be circumvented by the introduction of reliable energy storage mechanisms. Energy storage technologies will play a crucial role in creating and ensuring an efficient clean energy future landscape, with over two billion people worldwide mostly living in third world countries do not have access to electricity, these technologies will step in securing continuous supply of power to the communities from a supply base both involving distributed and intermittent. [1]

1.1.2 Opportunities in Africa For Renewable Technologies, Energy Storage and Utilization of Resources

Approximately 13% of the global population (1 billion people) lack access to electricity and about 40% of the world population (3 billion people) do not have access to clean energy and still rely on fossil fuel forms of energy. It has been estimated that the African continent is projected to reach a population of 1.9 billion by the year 2050, therefore access to energy will be a major obstacle. To mitigate this issue, Africa needs to generate an additional 250 GW of new energy capacity between the years 2015 to 2030. Sub-Saharan Africa (SSA) with a current population of ~995 million is projected to be amongst the regions experiencing exponential growth in the world. Compared to other continents Africa is the most deprived continent with a population of a about ~1.3 billion (14%), with about ~ 600 million (65% of worlds population) which is more >50% of the world population living without access to electricity and half of the continents populations without access to electricity and Yet, Africa is energy-rich **Fig. 1.2** displays NASA's visible earth lights at night with the majority of Africa energy deprived.

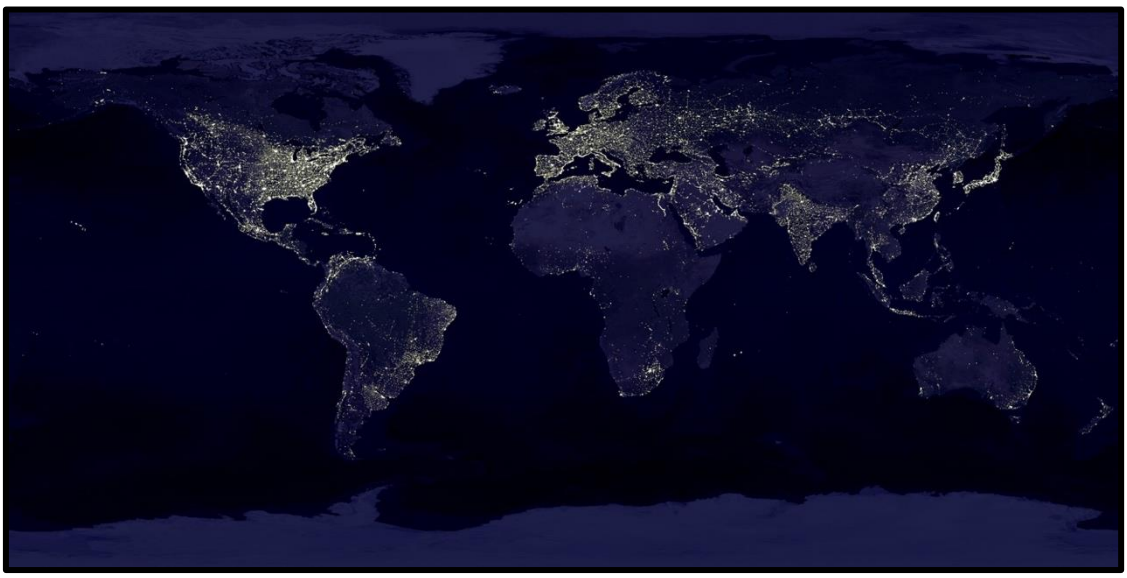


Fig. 1. 2 | Nasa Visible Earth, earth lights. Earth night areal map depicting Africa's lack of energy at night.[94]

Africa has a vast potential in both non-renewable and RE resources, which the largest potential in renewable resources of the continent are, solar, hydro, geothermal and wind, these offer an expansive opportunity for Africa to build a low-carbon energy technologies to provide clean energy for all, mitigate climate change and reduce emissions, inevitably accomplishing the SDGs. RE development in Africa is limited by the lack of investments in energy technologies to build infrastructure, lack of skilled manpower, insufficient RE policies and lack of maintenance services.[2] The renewable recourses are sufficient and meet regional energy needs, for non-renewable they include oil, coal, and gas that account for 7.5%, 1.1%, and 7.6% respectively of the world total reserves. Africa has a uniform distribution of sunlight, with more than 80% of Africa's landscape receiving nearly 200 kWh per square meter. The estimated Photovoltaic (PV) and Concentrated Solar Power CSP in Africa are at about 660 000 TWh and 470 000 TWh respectively (**Fig. 1.3** (**a**)). However, there are multiple challenges that CSP development that might be difficult to overcome in Africa, these include energy storage technologies for nighttime power generation and large amounts of water needed to cool CSP, which may increase the costs of production. With the potential to harness solar power it remains untapped, with a PV cumulative installed capacity of 1334 MW in 2014 with SA and Kenya leading the development. Wind energy potential in Africa has a high potential due to the coastal lines and high winds, with a total theoretical potential to produce 460 000 TWh of energy (**Fig. 1.3** (**b**)), as of 2015 about 1 GW of wind energy was installed in Africa.[2] It is time for Africa to learn towards its vast untapped resources (**Fig. 1.3** (**c**)) to ensure a better future for our generation.

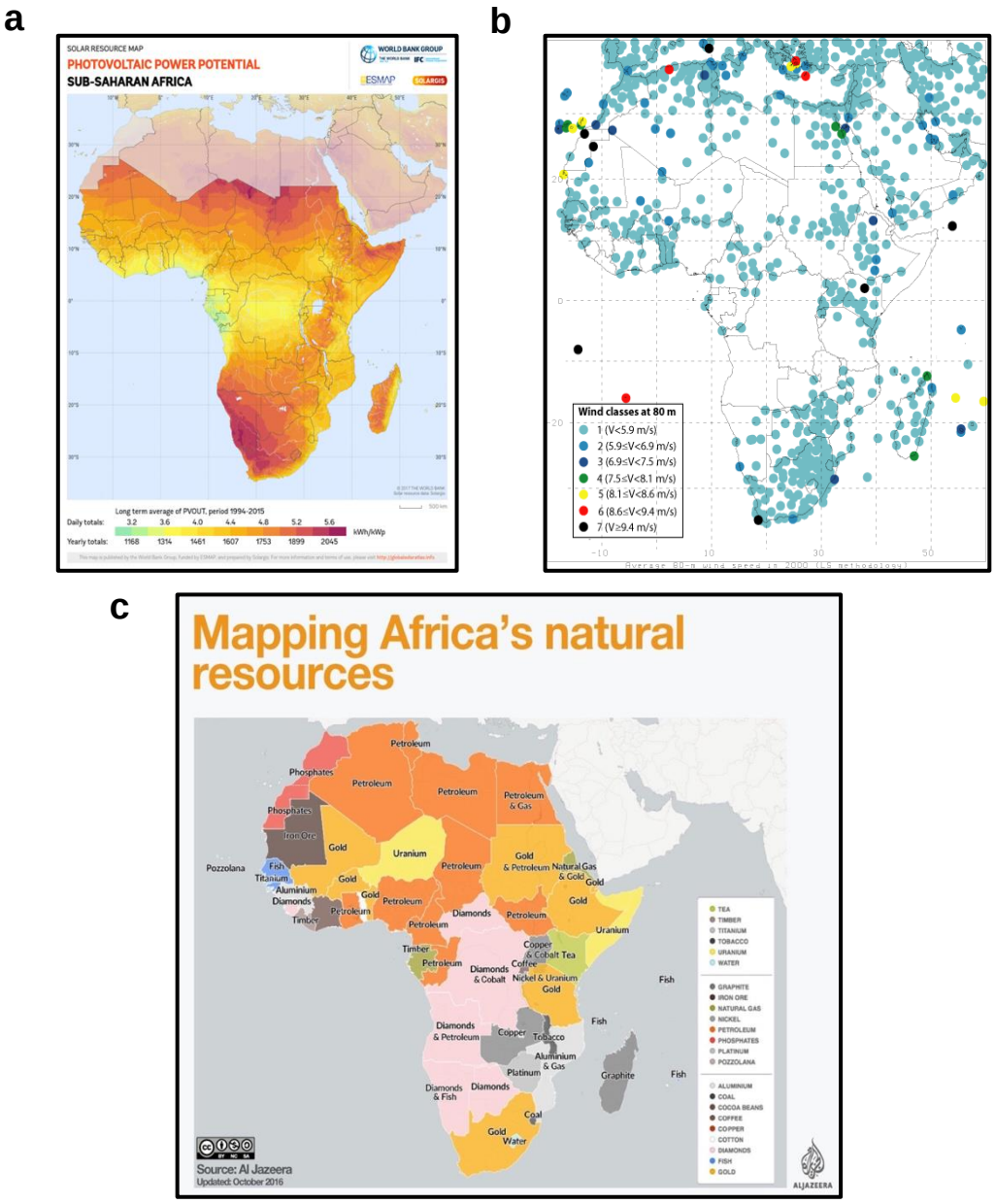


Fig. 1. 3 | Photovoltaic power potential in the Sub-Saharan Africa (**a**)[95], Wind power classes surrounding Africa as potential energy resource (**b**)[96], Mapping Africa's natural resources (**c**).[97]

South Africa which is located in the BRICS economy faces many economic growth problems, with energy being one of them, this is due to low capital investments in the electricity sector which has led to a shortage of capacity during peak hours, surging power prices, leading to an increase in the elasticity of demand and blackouts. The SA general Household survey in 2012 revealed that 1.45 million (11%) of RSA residence did not have access to electricity and 0.6 million (3.6%) of the residence accessed electricity illegally or informally, and the RSA government has identified the

lack of sustainable power as one of the major obstacles to economic growth. RSA generates 85% of its electricity from coal-powered plants with the highest levels of CO_2 emissions: of this percentage, 43% of industry demand, 28% of residential demand, 32% of commercial demand and agricultural, rely on coal produced electricity (**Fig. 1.4**). There has been a rapid change in RSA and the government has committed to investing $50 billion to accelerate the growth in energy power, switching from burning fossil fuels to clean and renewable energy and plans to reduce the countries emissions by 42% by 2025. [4]

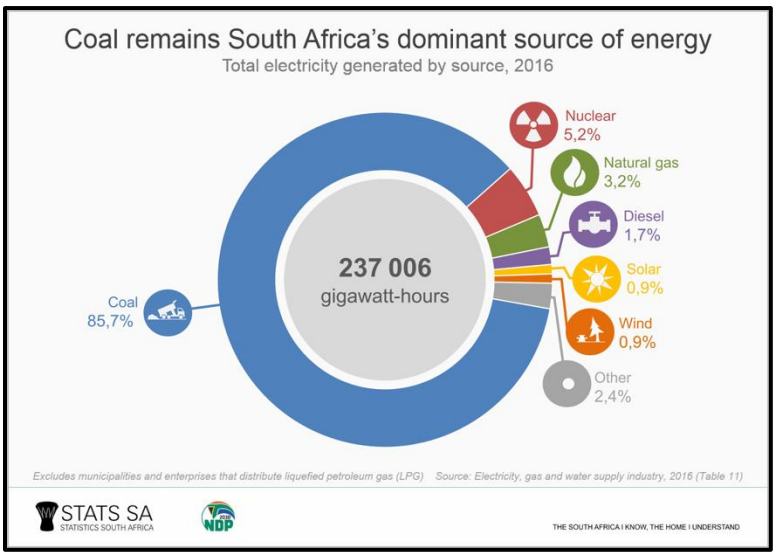


Fig. 1. 4 | Sources of energy generation in South Africa.[79]

1.1.3 Problem Statement

As stated from the abstract that sodium-ion batteries (SiBs) are set to be an alternative energy storage system to help ease the lithium-ion batteries (LiBs) market demands. Zinc-metal based anode aqueous batteries are paving the way in cost-effective, environmentally friendly, and non-toxic batteries. Here, we attempt to develop a zinc-metal based anode that uses sodium-ion as an electrolyte to form an aqueous battery that is mildly acidic. The dissertation will be investigating the DiManganese Fluorophosphate (MPF) material characteristics, electrochemical behaviour and performance. There is no known thorough material characterization and electrochemical research work that has been done on this material. The aim will be on strategies for improving electrochemical performance and cyclability of the material. The main problem to be interrogated is the cathode dissolution of manganese Mn^{2+} by utilizing surface coating of CeO_2 and carbon materials.

1.2 Research and Objectives

- Synthesize MPF, MPF-CeO_2, MPF-CeO_2-CB, and MPF-CeO_2-C using microwave synthesis as described by Ozoemena group.[39,40,41,42,43]

- PerformCeO_2 coating on MPF to improve stability, elevate Jahn Teller distortions and prevent undesirable oxygen evolution

- Perform in-situ carbon coating using citric acid and ex-situ carbon coating using carbon black to help improve electrical conductivity

- Perform Materials characterization using XRD, SEM, TEM, Raman, FTIR, and BET

- Investigate and interrogate the electrochemical behavior and performance which will be new insight information concerning this type of material

CHAPTER TWO

Literature Review

2.1 Introduction

The purpose of this chapter is to provide a literature overview that motivates the purpose of choosing this specific research. The introduction will focus on the electrical energy storage systems and their importance and classification followed by a brief insight on research in energy materials for storage systems. A short battery introduction encapsulating the different applications of batteries, battery performance, battery engineering and designs, the difference between primary and secondary batteries. A short introduction to sodium-ion batteries including its anode materials, electrolyte which will form a foundation to the introduction of the Triplite (MPF) mineral as an energy storage material for sodium-ion batteries. We will then highlight strategies for improving electrical performance and cyclability of the material which will lead to the main aim of this dissertation to investigation the materials characteristics, electrochemical behaviour and performance as a sodium-ion battery.

2.2 Electrical Energy Storage (EES) Systems

EES operate by converting electrical energy from a power system into a form that can be stored, which can thus, convert the energy stored back to electrical energy. Such systems enable electricity to be produced at low demand, at use of intermittent energy to be used at peak hours or high demand or when no other generation means are available. EES has multiple applications including, immobile energy storage, portable devices, and electric vehicles. EES systems date back in the early 20th century and power stations had to be shut down overnight, at this point Utility companies recognized the importance of flexibility that energy storage provides. The growth of RE sources as a means to supply electricity combined with more strict environmental requirements makes energy storage a more lucrative cost reduction. [5]

EES are urgently needed for conventional electricity generation since industries have little to no storage facilities. EES allows for self-generated energy production separated from its supply or purchased at will. They can increase the overall efficiency of thermal power sources while reducing harmful emissions. The energy resources system is changing to becoming a mixture of centralized and distributed sub-systems and EES will come in to compensate for power flexibility and provide an uninterrupted power supply in case there is a voltage drop in such a distributed network. EES can offer solutions in dealing with the unpredictability of intermittent renewable resources and their surplus output of energy could be stored during the periods when renewable generation surpasses demand and can be used when the generation of energy required is lower than the load.[5]

EES falls into two categories (**Fig. 2.1)**, one being high power quality and reliability and the other being energy management. SMES, flywheel and batteries fall under power quality and reliability whilst Potential energy storage (PHS), Compressed Air energy storage system (CAES), Large-scale battery, fuel cell, solar fuel and thermal energy storage (TES) fall under energy management. Another form of classifying energy technologies for electricity is in terms of storage as follows (**Fig. 2.2**):[5]

(1) *Mechanical energy storage*

i. Potential energy storage (PHS and CAES)
ii. Kinetic energy storage (flywheels)

(2) *Thermal energy storage*

i. High-temperature energy storage (heat systems and latent heat systems)
ii. Low-temperature energy storage (cryogenic energy storage, aquiferous cold energy storage)

(3) *Electrical energy storage*

i. Magnetic or current energy storage (SMES)
ii. Electrostatic energy storage (capacitors and supercapacitors)

(4) *Chemical energy storage*

i. Chemical energy storage (Fuel cells)
ii. Thermochemical energy storage (solar hydrogen, etc)
iii. Electrochemical energy storage (batteries such as lead-acid, lithium-ion, flow batteries, etc)

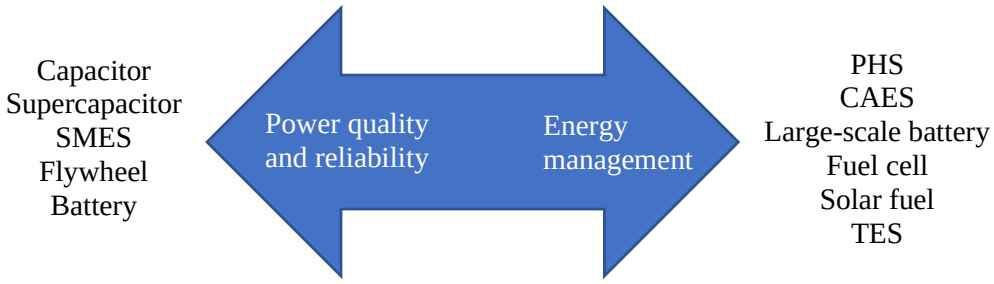


Fig. 2. 1 | Schematic of the two EES criteria. Adapted from ref [5]

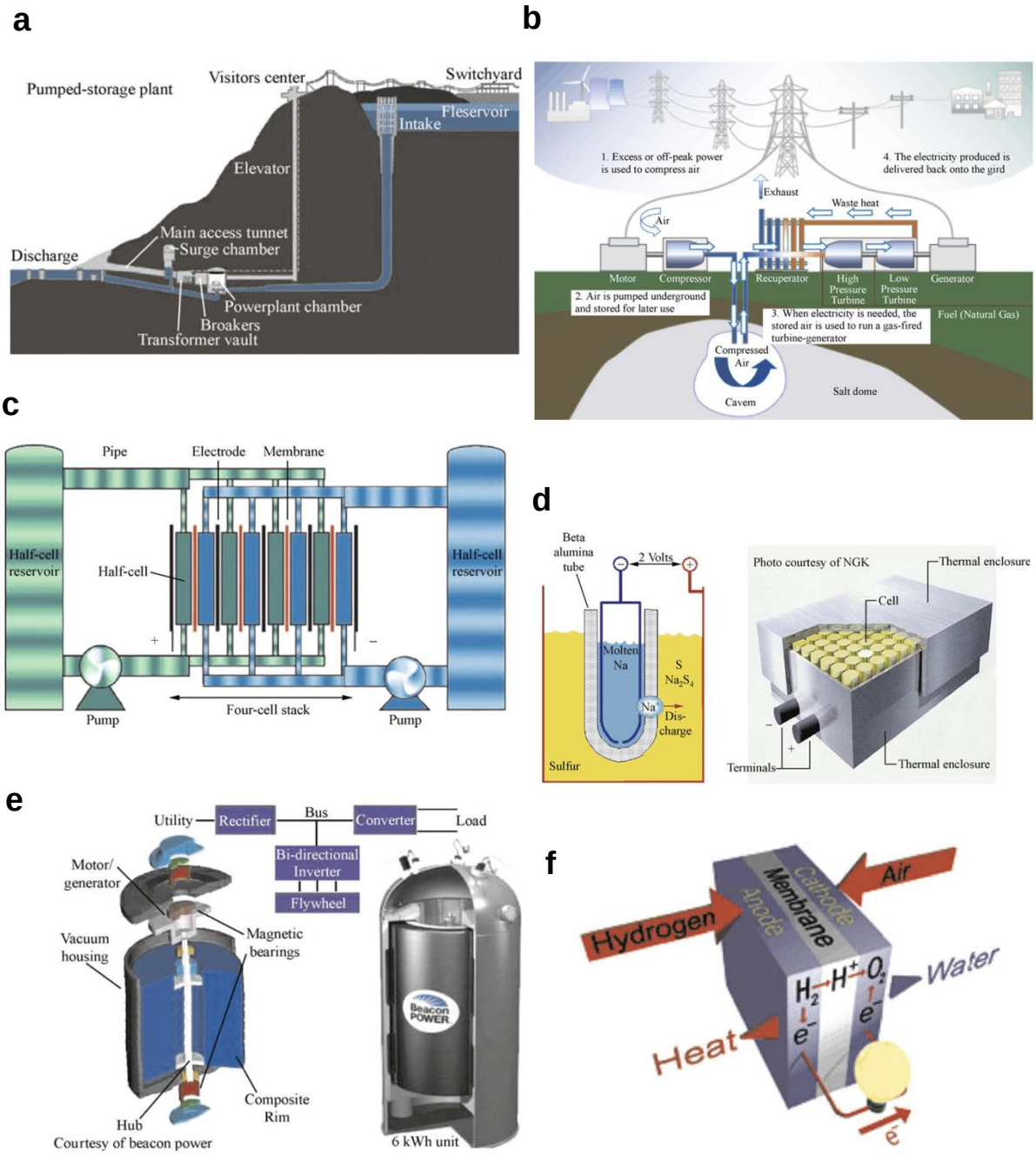


Fig. 2. 2 | Schematic showing examples of EES. PHS (**a**), CAES (**b**), Flow battery (**c**), NaS battery (**d**), Flywheel system (**e**), Hydrogen fuel cell (**f**). [5]

2.3 Research in Energy Materials for Storage Systems

Energy and materials have a synergistic relationship, materials can produce energy or can be converted and allow energy to be transferred into useful forms. Some materials are naturally occurring and can release energy through chemical and nuclear reactions, and these are known as fossil fuel form of materials which can be extracted from the ground and are burnt in the form of heat to produce energy. Then there are engineered materials that convert energy available energy into useful forms, for example, materials developed for batteries that store and deliver energy when needed, materials used to turn turbine blades which are made out of fiber-reinforced plastic that transform wind energy to electrical and mechanical energy. Over the past few centuries, mankind has relied on using affordable energy mainly from fossil fuels which has enabled economies to grow and of which are still growing at a rapid pace as the world's population increases, so does our basic needs to solve problems, thus large amounts of energy has to be generated to meet our demands. New resources have to be harnessed and the existing ones to be improved, adding to this problem, sustainable power generation is a major concern, managing waste, reduction of greenhouse gas emissions and pollution still need further attention. The question is, how can materials research address these obstacles?[6]

Currently, most research has focused on the applications of energy tackling the largest market the smart grid utility, it includes off-grid applications, consumers of renewable generation (Wind, etc.), distribution and community stations. The fundamental key component in these applications is smart energy storage and currently, the most widely used technology is the LA battery which takes up 60% of the total battery market because of their potential to provide high current at a relatively low price. Although Li-ion batteries have enticed a growing interest, lead-acid batteries still have a larger portion on the market share price as most used batteries on the energy storage market. The reason why lead-acid batteries lead the market, most other technologies are priced at a higher rate, therefore affecting the overall total system cost. However, LA batteries are not an ideal and reliable technology, due to their short

cycle life, suffer from poor charge/discharge capabilities, have environmental concerns and poor recyclability. This very problem encourages the research community to develop novel batteries that are low-cost, sustainable, environmentally friendly and recyclable. If such technologies were to be developed, there will be a strong market attraction and in the future may lead to grid-level applications.[7]

EES has been a hot topic of discussion in the past few years for both automotive (transportation) and the grid (immobile storage) applications as emerging markets such as portable/consumer electronics (e.g., laptop, smartphones, and tablets) and transportation (which include, hybrid electric vehicles (HEVs), full electric vehicles (EVs), and plug-in hybrid electric vehicles (PHEVs)) constitute an increase in the demand for electrical energy storage devices with high energy and power densities.[8] Therefore, materials science and materials engineering plays a major key role in developing technologies to circumvent this issue, however, energy storage is also a systems problem and faces many other challenges which include:[7]

(1) Development of new and innovative materials, materials electrochemistry and electrolytes are needed which can dramatically boost the compatibility and systems performances
(2) Reliability and safety
(3) Analysis and pure understanding of energy markets and economics is required in order to guide technology integration of energy technologies for different applications
(4) The need for sustainable, low-cost and environmentally friendly energy technologies
(5) Novel and inventive designs and architecture must be developed to reduce the system maintenance costs

2.4 Batteries

A Battery is an electrochemical device that converts chemical energy from its active material into electrical energy by an electrochemical redox reaction (oxidation-reduction). For a battery to be rechargeable, the reverse of this process occurs which involves the transfer of electrons from one material to another through an external circuit. It has been 200 years since the battery was first invented by Alessandro Volta followed by his letter delivered to the Royal Society of London in 1800 signifying innovative leaps in both science and technology breakthroughs. Before the battery was made known, electrical phenomena had been studied using electrostatic sources such as friction or harvested from natural sources, like lightning. In this case, the Leyden jar was invented a type of capacitor developed to store electrical energy to be utilized later, unfortunately, the energy produced from such devices can only be delivered in short bursts. Thus a more sustainable energy storage devices as needed.[9]

The introduction of storing electrochemical energy to electrical energy open doors to many forms of techniques such as new materials research, assembling the chemical right substances and a new way of producing electricity was available to everyone. The first batteries were used to study electricity and electrochemistry, many thanks go to Michael Faraday who advanced the knowledge of electrochemical reactions. Within a few years of these discoveries, batteries were developed and commercialized to provide electricity for applications such as telegraphs, railway signals and battery installations which proved electrical power just before the invention of the electrical generator. To date, some of the batteries developed in the nineteenth and early twentieth centuries are still being utilized especially nickel-cadmium, lead-acid and zinc-carbon batteries. As we lean/edge closer to the 4^{th} industrial revolution most technologies will be enabled by batteries including laptops, electric vehicles, cellular phones, and implantable pacemakers. In this chapter, the aim is to introduce you to various battery applications, engineering designs, performance, and technologies.[9]

2.4.1 Applications of Batteries

Every day we encounter devices that require batteries and are unplugged from the electrical energy distribution grid **Fig. 2.3** The purpose is to outline a few important applications such as:

- Medical devices
- Electric vehicles
- Portable consumer electronic devices
- Space
- LSE storage
- Military

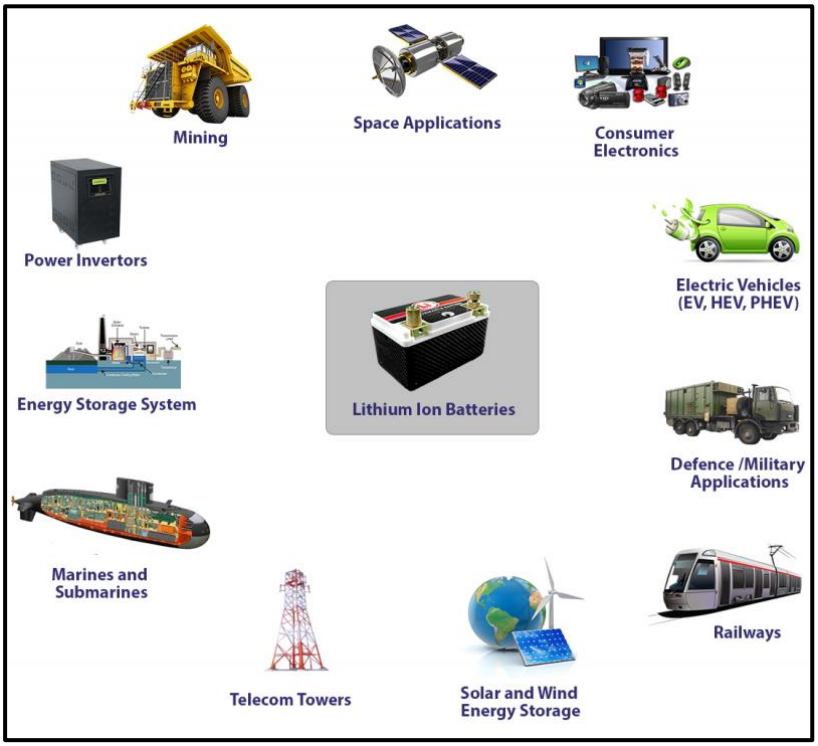


Fig. 2. 3 | Battery applications and uses.[80]

Medical Devices

These include implantable devices such as pacemakers, hearing aids, neurostimulators, cardiac defibrillators, and other portable electronic medical equipment **Fig. 2.4** Implantable pacemaker and cardiac defibrillators are devices implanted in the chest that apply an electrical signal to the heart tissue to aid the hearts beating pattern. Pacemakers batteries consist of lithium-iodine (Li/I_2) which deliver high-energy-density but low-power output, while defibrillators require batteries that are a combination of high-energy and high-power. Hearing aids are placed outside of the body, because they operate on zinc-air batteries offering high-energy-density lasting about a month, however rechargeable batteries using lithium metal and nickel-metal hydride (NiMH) have been introduced extending the duration. Neurostimulators are similar to pacemakers but deliver an electrical signal to the nerve tissue, these devices are available for neuro related applications such as spinal cord stimulation for treatment of deep depression to help suppress symptoms of Parkinson's disease.[90]

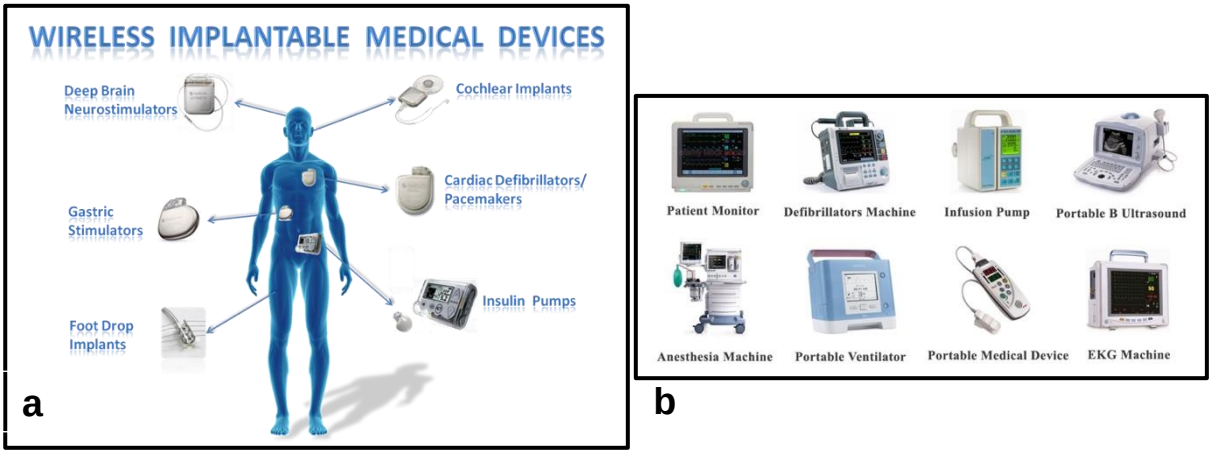


Fig. 2. 4 | Medical devices. wireless implantable medical devices (a), portable electronic medical equipment (b).[81,82]

Electric Vehicles

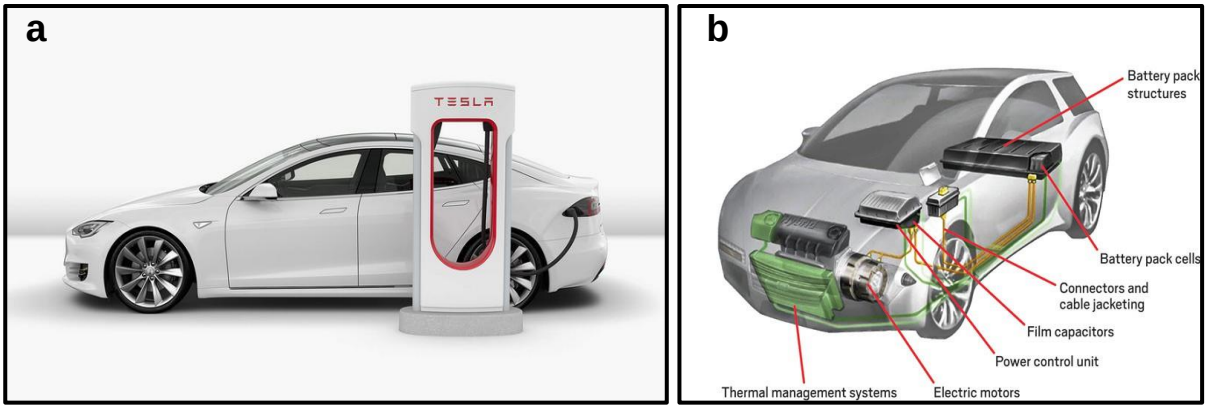


Fig. 2. 5 | Electric vehicles. Tesla electric vehicle (a), schematic of an electric vehicle with battery pack (b).[83,84]

Electric vehicles (EVs) as shown in **Fig. 2.5,** were first invented in the 1830s by Robert Anderson, which have become a necessity to minimize our global footprint and promote a green economy. To date battery powered vehicles include, cars, buses, trucks, trains forklifts and wheelchairs, thanks to companies like Tesla who have managed to pave the way forward offering affordable electric vehicles with about 500 km range. Currently Li-ion batteries are being developed for EVs although larger range and peak powers of 50 kilowatts are needed.[90]

Portable Consumer Electronic Devices

Modern day devices depend on the power requirements of the device and how it is utilized. Some devices use primary batteries which are designed to be used once and thereafter discarded. Some use secondary batteries that can be recharged to restore its energy and these devices are used frequently, requiring very high-power for extend periods of time. Factors such as size, weight and cost of the battery affect consumer electronics. As frequency use of such devices increases leads to high-demands in power loads and thus rechargeable batteries become more lucrative, such devices are supported by lithium-ion and nickel-cadmium batteries. [90]

Space

Batteries play a significant role in space exploration especially when it comes to satellites when they enter the earth's shadow, thus having their solar panels facing away from the sun. LiBs have been employed due to their lighter weight, to note it is also expensive to replace or fix satellites in earth orbit, therefore batteries should have higher energy densities and long-life spans. In 2004 NASA employed a lithium-ion battery for Mars exploration, which is still functioning despite heavy weather conditions on the planet.[90]

Large Scale Energy Storage

The introduction of LSE storage was first implemented in the 19th century using lead-acid batteries, over the years from the steam engines, the motor batteries have had a fair share of improvement alongside these technologies and called upon as a temporary source of energy when needed. Today batteries have been used in energy management such as peak shaving and load leveling storing energy during the day when demand is low then using it when demand is high. Also, clean energy generation such as solar and wind demand energy storage **Fig. 2.6** to allow smooth combination with distributed or centralized power generation providing backup power, improve the safety and economy of the distribution network thus the user can cut cost and choose between grid or renewable, also providing a means of making income through extra energy stored.[10,90]

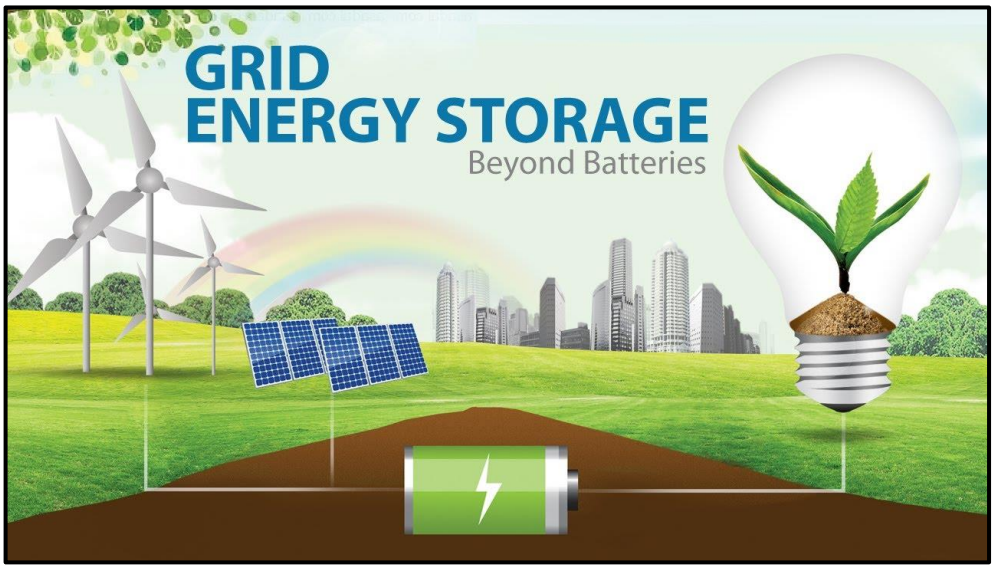


Fig. 2. 6 | Grid energy storage. where batteries play a role in intermittent energy generation.[85]

Military

Military batteries are similar to space exploration batteries, they need to withstand hush weather conditions, have long durability and deliver high-energy densities. Modern war force is depending more and more on batteries, for example, a 72-hour operation needs about seven to eight batteries due to night vision, weapons and communications all need portable battery power. Both primary and secondary batteries are used including Li/MnO_2 and Li/SO_2 as primary batteries and NiMH, NiCd and lead acid as secondary batteries. To date, wearable soldier power is becoming more desirable as the current state of requires soldiers to carry too many batteries that are too large for long missions. The challenge is to develop batteries that are lightweight providing enough power and energy especially for drones operating unmanned.[90]

2.4.2 Battery Performance

Many factors affect a battery's performance, certain electrode materials play a vital role in battery performance especially its activity, however, the rate at which energy is released is connected with the batteries' overall design, type of electrolyte used and other materials incorporated to improve the performance of the cell. Here within we attempt to give s summary about battery performance, terms, theoretical and practical energy and factors that affect battery performance.[90]

Terms and Units

There are many terms used in science and engineering to describe a battery, **table 2.1** summarizes the terms and units

Table 2. 1: Battery Terms, units, and abbreviations

Term	Characteristic Units	Unit Abbreviation
Potential Voltage Electromotive force (emf)	Volt	V
Current	Ampere or amp	A
Resistance	ohm	Ω
Capacity	Ampere-hour or amp-hour coulomb	Ah C
Energy	Watt-hour joule	Wh J
Gravimetric energy density (weight based)	Watt-hours per kilogram	Wh kg^{-1}
Volumetric energy density (volume based)	Watt-hours per cubic decimeter Joules per cubic centimeter	Wh dm^{-3} J cm^{-3}
Power	Watt	W
Gravimetric power density (weight based)	Watts/kilogram	W kg^{-1}
Volumetric power density (volume based)	Watts/cubic decimeter	W dm^{-3}

Potential or Voltage

Potential or voltage (v) is the amount of work or energy (J) that can be done by an electrical charge (C).[90]

Current

Current in ampere or amps (A) is the measure of how fast the electrical charge in coulombs per second (C/s) is delivered. The electrical charge is carried through the external circuit by electrons.[90]

Resistance

In most materials, the current or electrons that flow within are affected by resistance as they travel, so when a potential or voltage produces current it is limited by the resistance in the circuit. In the case of a conducting medium with two points, the potential difference between the points is directly proportional to the current and inversely proportional to the resistance of the conductor; [90]

$$E = iR$$

Where;
E = potential (V)
i = current (A)
R = resistance (ohms)

Capacity

Classified as the amount of electricity transported by a battery and measured in units of ampere-hours (Ah). Capacity is a measure of how long a battery will last in hours at a given discharge current (Ah). The discharge time (h) is multiplied by the discharge current (A) to give capacity in ampere-hours (Ah):

$$\text{Capacity (Ah)} = \text{time (h)} \times \text{current (A)}$$

Take for example a battery that lasted 5 hrs. when discharged at a constant current of 0.15 A can deliver a capacity of 0.75 Ah, alternatively if the capacity of the battery is known and you want to determine how long it will last, the capacity (Ah) divided by the discharge current (A). Most applications do not drain batteries at constant current, however, how a battery is discharged does affect how long it will last and the discharge voltage, for batteries discharged through a power load or resistance may not have a constant current throughout discharge **Fig. 2.7 (a)**, therefore multiplying current by time will yield a wrong answer.[90]

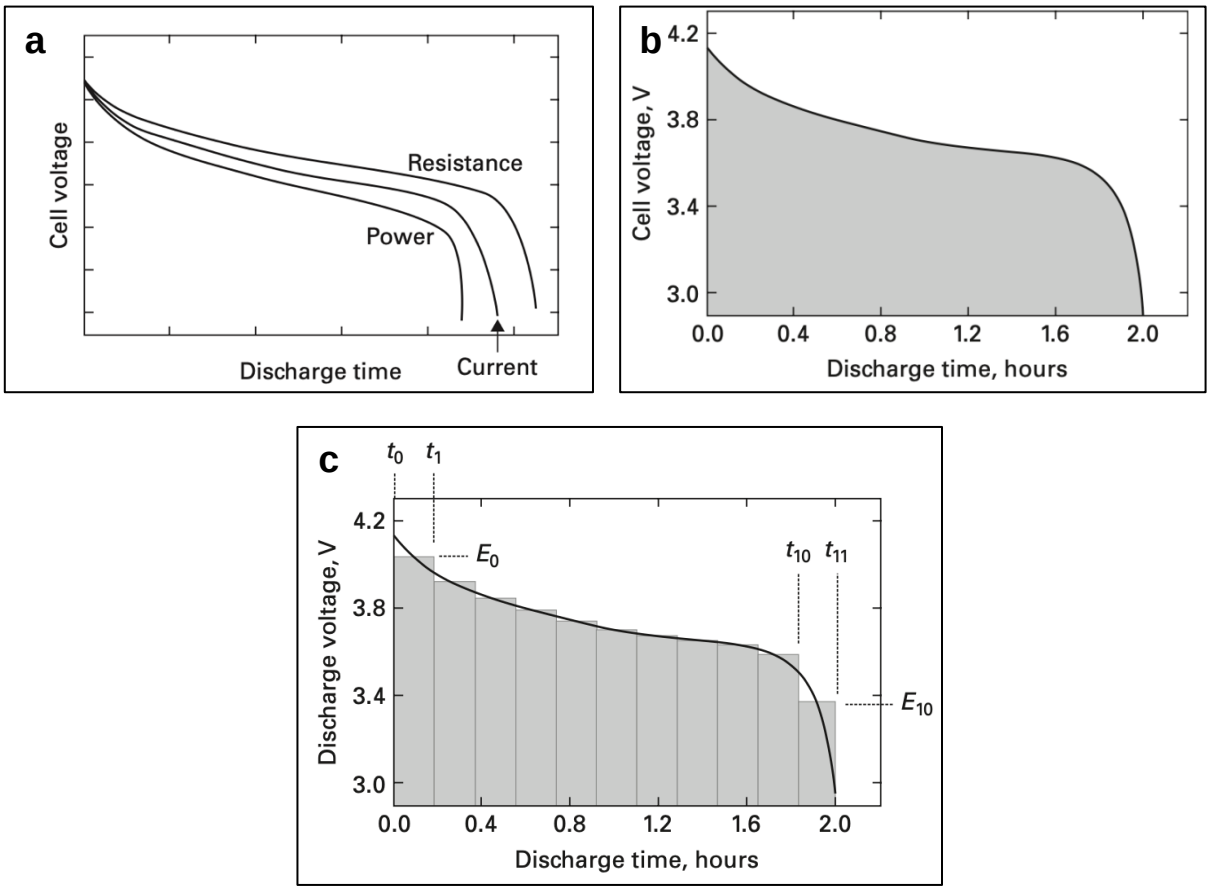


Fig. 2. 7 | Capacity curves. The effect of discharge loads on battery discharge (**a**), The capacity for a battery discharged with a resistor calculated using area under voltage vs time curve (**b**), Using rectangular numerical integration for estimating battery capacity (**c**).[90]

The capacity is thus calculated by integrating the current produced over the discharge time for the battery.

$$\text{capacity (Ah)} = \int_0^t i dt$$

From the Ohm's law $i = E/R$, it can be substituted in the above equation

$$\text{Capacity (Ah)} = \frac{1}{R}\int_0^t i dt$$

With the resistance remaining constant, integration of the battery discharge voltage over time can be taken, as shown by **Fig. 1.11 (b)** the integrated part being the capacity represented by the area under the curve. However, it is not practical to specifically determine the discharge capacity by mean of integration, a mathematical function needs to be established that can exactly reflect how the current changes over time. The next step is by performing an approximation of the integrated portion by estimating the area under the curve using numerical integration. The aim is to section the area under the curve into small rectangles with their midpoints centered on a voltage-time point **Fig. 1.11 (c)**, ensuring the entire beginning and end of discharge is completely accounted for. The area of each rectangle is integrated and a sum of all the rectangles is taken. The more rectangles sectioned improves the accuracy of the approximated discharge capacity.[90]

$$\text{Capacity (Ah)} \approx \frac{1}{R}\sum_{k=0}^{n} E_k \; x \; (t_{k+1} - \; t_i)$$

Where;

i = current (A)

t = time (h)

E = potential or voltage (V)

R = resistance (ohms)

Subscripts *k* rectangular number starting with zero and those with *t* correspond to the time point for each increment starting at t_0

Theoretical Capacity

The theoretical capacity (Q_{th}) is given by the amount of active material in the battery, it is referred to the total quantity of electricity involved in the electrochemical reaction, also defined as coulombs (C) or ampere-hours (Ah), it can be calculated as follows; [90]

$$Q_{th} = \frac{(n) * (F) * (1000)}{(3600) * (Mw)}$$

Where;

n = number of electrons

F = Faradays constant

M_w = molecular weight of the active material

C-rates

C-rate is the charge or discharge current (A) at a rated capacity of the battery, meaning that charge-discharge rates of a battery are controlled by C-rates. The rated base value is usually C or 1C known as 0ne hour discharge is calculated as the current needed to charge or discharge a battery to the rated capacity in one hour meaning that a fully charged battery at 1.5 Ah delivers 1.5 A for one hour:

$$\text{C rate} = \text{rated capacity} / 1 \text{ hour}$$

Where;

C in A and rated capacity in Ah

Table 2.2 shows the different C-rates employed as well as the discharge time used for batteries

Table 2. 2: C-rates and discharge time

C-rate	Discharge Time
6 C	10 min
3 C	20 min
2 C	30 min
1 C	1 hr.
0.5 C or C/2	2 hrs.
0.2 C or C/5	5 hrs.
0.3 C or C/3.33	3 hr. 33
0.1 C or C/10	10 hrs.
0.05 C or C/20	20 hrs.

The battery capacity is measured by a battery analyzer, the analyzer discharges the battery at the specified current while measuring the time it takes to reach the discharge voltage. If a battery at 1.5 Ah provides 1.5 A for one hour, discharged fully for 1 hr. the analyzer will display the results in percentage the as 100 % capacity if it were to discharge fully for 30 min. then the battery will have 50 % capacity. When discharging a battery applying different C-rates to the analyzer, the lower C-rate will display higher capacity and vice versa, **Fig. 2.8** displays the discharge time (h) at various cell potentials (V) expressed in different C-rates. A new battery can sometimes be overrated and can produce over 100% capacity while others can be underrated producing below 100%. Manufactures usually report alkaline and lead-acid batteries at very low C-rates such as 0.05 C or a 2-h. discharge to obtain good capacity readings.[90]

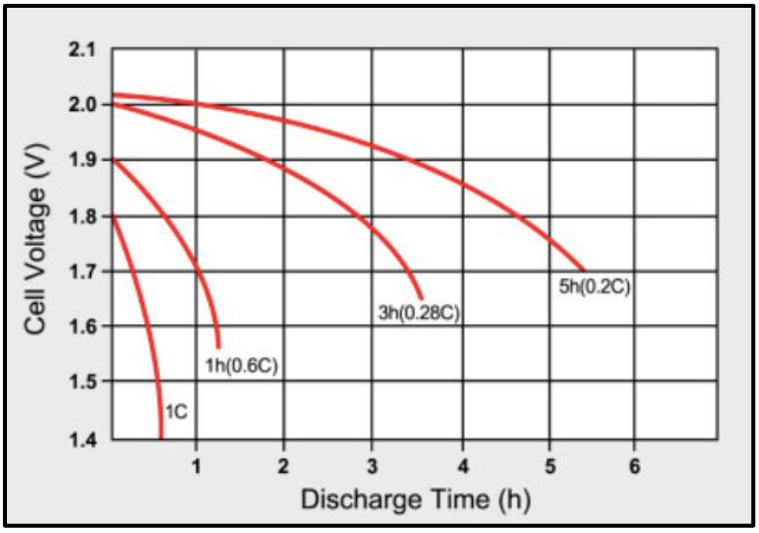


Fig. 2. 8 | C-rate discharge profile. the discharge time (h) at various cell potentials (V) expressed in different C-rates.[90]

Power

To understand power, one has to note that electrical energy is the amount of work done resulting from a flow of charge in coulombs through a potential difference or volts. Thus electrical power is the rate per unit time at which energy is delivered by an electrical circuit. It is calculated by multiplying the potential (E) by the current (i): [90]

$$P\ (W) = iE$$

Energy

The most basic definition of energy is the ability to do work or apply a force to do work. The energy delivered by a battery is measured in watt-hours (Wh), it quantifies how long a battery will last in hours at a given discharge power load in watts. It is easier to measure the energy of a battery when discharged at a constant power load. The power (W) is multiplied with time (h) to give energy (Wh): [90]

$$\text{Energy (Wh)} = \text{power (W)} \times \text{time (h)}$$

If you know the time (h) that a given battery will last and the power load used, then the energy delivered can be calculated. If the power load is not constant throughout discharge, the energy can be determined by using the following equation

$$\text{Energy (Wh)} = \int_0^t Eidt$$

This is like the equation employed to estimate capacity as shown previously, thus if the load is a constant current the discharge voltage time curve is integrated and multiplied by the current. [90]

2.4.3 Battery Engineering and Designs

Although the active material poses the maximum amount of energy that can be delivered which determines the voltage and the amount of active material used determines the ampere-hour capacity, offering a fraction of the theoretical energy in a battery. The main aim is to observe the cell chemistry such as the cathode, anode and electrolyte **Fig. 2.9** that make a battery to work, however, to understand the full nature and performance of a battery, holistically one has to observe its chemical, physical and engineering aspects, thus the battery designs make it more efficient, reliable and safe to use. The aim here is to provide a summary of battery types, shapes, sizes, seals, vents, safety mechanisms, and battery components. [90]

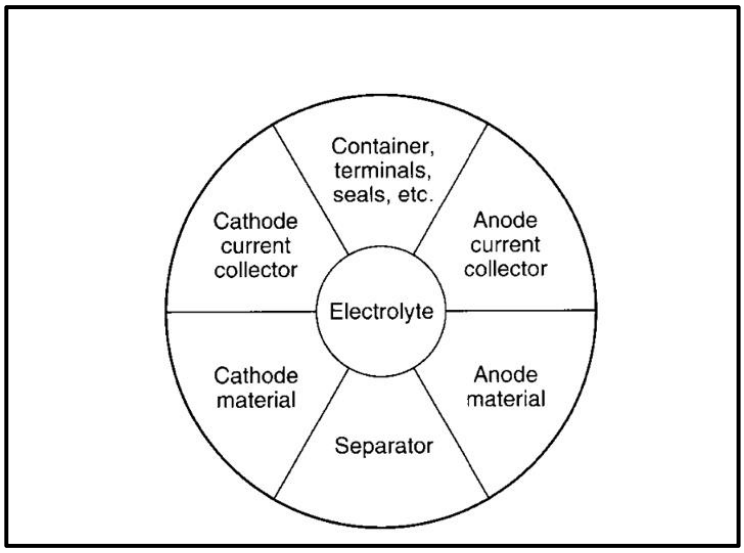


Fig. 2. 9 | Basic components of a battery.[90]

Battery Shapes and Sizes

Batteries have different shapes and sizes designed specifically for a unique application. They are classified as either round or prismatic. Round cells are batteries of everyday use, incorporated in remotes controls, toys, flashlights and watches, they can be differentiated in terms of their aspect ratios in terms of height and diameter. Cylindrical batteries depicted in **Fig. 2.10 (a)** are taller with height to diameter ratios in the range of 0.9 to 8.0. The first cylindrical battery was called a Leclanché dry cell used as an ignition battery for starting gasoline engines produced in a size range of 1.5 inches in diameter by 4 inches in height to $3^{1}/_{3}$ by 8 inches. The most well-known is the no. 6 cells used for clocks and telephones. Button cells as shown in **Fig. 2.10 (b)** are shorter than their diameter, with height to diameter aspect ratios varying between 0.1 to 0.7, even more, the common term is coin cell which ranges between 0.05 to 0.31 in diameter **Fig. 2.10 (c)**. [90]

Prismatic batteries are most commonly used in cellphones, laptops, and cars, the smallest being the solid-state film batteries with sizes of 5 mm long by 5 mm width by 1 mm thickness specifically designed to be mounted in circuit boards, radio frequency identification, wireless sensors, and tags. For commercial applications, many batteries

come in standard sizes with well-specified dimensions having identification codes defined by the ANSI and IEC. [90]

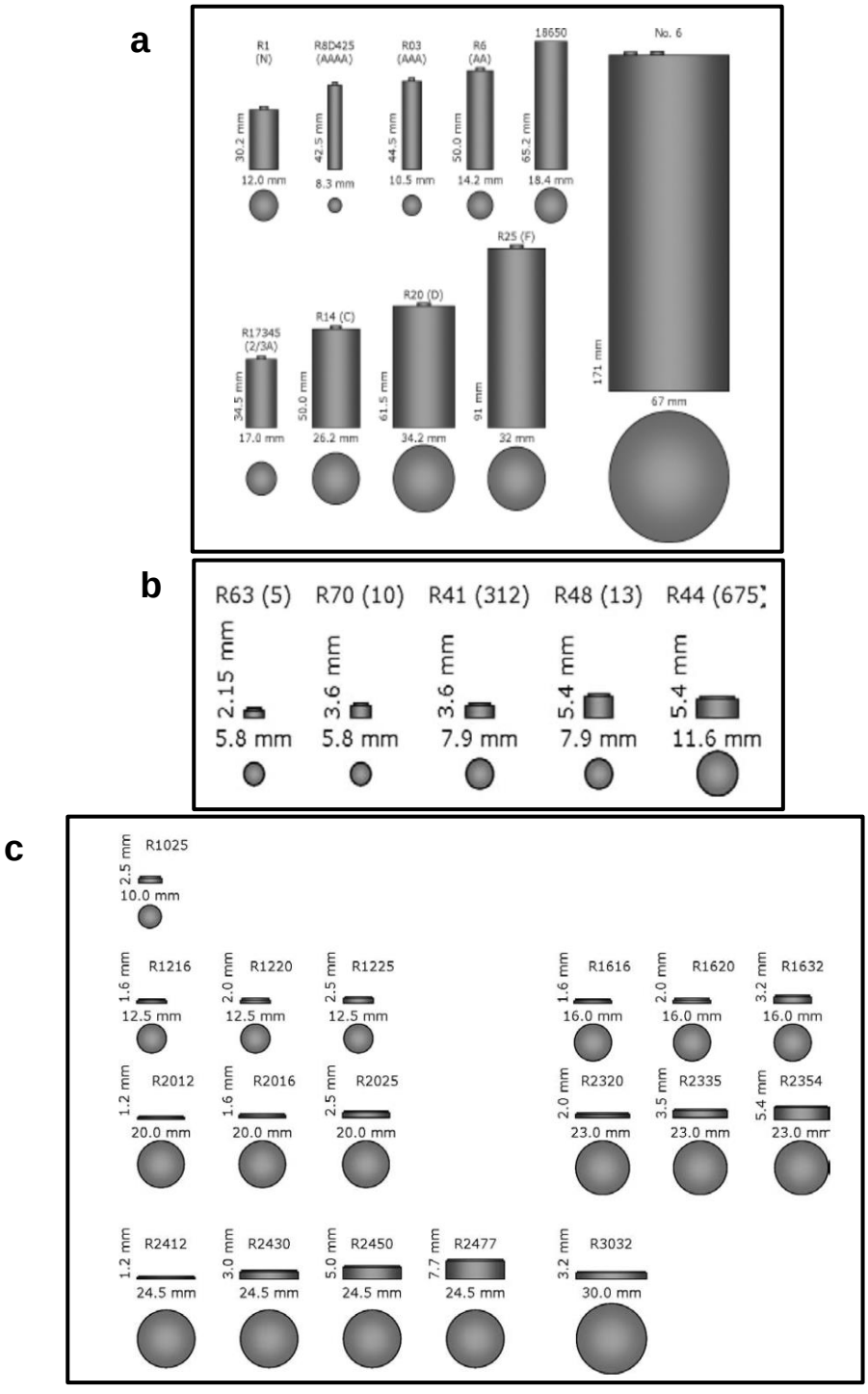


Fig. 2. 10 | Battery shapes and sizes. common cylindrical cells (a), button cells (b), coin cells (c) sizes with the diameter of the cells outlined at the bottom depicted as shaded circles.[90]

Battery Components

The basic components for a battery are comprised of an anode (negative electrode) and the cathode (positive electrode) making up the first component of a battery. Anode materials are usually metals that can be easily oxidized, by giving up their electrons to form ions, these include lithium in lithium-ion batteries (Li-ion), cadmium in nickel-cadmium batteries (NiCd), zinc in zinc-ion batteries and so forth. Other anode materials include carbon used in lithium-ion batteries which readily yields its electrons. Cathodes materials are usually metal oxide powders such as manganese dioxide (MnO_2) and lithium cobalt oxide ($LiCoO_2$). These types of materials are not very electrically conductive (lack current density that allows current to flow), therefore they have to been mixed with an electrically conductive material such as carbon powders, often carbon black or graphite. The second component is a binder that is used to hold the powders together, they consist of polymeric materials (large molecules composed of repeated subunits making up a chain), these often include polyvinylidene fluoride (PVDF) and polytetrafluoroethylene (PTFE). [90]

The third and most crucial component of a battery is the electrolyte, batteries either use an aqueous electrolyte (water-based) or nonaqueous electrolyte (non-water based). Aqueous electrolytes consist of substances that can dissociate into ions like H_2SO_4 in LA batteries, KOH in alkaline cells and $ZnCl_2$ in leclanché zinc-carbon cells. Non-aqueous electrolytes do not use water as a solvent, they typically employ organic liquids, these forms of liquids are vital in lithium-ion batteries because lithium reacts with water causing an explosion. Another form of electrolyte are solid-state electrolyte based on liquid solvents and are able to conduct ions between the cathode and anode material, however since they are solids ions cannot move faster limiting the power output of the battery, thus they are used in low-power applications an example is lithium iodide (LiI). [90]

It is imperative that the electrode a packed close together to maximize energy density, however, the cathode and anode should not touch one another, they will trigger a short circuit which will rapidly discharge the electrode materials without producing useable electrical energy. This leads us to the fourth component of the battery called a

separator which allows the battery designers to efficiently package the electrodes without allowing the electrodes direct contact with one another. The separator must allow ions to pass or flow through it, thus they are made porous allowing a safe channel for ions to soak through. Separators are made up of electrically insulating and ion-permeable materials such as woven and nonwoven fibers, microporous polymer membranes and paper. The last important component are current collectors, these allow for current to flow within a battery from the negative and positive electrode materials to the battery terminals and they consist of metal grids or foils. [90]

Conditions that make up a good electrolyte, anode and cathode material:

Table 2. 3: Conditions that make up a good electrolyte, anode and cathode material

Anode material	Cathode material	electrolyte
• Good conductivity • Stable • Low cost • Good reducing agent • High electrical energy	• Good operating or working voltage • Stable especially when in contact with electrolyte • Good oxidizing agent • Most desirable with light weight offering high voltage and capacity • Low cost	• High ionic conductivity • Non-reactive with electrodes • Low cost • No electric conductivity • Resistance to temperature fluctuations • Safe

2.4.4 Battery Technologies

2.4.4.1 Primary Batteries

Primary batteries only last for one cycle, meaning that they are discharged once and thereafter have to be replaced. These types of batteries are suitable for portable electric and electronic devices, photography equipment, communication equipment, watches, hearing aids, toys, and various other extensive applications. The advantage of using primary batteries are the fact that they are easy to use, simple, convenient require little to no maintenance, have a good shelf life and reasonable cost. Primary batteries have been around for over 100 years. The most notable improvement came right after world war two with new and superior batteries up form 50 $Whkg^{-1}$ to 400 $Whkg^{-1}$. The shelf life before world war two was 1 year at a moderate temperature and modern-day batteries have a shelf life of 2 to 5 years. Recent lithium batteries are capable of 10 years of shelf life and can withstand high temperatures such as 70℃ to as low as -40℃. The increase in higher energy density batteries has evolved in the past decade and has been limited to new and untried materials, the most important developments have been in areas such as shelf life, power density, and safety. The worldwide primary battery market has reached more than $20 billion annually, the popular types being button and cylindrical.[9]

Numerous anode and cathode combinations have been studied to make up a primary battery however only a few have achieved practically. Zinc has been by far the best candidate because of its good electrochemical behavior, good shelf life, abundance in the earth's crust, compatible with aqueous electrolytes and cost-effective. However now there is a high interest in lithium-based primary batteries due to lithium's standard potential of all metals and high gravimetric energy density, henceforth lithium-based anode systems utilizing different cathode materials have the potential to reach even higher energy densities. **Table 2.4** summaries the various systems, characteristics, and applications of primary batteries.[9]

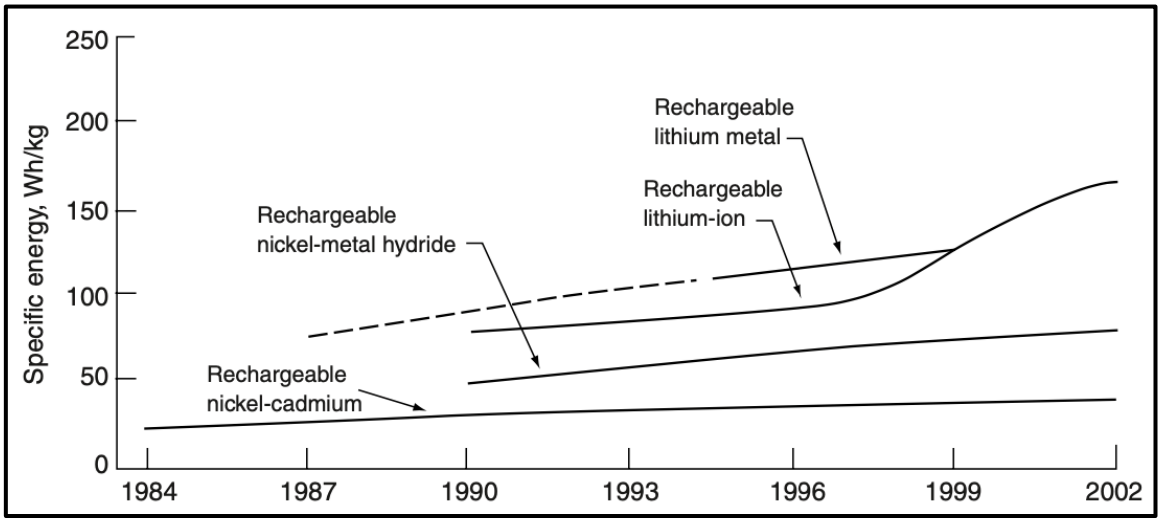
Table 2. 4: Systems, Characteristics and Applications of Primary Batteries

System	Characteristic	Applications
Lithium (solid electrolyte)	Low power battery with extremely long shelf life	Memory circuits and medical electronics
Lithium (solid cathode)	High energy density, long shelf life, low-temperature performance, good rate capability and cost-effective	Cylindrical and button type battery applications
Lithium (soluble cathode)	High energy density, operates in a wide temperature range, long shelf life	Wide range of applications ranging from military power applications to utility meters
leclanché	Most common low-cost battery	Toys, flashlights, portable radios, etc
Zn/Ag_2O	Has the highest gravimetry capacity with good shelf life, however costly	Photography, underwater, hearing aids, electric watches, missiles and space applications
Zinc-air	Highest energy density and low cost	Medical devices, pagers, and portable electronics
Alkaline ($Zn/alkaline/MnO_2$)	Well known general battery, high rate performance, moderate cost, low temperature, and high rate performance	Used in portable battery applications due to its popularity
Mg/MnO_2	High capacity and long shelf life	Aircraft and emergency transmitters
Zn/HgO	Highest volumetric capacity and good shelf life	Medical devices, hearing aids, detectors, military use
Cd/HgO	Long shelf life, low energy density, good and low-temperature performance	Special applications requiring extreme temperature conditions

2.4.4.2 Secondary Batteries

Secondary batteries are also often referred to rechargeable batteries, which have a diverse range of applications with the most common being starting, lighting and ignition (SLI) automotive applications, emergency, toys, lighting, radio, photography and standby power. The most recent use stems from the high interest in electric and hybrid electric vehicles. Major problems have been put in place in developing new systems to meet the requirements of such applications. Conventional aqueous secondary batteries although with the ability to be recharged, with high power density, good low-temperature performance and flat discharge, their energy densities and specific energies are usually low, with poor charge retention than those of primary batteries, this is the main reason why LiBs are more favorable, **Fig. 2.11** (**a, b**) displays the performance of portable rechargeable batteries. Secondary batteries have been around for over 100 years and worldwide the secondary battery is now ~ $20 billion annually, with lithium-ion batteries with a market share of 50% followed by alkaline and lead-acid battery systems at ~25%. **Table 2.5** summaries the various systems, characteristics, and applications of secondary batteries.[9]

a



b

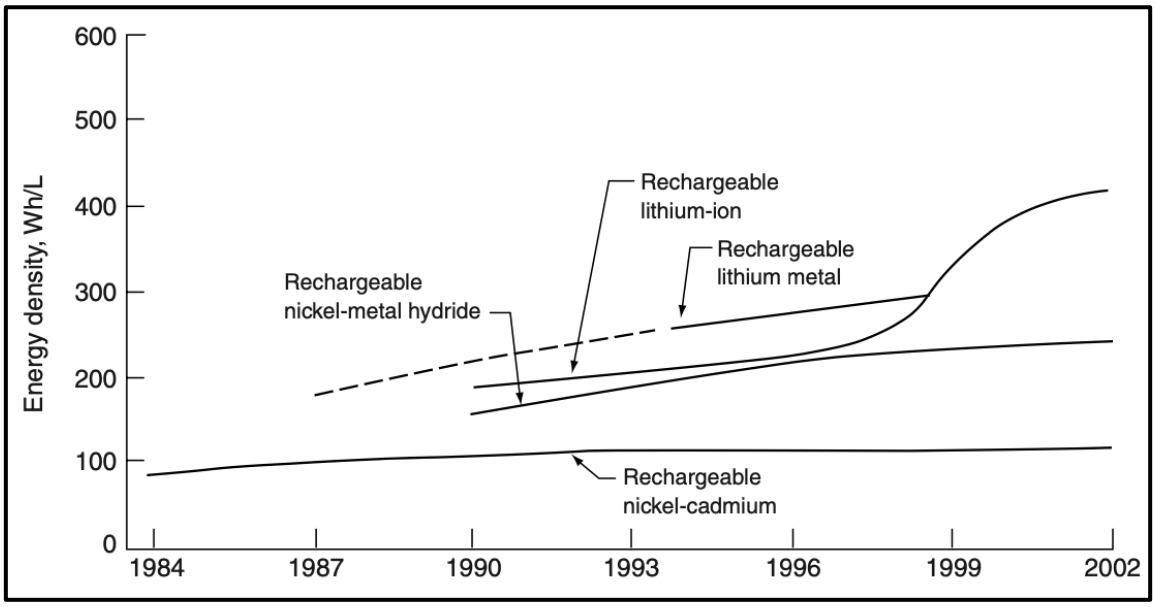


Fig. 2. 11 | Recent advances in the performance of secondary batteries. Specific energy ($Whkg^{-1}$) (**a**), Energy density (WhL^{-1}) (**b**).[90]

Table 2. 5: Systems, Characteristics and Applications of Secondary Batteries

System	Characteristics	Applications
Lithium-ion	High energy density and long cycling life	Consumer electronics, space application and electric vehicles
Ambient temperature (Zn/MnO_2)	No maintenance, good rate capability, cost effective, good capacity retention and limited cycle life	Consumer electronics and cylindrical cell applications, replacement for alkaline and zinc-carbon
Nickel-hydrogen	Long cycle life	Aerospace applications such as LowEarthOrbit and GEOstationary satellites
Silver cadmium	High specific energy, moderate cycle life, good charge retention and high cost	Portable lightweight equipment and space satellites
Ag/Zn	Highest specific energy, low cycle life, high rate capability and high cost	Drones, space probes, Portable lightweight equipment, military equipment and launch vehicles
Nickel-zinc	High specific energy, good rate capability and long cycle life	Scooters, bicycles and trolling motors
Nickel-iron	Low specific energy, long cycle life	Stationary applications
Nickel-metal hydride	Has higher capacity than NiCd batteries and maintenance-free	Electric and hybrid vehicles and portable devices
Nickel-cadmium: Portable Industrial	Maintenance-free, superb cycle life, high-rate low-temperature performance	Portable tools, appliances, standby power, consumer electronics and memory backup Industrial, communication

	High rate, superb cycle life, low-temperature capability, and flat voltage	equipment, emergency power applications, and aircraft batteries
Lead-acid Portable	Maintenance-free, moderate cycle life, low cost	TV, portable tools and electronic equipment, small appliances
Motive power	For deep 6 to 9 hr., discharge cycling	Electric and hybrid electric vehicles, industrial trucks
Stationary	Suitable for standby float services with long cycle life	Utilities, load leveling, emergency power, energy storage
Automotive	Most common, cost effective battery with moderate specific energy, maintenance-free and low-temperature performance	Aircraft, lawnmowers, golf carts tractors, and marine

2.5 Sodium-ion Batteries

Energy supply is an essential part to human life. To effectively utilize green power supply, advanced energy storage technologies should be considered. In the past, various types of devices for storage have been considered, such as fuel cells, supercapacitors, batteries and so on. Amongst these, batteries are the most viable due to their high volumetric energy densities and can be easily integrated into off grid energy systems.[11] LiBs have become the common power source supplier for electronic devices, since their introduction by Sony in the early 1990s. Introduction of lithium-ion batteries onto the automotive market such as a battery of choice for powering HEVs, PHEVs and EVs can reduce the dependence on fossil fuels.[12,13] However, applications for LSE devices, such as EVs and grid, limit the use of lithium due to its low natural abundance, which will lead to elevated costs.[11]

The problem with the power grid is that it relies on the stable and continuous generation of electricity, but solar and wind energy are intermittent and depend on environmental factors and therefore, considered not unsuitable for power grids. To overcome this problem large scale electrochemical energy storage technologies based on batteries have been of great interest, mainly for their flexible power, high round trip characteristics that meet different grid functions, long cycle life and low maintenance.[12]

In 2014, the US government conducted a survey on the global reserves for lithium, according to their analysis, the reserves where 13 million tons with a demand of Li_2CO_3 to grow by 16.76 % within the next six years, therefore meaning that the global lithium reserves without recycling can last for 28 years.[12,14] The demand is approximated to grow astronomically by the introduction of electric vehicles which generally use 60 kWh lithium-ion battery pack. Due to the resource depletion, we expect an exponential increase in the price of lithium, thus it cannot meet the requirements of increased industrial production.[12] With the potential of running out of lithium deposits some determined attempts began to revisit SiB technology and its key materials, after the year 2010. Up until now, numerous sodium based compounds have been extensively investigated and some of them being capable of delivering reversible capacities close to their theoretical values.[13]

Room temperature SiBs have been viewed as the most suitable electrode materials, due to their cost-effectiveness and resource supply, thanks to the unlimited supply of seawater. Sodium is the fourth most abundant element on the earth's crust (2.74%). The cost of sodium carbonate roughly ($135-$165 per ton) compared to lithium carbonate ($5000 per ton in 2010).[8] The best part about sodium is that it is an alkaline metal and lies in the same group as Li and thus has similar chemical performance, allowing as much work carried out for lithium-ion to be conducted on sodium-ion batteries.[12,15] The main aim is to boost the energy density of sodium-based materials, so that it may be comparable to commercial LiBs materials. An effective approach is to increase the operating potential of the battery, by using electrochemically stable cathode materials with high voltage vs Na^+/Na.[14]

Not only do sodium-ion batteries offer price-reduction, SiBs can obtain faster kinetics with the electrochemical reactions, by enabling a high Na^+ ion conductivity in bulk solid within a wide temperature range and ease of charge transfer, with the benefits of less pronounced solvation.[13,14] The battery components and electrical storage for both LiB and SiB are similar, except for their ion carriers. The Problem with Na^+ ions is the larger cation radius and the heavier atomic weight (1.02 Å) than those of Li^+ ions (0.76 Å)[16], which affects transport properties, phase stability and interphase formation. Also, Sodium has a heavier atomic weight (23 $gmol^{-1}$) than lithium (7 $gmol^{-1}$)[17]; which results in an inferior reversible capacity and lower volumetric energy densities.[8]

With such alluring attributes, SiBs endures a lower energy density than LiBs, but can be short-lived, by increasing the output voltage or capacity. The positive electrode is considered the main target for boosting the energy output of SiBs and many attempts have been made to develop cathode materials for SiBs which include, transition metal sulphides and, sulfides, layer and tunnel type transition metal oxides, and metal fluorides, prussian blue analogues and oxyanionic compounds thus there is a major search for sodium-ion based cathode materials with high operating voltages, high structural stability and a large reversible capacity remains an obstacle for future development.[14] Another major obstacle is the development of an anode with desirable Na voltage storage, high structural stability, and large reversible capacity. It has been demonstrated that graphite anode materials used for lithium storage do not intercalate properly with sodium ions, thus non-graphitic anodes which consist of carbonaceous

materials such as pitch-based carbon-fibres and activated carbons allow better insertion of sodium ions, amongst these, hard carbons are considered to be the first-generation anodes of choice for SiBs. It must be noted that SiBs are not fabricated using sodium metal due to dendrite formation, unstable passivation layer occurring in most organic electrolytes and high reactivity which are very problematic than those occurring in LiBs (lithium metal anodes). Another safety hazard is the low melting point of sodium at ~97.7 ℃ especially for devices that utilize Na metal electrodes at ambient temperature, therefore a proper Na-ion exchange system between the cathode and anode is needed that has a rocking-chair format.[8]

From the previously stated problems to add on, new forms of electrolytes have to be developed to ensure adequate use of SiBs since the use of organic liquid electrolytes raises safety issues and practicality. The most common electrolytes used are $NaClO_4$ and $NaPF_6$ salts in carbonate ester solvents. The use of such electrolytes cause the Na metal to degrade and corrode instead of forming a strong SEI (solid electrolyte interface) which is a layer that is formed during the first cycle during *sodiation℃* or intercalation, allowing ions to flow freely and isolates electron flow and is made up of the decomposed products of the electrolyte components).[18] Researchers propose that developing aqueous electrolytes instead of organic electrolytes and finding the best anode suitable for such applications is of pivotal importance to achieve the success of SiBs. **Figure 2.12** below depicts various cathode, anode, and electrolytes utilized in SiBs.[17]

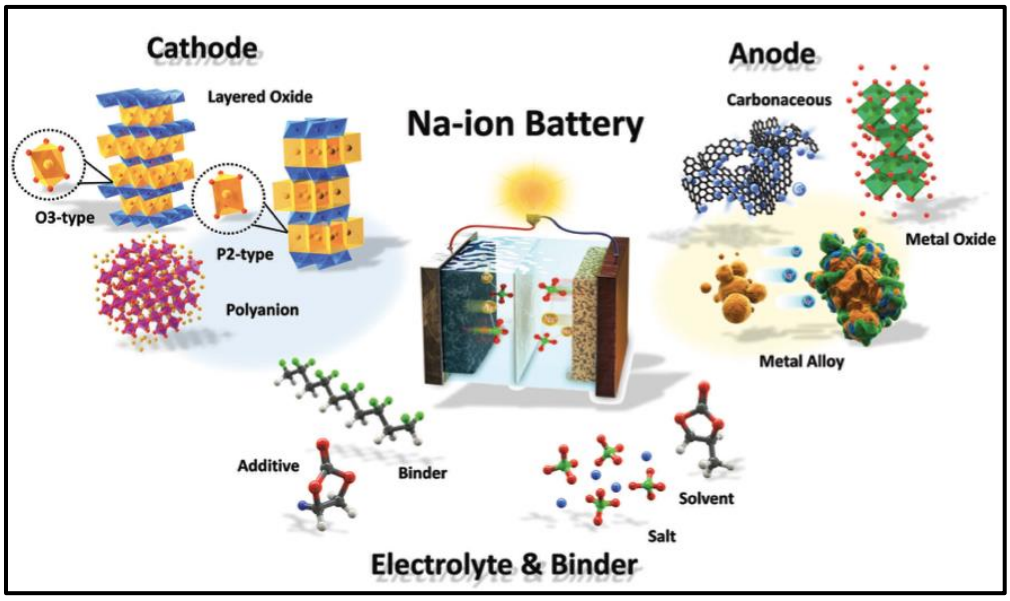


Fig. 2. 12 | Sodium-ion battery showing cathode, anode and electrolyte materials.[17]

2.5.1 Sodium-Ion Anode Materials

To qualify as a sodium-ion anode material, it must meet the requirements of low voltage vs Na^+/Na couple, also not be so like impede dendrite formation. Over the past 50 years, unlike lithium-based batteries that utilize graphite as their anode material, sodium cannot be intercalated into it due to its large size, with that, hard carbon has been the most conventionally used material which gives good reversibility and capacities. Another is titanium oxides which are known for their alkali metal intercalation at low voltage due to the reduction potential of Ti^{3+}, but do not compete at the level of hard carbons. Alloys have been considered since they have interesting electrochemical properties, however, they suffer from volume change upon sodium intercalation causing capacity fading. Phosphorous based Na_3P has also been considered, however it reacts vigorously with water to form phosphine which is toxic and burns spontaneously in the presence of oxygen. Also, organic materials have been considered, but most of them have large irreversible capacity and require very high voltages for desodiation which is not practical for sodium-ion batteries. Like the electrolytes briefly explained above, further research for the best anode candidate is still ongoing. One of the purposes of dissertation is to employ zinc as a possible anode material for aqueous sodium-ion batteries which will be introduced next.[19,20,21]

2.5.2 Zinc Metal Anodes for SiBs

Check the recent discussion above on developing aqueous SiBs, herewith in I will be discussing the best anode thus far utilized for aqueous batteries. Ever since the discovery of the first battery by Volta, metallic zinc has been regarded as the most ideal anode material for aqueous batteries amongst other multivalent anodes such as aluminum, manganese, and iron because of its low electrochemical potential (-0.762 V vs the standard hydrogen electrode (SHE)), high theoretical capacity (820 $mAhg^{-1}$), low toxicity, high abundance, environmental friendliness, stability in water, low flammability, high compatibility and inexpensive.[22,23,24] Overtime the attempt to develop zinc rechargeable alkaline batteries were done and Zn-MnO_2 was discovered, but unfortunately, it was hampered by poor cycling performance due to the formation of zinc dendrites and irreversible discharge species. Recently research on zinc-metal anode batteries has gained popularity with the number of publications excepted raising to nearly 40 to 50% percent each year especially from 2014 to 2018 as shown in **Fig. 2.13 (a).** Zinc metal-anode based batteries have a similar set up as previously stated SiBs in **Fig. 2.12**. they may utilize various materials which include and not limited to prussian blue, vanadium-based and manganese-based cathodes offering a narrow electrochemical stability window (2–2.5 V) as shown in **Fig. 2.13 (b)**, than their organic counterparts (3-5 V)[25], a mild aqueous electrolyte and a zinc metal as anode, **Fig. 2.13 (c)**.[26]

The commercialization of secondary based using zinc metal batteries have been hampered by several limitations. The major problems are due to its being dendrite formation, metal corrosion, and hydrogen evolution. This leads us to the determination of the right electrolytes to use in such applications as they are as important as determining the right cathode material and plays a major role by forming protective layers at both the cathode and anode. The next part **2.1.2** will discuss and elaborate on both these forms of electrolytes used in zinc-metal anode-based batteries in detail.

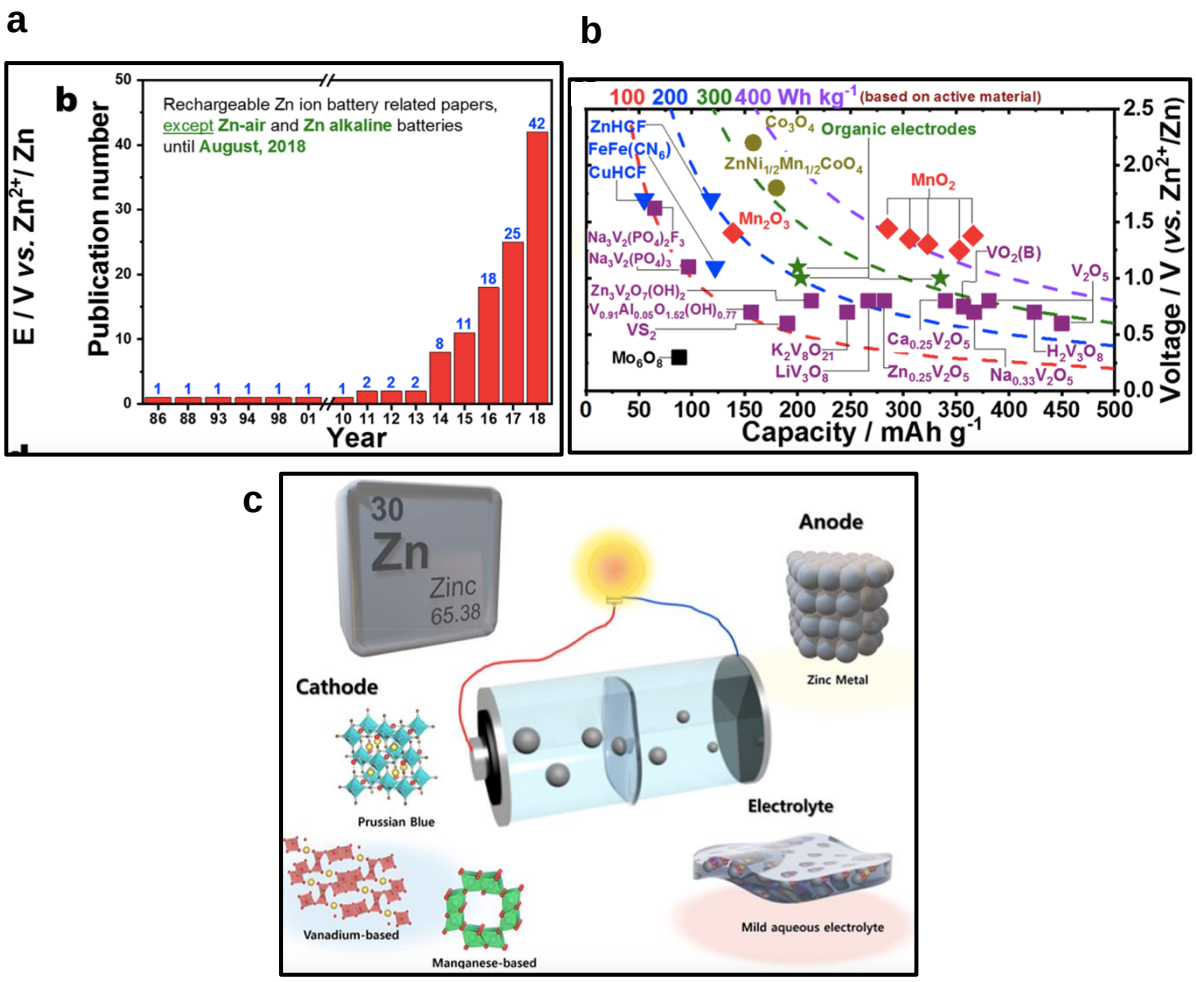


Fig. 2. 13 | Zinc metal-anode batteries. Number of publications (a), Ragone plot of active materials used in Zinc-metal-anode based batteries (b), Schematic of a Zinc-metal-anode used in batteries (c). ref [26]

2.5.3 Sodium-Ion Battery (SiB) Electrolyte

Electrolytes play an important role in battery chemistry as its main function is to transport ions and make a connection between cathode and anode, they also provide a protective layer at the electrodes, surface layer and SEI. Therefore, electrolytes must contain the following properties:

1. Chemical stability
2. Chemical stability at low and high voltages
3. Thermally stable
4. Good ionic conductivity
5. Safety
6. Low cost

To be able to achieve these characteristics, researchers are working on interrogating the characteristics of the salts and solvents which usually affect the cell performances.[8,26,27] The salt should have stability with the cell component, solubility in the solvent and stability vs. reduction/oxidation, the solvent must be polar with good dielectric constant, with low viscosity to enhance ionic mobility, remain inert during charging and high melting and boiling point. Over the past decade, researchers have been working on finding the best combination of electrolytes, however, none has been developed for practical use of SiBs, however, the best electrolyte to date is the carbonate ester-based electrolyte solution which incorporates sodium salt this electrolyte is for non-aqueous sodium-ion batteries. From as early as 1980, $NaPF_6$, NaI and $NaClO_4$ have been considered for development as electrolytes however sodium perchlorate ($NaClO_4$) has been the most commonly used due to electrochemical reasons and low costs, although concerns of safety and issues about the difficulty to dry have been highlighted, it still strives as the best candidate.[8,26,27] Not only does $NaClO_4$ work for non-aqueous applications, it can also be deployed in aqueous sodium-ion batteries known as water-in-salt batteries which are environmentally friendly and low cost, H. Zhang et al. investigated by varying the concentrations of $NaClO_4$ from 1, 4 and 8 M and studied the impact of the electrolyte on the performance of the electrode materials, they discovered that at high

concentrations the electrode material had stable cycling performance and good rate capability, however with very high resistance after 50 cycles. With this information in our research, we chose to use the 4 M $NaClO_4$ water-in-salt concentration since it had a greater ionic conductivity of 170 $mScm^{-1}$ than 8M $NaClO_4$ (100 $mScm^{-1}$), with moderate stability and rate capability, displaying low resistance after 50 cycles.[28]

2.6 Triplite (Mn_2PO_4F) As Energy Storage Material for SiBs

- The first work to be done on Triplite by Hurlbut in 1936 suggested that triplite consisted of an isomorphous series of two elements of forming a divariant series of metals Fe^{2+} and Mn^{2+} containing large amounts of Mg and a less amount of Ca, the variation in Fe and Mg influence the optical properties with Mn variation offering little effect.[29]

- In 1940 the journal of The American Mineralogist categorized triplite to fall under the Sarkinite Group which consist of triplite, Wagnerite, sarkinite and triploidite, characterized by similar cell edge lengths, however during this period the morphology of triplite mineral was unknown since there was no measurable crystals but it was given a space group of $C_{2h}^5P2_1/a$ from the following refection's; (hkl) with all present, (h0l) with h even and (0k0) with k even, the unit cell content was $16[(Mn,Fe)_2PO_4(OH)]$.[30]

- The first-ever measurable triple crystals to be recorded were found in 1947 at the Mica Lode pegmatite, Eight Mile Par, Fermont Country of Colorado state reported by C. W. Wolfe and F. WM. Heinrich[31] were they examined four crystals on the basis of crystallographic measurements and x-ray examination, they found the Triplite to be monoclinic of space group *I* 2/m, with lattice parameters a_0 = 11.90, b_0 = 6.48, c_0 = 9.92, β = 105°53. The reported colour of triplite mineral is brown with a greasy luster [32].

- In 1969 L. Waldrop went further on to investigate the crystal structure of triplite $(Mn,Fe)_2FPO_4$, he proved that Mn is bonded to half-filled sites F(1) and F(2), P was surrounded by four O atoms forming a tetrahedron and Mn(1) and Mn(2) described as a distorted octahedron with four O and two mutually exclusive F sites with partial site occupancies located ~0.62 Å apart.[33]

- Finally, we reach the $Mn_2(PO_4)F$ by J.R. Rea and E. Kostiner in which they grew a single crystal of $Mn_2(PO_4)F$ by standard reflux melt techniques using excess MnF as reflux. This form of triplite is a pure member of the triplite determined by L. Waldrop in 1969. Their analysis reveals that the $Mn_2(PO_4)F$ crystallizes in the monoclinic space group *C2/c* (**Fig. 2.1.3** (**a**)) with unit cell dimensions *a* = 13.410 (4), *b* = 6.5096 (5), *c* = 10.094 (2) Å and β = 119.99 (1)° (Z=8) Mn atoms lie at the centers of the highly distorted octahedra, both the Mn(i) and Mn(2) atoms are coordinated by four O atoms, two F atoms each were the fluorine atoms are cis in both cases and the phosphate tetrahedra was discovered to be regular sharing only comers with the polyhedra. They further went on to say that their $Mn_2(PO_4)F$ is isostructural with the mineral triplite with the expectation that there is no disorder in the fluorine site in the triplite and occupies only one position in the structure when compared to the triplite, the fluorine in $Mn_2(PO_4)F$ occupies a position between the half occupied fluorine sites in triplite.[34]

- P. Vignola et. al. also did a structure analysis on the triplite $Mn_2(PO_4)F$ from the Codera valley in Italy, the data led to one F site similar to what J.R. Rea and E. Kostiner reported, **Fig. 2.1.3** (**b**) depicts the crystal structure of triplite $Mn_2(PO_4)F$ obtained by P. Vignola et. al..[35]

The purpose of this MSc degree research is to explore the electrochemical behaviour and performance of the triplite $Mn_2(PO_4)F$ structure as a cathode material for energy storage, specifically, rechargeable aqueous SiBs, since there is no reported data on $Mn_2(PO_4)F$ as an energy storage material.

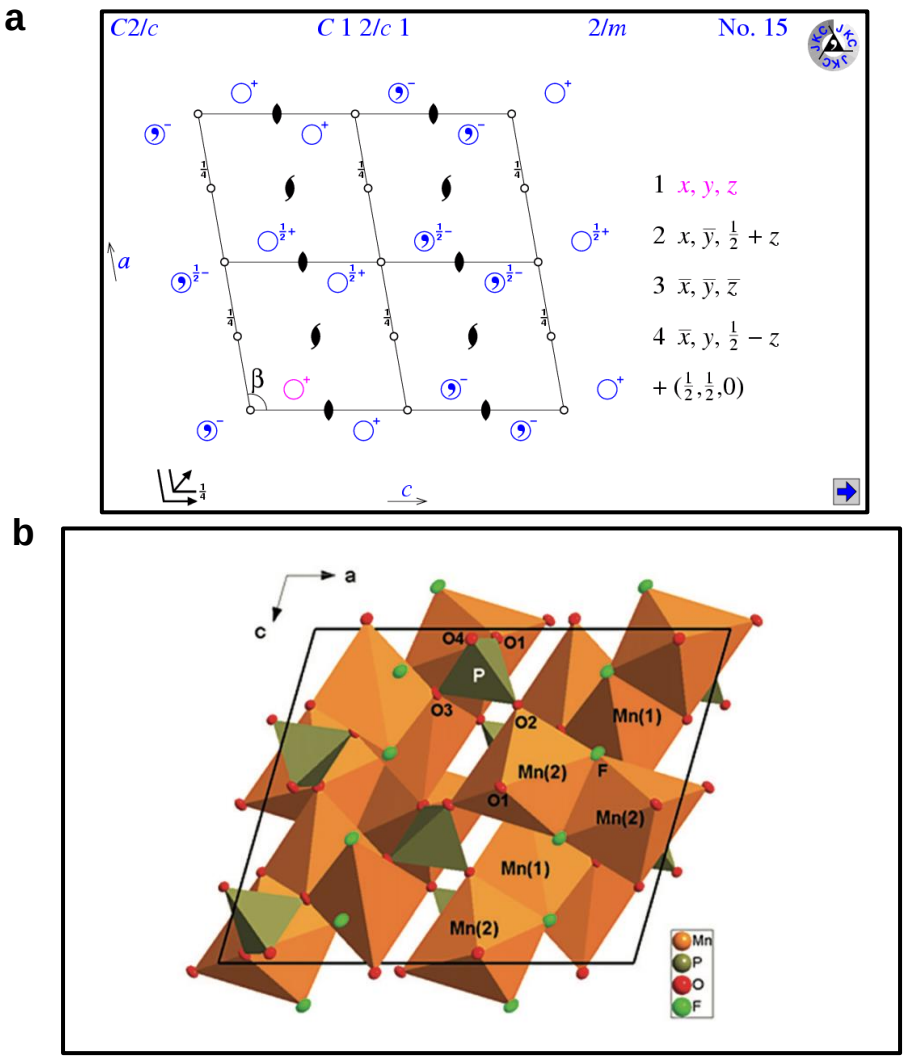


Fig. 2. 14 | Monoclinic space group C2/c of $Mn_2(PO_4)F$ (**a**), crystal structure of $Mn_2(PO_4)F$ (**b**).[35]

2.7 Strategies for Improving Electrochemical Performance And Cyclability

Since we have had an introduction and insight of Triplite (Mn_2PO_4F), it must be stated that the electrochemical properties and performance of this material as a possible energy storage system have not yet been determined. The purpose of this research is to interrogate these physical-chemistries and provide new information about this material as a battery cathode material. It is safe to say that since the Triplite (Mn_2PO_4F) includes Mn^{2+} as its main element as host stru3cture, it will undergo redox reactions upon charging and discharging. It is known from MnO_2 that Mn^{2+} containing materials suffer from Manganese dissolution, dissolution is the loss of Mn^{2+} soluble ions which occurs at the interface of the cathode and electrolyte, therefore stabilizing the cathode from the attack of the acid electrolyte is essential to prevent dissolution and Jahn-Teller distortions, these occur in the d5 low spin octahedra Mn^{2+} complexes.[56,57,58,59] the main purpose is to propose strategies used to counter these effects and elaborate on possible methods to solve them.

Cathode Dissolution

Firstly we will interrogate manganese dissolution, this is usually caused by disproportionation reactions during cycling and structural transformation leading to degradation of the active material, thus causing Mn^{2+} dissolution, in the case of our triplite material the manganese dissolution occurs via the following reaction displayed below.[36,37,38]

$$2Mn^{3+} \rightarrow Mn^{2+} + Mn^{4+}$$

Proposed strategies developed to mitigate this issue:

1. **Surface coating**: Not only can it improve conductivity, the electrode coating stabilizes the structure by forming a surface protective layer on the active material, carbon and graphene enclosed shell wrapping structure is thought to be beneficial to inhibit Mn dissolution.[36]

2. **Addition of Mn salt in the electrolyte**: Mn^{2+} ions addition into the electrolyte will tend to stabilize the materials internal structure and integrity by restricting Mn ion insertion by blocking the vacancies, which is essential to lowering the amount of ions de-intercalating and intercalating into the internal structure which affects the materials capacity retention and causing instability in the crystal structure.[36]

3. **Incorporating closely-bonded ions:** A study revealed that by incorporating k^{+}-ions in-between the MnO_2 (polyhedron) channels will provide a conductive protecting effect onto the host structure ceasing dissolution.[36]

Our Proposed Methods

2.7.1 CeO_2 Coating

CeO_2 coating is said to improve the cathode materials activity and kinetic process, Yao J *et al*. reported a study on the effect of CeO_2 on $LiFePO_4$ and found this to be true. [44] H. Wook Ha *et al*. explored the effect of percentage coating of CeO_2 in the range of 2-5% on $LiMn_2O_4$ and discovered that 2wt%-CeO_2 coating suppresses the Mn^{2+}-ion dissolution (low amounts of dissolved Mn-ions were detected in the electrolyte) whilst maintaining high capacities with more than 82% capacity retention over 150 cycles and at higher percentage coating the capacity decreases, hence a lower coating percentage is more desirable for manganese-based batteries to keep its integrity.[45]

An even interesting observation was made by M Minakshi *et al*,[46] they investigated the effect of CeO_2 addition onto MnO_2 as an aqueous lithium battery in the attempts to understand the electrochemical behavior and mechanism of in which CeO_2 impact on

cycling behavior. They investigated a wide range of percentage loadings from 0.2 to 5wt% to identify the optimal loading, their results revealed that CeO_2 enhances the performance of cycling and maintains capacity upon cycling. After the first cycle the capacity increased to about 25% of the initial cycle, which is believed to be due to the suppression of undesirable oxygen evolution (UOE). To understand this correctly, one needs to know that in an aqueous systems the charging efficiency and its operation is affected by oxygen evolution described by the following reaction:

$$2OH^- \rightarrow H_2O + ½\ O_2 + 2e^- \quad (1)$$

During charging some of the charge current is consumed by UOE reaction (1) and is known to increase with increased charging voltage, they discovered that during charging of the pristine-MnO_2, part of the charging current may be used up by the UOE reaction, hindering the process of reverting back to active material MnO_2 leading to capacity fade. The presence of CeO_2 can subdue the UOE reaction; by increasing the overpotential for oxygen evolution as such would lead to an improvement in coulombic efficiency and could allow the discharged MnO_2 back into its active form. Lastly, they also discovered that 2wt% CeO_2 addition is the most effective and optimum to obtaining high capacities and good stability. Upon an increase to 5wt% CeO_2 addition the capacity decreases, it was suggested that the 2wt% addition has a synchronizing effect with the active material.

2.7.1 Carbon Coating

Carbon is one of the most abundant elements on the planet, it is low cost and can be extracted from various sources such as hydrocarbons, resin, and polymers etc. Carbon has many physical properties such as structural flexibility, low density, good mechanical strength when applied as a coating it forms a thin film layer on the surface of the active material and is usually synthesized by chemical vapor disposition (CVD). Carbon coating is of significant importance, its most valuable property is having good electronic conductive since most electrode active materials are semiconductors and insulators which are synthesized as powders, need a conductive additive to increase electrical conductivity along with a polymer binder to hold the mix together. Research reveals that with LiBs mostly with Mn as host structure, the nanosized particles are prone to form agglomerated particles due to high surface energy arising from the high surface area making them difficult to disperse and mix with the conductive additive depicted in Fig. 2.1.4 (a), the electronic path length (L_e) is greater than the particle size (r) because only a few nanoparticles in the agglomerates are in direct contact with the carbon additive and acquire electrons, thus leading to an increase in the interfacial resistance. To circumvent this problem, each nanoparticle is fully coated with an electronic conductive layer, thus shortening the electronic path length (L_e) to a level which is comparable to the particle size (r) of the nanomaterial; the electron can pass through with ease along the outer surface of each nanoparticle devising a continuous flow of electrons, leading to a reduction in the interfacial resistance as depicted in Fig2.1.4 (b). [47]

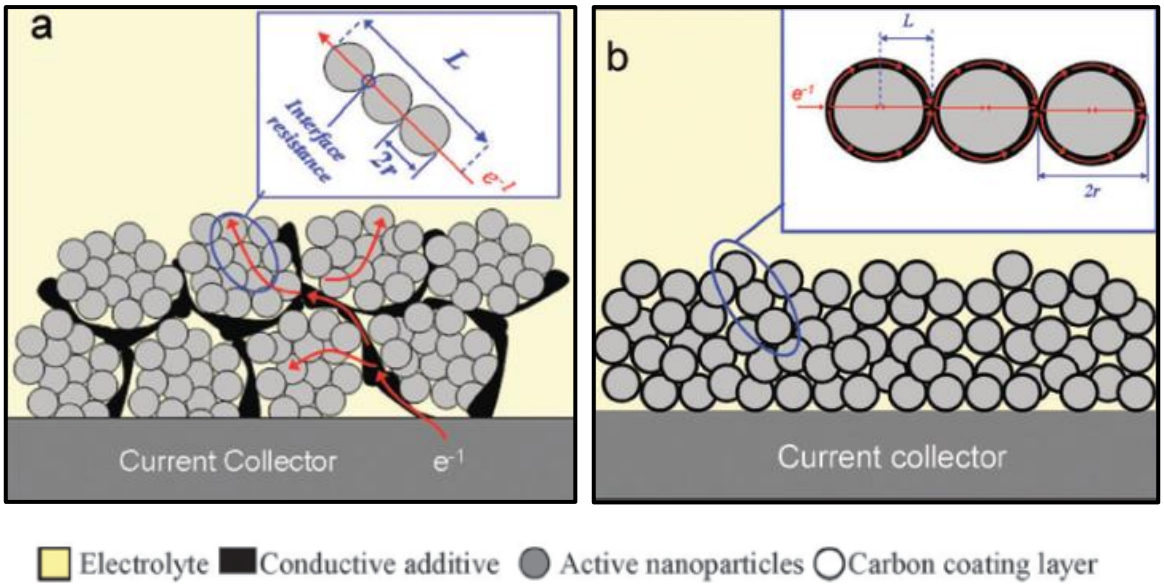


Fig. 2. 15 | Schematic of the electronic path length (L_e). Nanoparticles without coating (**a**), nanoparticles with carbon coating (**b**). ref.[37]

CHAPTER THREE

Characterization and Techniques

Importance of Surface Techniques

Materials are known to interact with their surrounding mainly through their surfaces, the physical and chemical properties of these surfaces determine the nature of the interactions. Their surface chemistries will influence interactions such as catalytic activity, contact potential, adhesive properties, wettability and many more. As such, surfaces influence many important properties on any material. Another important fact is that only a small portion of atoms are in many materials are found on the surfaces which the exact proportion depends on the surface roughness, shape, and composition, therefore any surface technique to be employed must have these two characteristics, (i) must be extremely sensitive, (ii) must be efficient in filtering majority of the signal from atoms present on the sample.[73]

3.1 Physical Characterization

3.1.1 Powder X-Ray-Diffraction

Powder X-rays are electromagnetic waves with wavelengths that are shorter than visible light, they are based on wave interferences. Two electromagnetic waves of the same wavelength traveling in the same direction depending of their phase will either coincide constructively ($n\lambda$) or destructively ($n\lambda/2$). The X-ray beams incident from a crystalline solid is diffracted by the crystallographic plane, as illustrated in **Fig. 3.1** two incident beams will be deflected by a crystal plane (blue dots), if they are in phase the Bragg's law will apply, which is calculated by the path difference between the two beams that depends on the incident angle (θ) and the spacing between the parallel planes (d). When constructive interference is detected, information such as spacing between atomic planes of a crystal at a given wavelength of the incident beam and angle. From this equation information on the spacing between the atomic planes of a crystal, the crystal structure can be determined, together with the lattice parameters.

$$n\lambda = 2d\ sin\theta$$

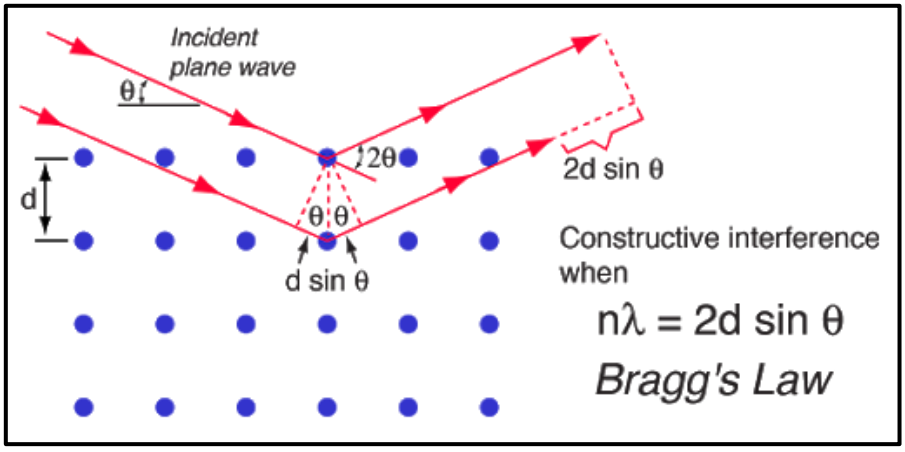


Fig. 3. 1 | X-Ray diffraction diagram. Bragg diffraction.[86]

3.1.2 Raman Spectroscopy

It was in the early 19th century was the Indian scientist Chandrashekhara Venkata Raman discovered the phenomena of the inelastic scattering of light which is now commonly known as the Raman effect. This effect describes the wavelength obtained from a scattering of a small area with a difference in frequency from that of the incident beam and the scattered wavelength depends on the chemical structure of the molecules responsible for scattering. Raman spectrum uses the scattered light to obtain data about molecular vibrations which can provide information about the structure, electronic environment, symmetry and bonding.[48,49]

Mechanism and Instrumentation

When a molecule is irradiated with monochromatic light results with elastic and inelastic scattering. In elastic scattering no change in wavelength and energy as well as photon frequency while inelastic scattering which has a change in photon frequency due to deactivation or excitation of molecular vibrations in which the photon may lose or gain energy.[48,49] **Fig. 3.2** (**a**) displays a schematic of the Raman instrument. Three types of scattering can occur displayed in **Fig. 3.2** (**b**);

1. **Stokes Raman scattering** involves transitions from lower to higher energy vibration levels obtaining intense bands
2. **Rayleigh scattering**: Light incident on the molecule interaction has a net-zero exchange in energy, the frequency of the scattered light is equal to that of the incident light ($E = E_0$)
3. **Anti-Strokes scattering**: The light interaction with the molecule ends up with net exchange energy of one molecular vibration if the light photon gains vibrational energy from the molecule the frequency of the scattered light ends up being more than the incident light ($E = E_0 + E_v$)

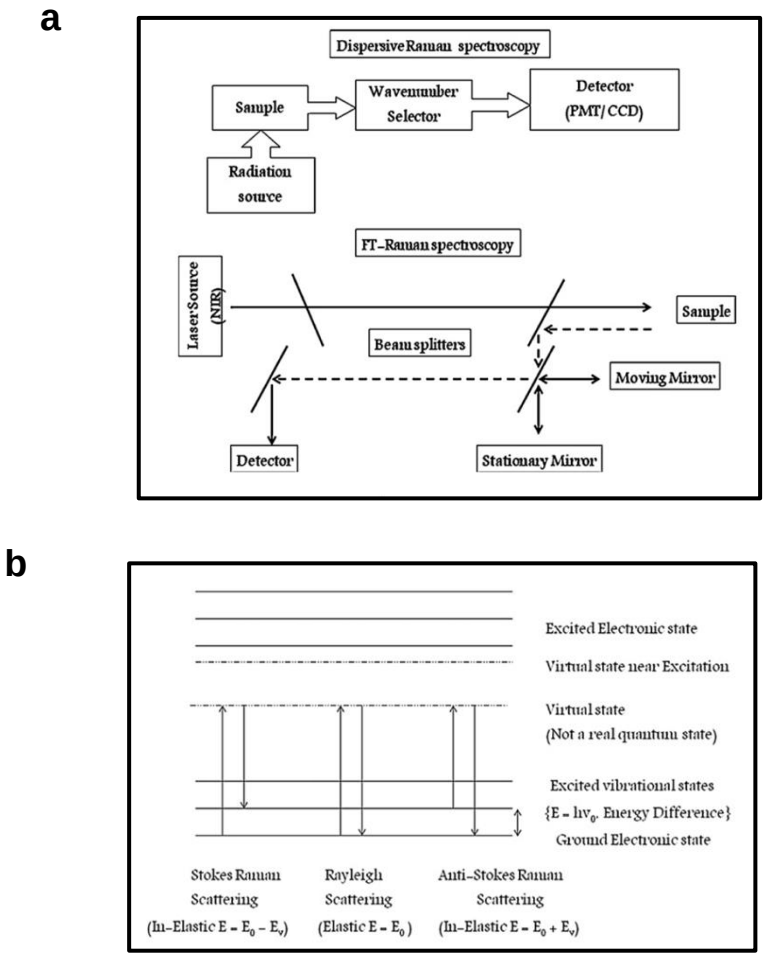


Fig. 3. 2 | Raman instrumentation. (**a**), **Raman mechanism of scattering** (**b**).[38]

3.1.3 BET Surface Area Analysis

BET is a method used to determine the S.S.A of powder by incorporating physical adsorption of a gas on the surface of the solid and then calculating the amount of adsorbed gas that corresponds to monolayer coverage on the surface. The physical adsorption results in weak forces is known as the Van der Waals forces between the adsorbate gas molecules and the adsorbent surface area and chemical adsorption results in strong interactions of the adsorbate gas molecules with the surface/inner surface, this analysis is carried out using nitrogen gas with the amount of gas adsorbed being determined via continuous flow or volumetric procedure.[50]

Classification of physisorption isotherms can be grouped into six types as shown in **Fig. 3.3**, type I isotherm are mostly found in microporous solids with small external surfaces, the amount of absorbed gas approaches a limiting value which is governed by assessable micropore volume rather than the internal S.S.A., the steep uptake at very low pressures is due to enhanced absorbent-adsorptive interactions in narrow micropores, type I(a) isotherms are found in microporous materials with (∼1 nm), type I(b) isotherms are found in materials with pore size distributions over a broader range of wider micropores (<∼2.5 nm). Type II isotherms are mostly governed by physisorption of gases on macroporous or nonporous adsorbents they shape is a result of unrestricted monolayer-multilayer adsorption up to high pressures. At point, B represents the completion of the monolayer coverage and at the gradual increasing curve represents the amount of overlap between the monolayer coverage and the onset multilayer adsorption which increases without limit as pressure approaches 1. Type III isotherms there is no point B hence no monolayer coverage, the adsorbed molecules are congested on the favorable sites of a macroporous or nonporous solid resulting in a thickness of the multilayer tending to increase without limit when pressure approaches 1. Type IV isotherms correspond to mesoporous adsorbents, these are governed by the adsorbent adsorptive interactions and molecules in the condensed state., firstly the monolayer -multilayer adsorption on the mesopore walls similar to the type II isotherm then followed by pore condensation. Type IV(a) capillary condensation is coupled by hysteresis, this occurs if pores exceed ∼2.5 nm and with smaller width Type IV (b) isotherms which are governed by conical and cylindrical

mesopores that are closed at the end. Type V isotherms shape is similar to that of type III are given by weak adsorbent-adsorbate interactions, at high-pressure molecular clusters form followed by pore filling and type Vi isotherms are governed by layer-layer adsorption on a highly uniform nonporous surface.[50]

Hysteresis loops are mainly occur due to capillary condensation, **Fig. 3.4 represents** the six types of hysteresis loops. H1 is found in materials with a narrow range of uniform mesopores. H2 are found a solid with more complex pore structures that consider network effects, H2(a) many occurs in silica gels and mesoporous materials, H2(b) is associated with pore-blocking seen in mesocellular silica foams. H3 loops adsorption branch resembles that of type II isotherm usually observed for non-rigid aggregates of plate-like particles. H4 loop is similar to type I and II with the more pronounced uptake at low pressures being associated with filling of micropores, usually found in mesoporous materials. H5 loop is usually obtained from solids of open and partially blocked mesopores.

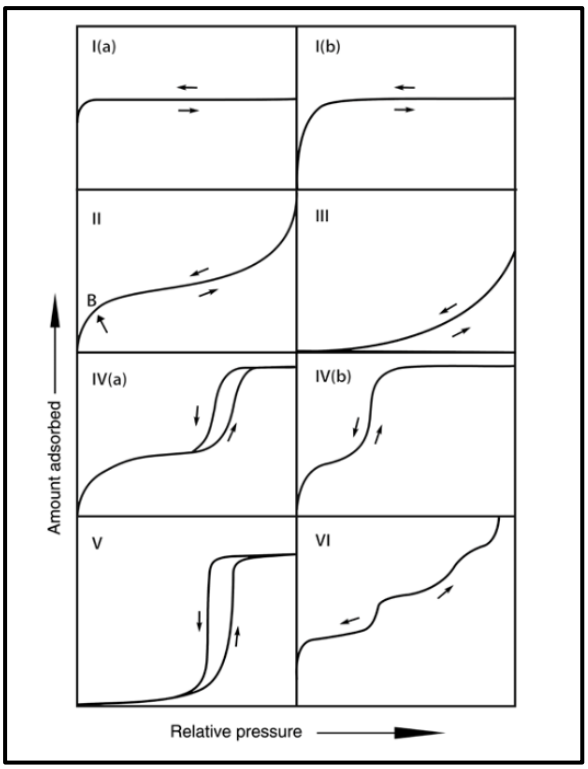


Fig. 3.3 | BET classification.[38]

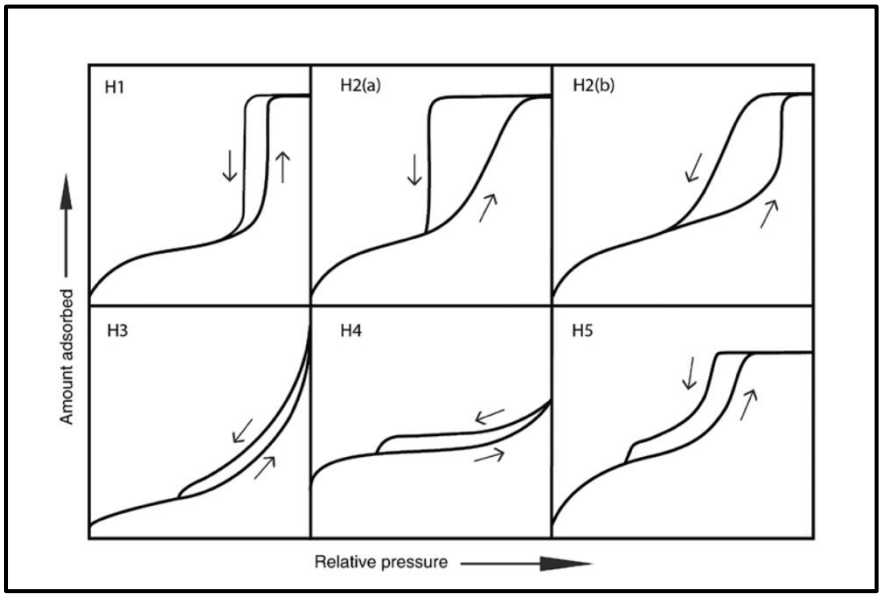


Fig. 3. 4 | BET Hysteresis classification.[38]

3.1.4 Scanning Electron Microscopy

SEM examines microscopic structure by scanning the surface of materials. The SEM image that is collected is formed by a focused electron beam that scans on the surface of the sample, it gives a depth of field giving 3D images of the morphology of the sample. The depth of field can reach 10^4 x magnifications. **Fig. 3.5** displays the basic schematic of the SEM diagram, the SEM components consist of an electron gun which operates at 0.1-30KV, were electrons are produced, these electrons pass through a series of lenses and apertures (condenser lens which produces a demagnified image than to an objective lens which is a probe forming a lens on to the sample) that hit the sample surface. The columns and chamber are evacuated by a pump, the electron beam is position is controlled by scan scan coils resting above the objective lens. A rastering image is produced which gives information about the defined area on the sample resulting in the electron-sample interaction with the signals produced detected by detectors.[73]

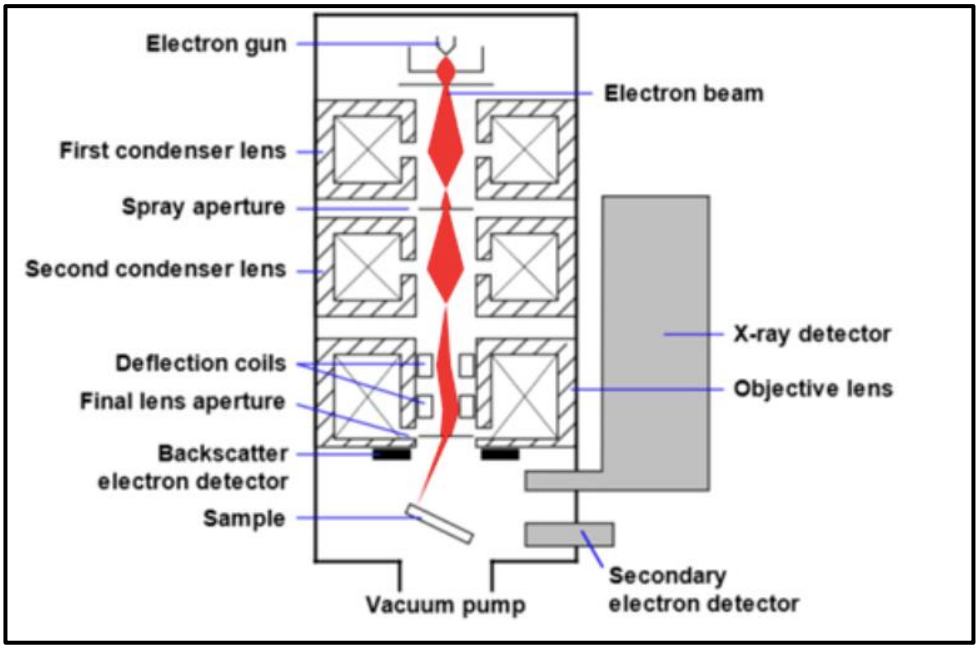


Fig. 3. 5 | Scanning electron microscopy diagram.[87]

3.1.5 Transmission Electron Microscopy

Transmission electron microscopy also known as TEM is used to study the internal micro and crystal structure of samples of which these samples need to be in a thickness range of 20-300 nm and uses a 200KeV. TEM generates images with high magnification and resolution than light microscopes. This high resolution is due to the short wavelengths of the electrons which are 10 000x shorter than of visible light.[73] The instrumentation consists of a light source, objective lens, condenser lens, specimen stage, and projector lens as shown in **Fig. 3.6**

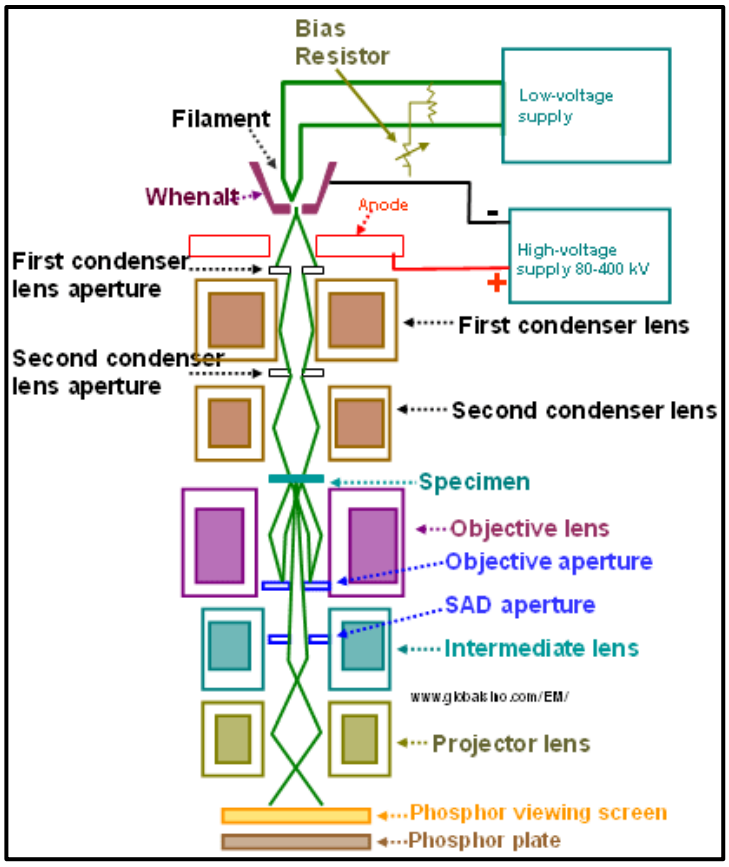


Fig. 3. 6 | Transmission electron microscopy diagram.[88]

3.1.6 X-Ray Photoelectron Spectroscopy

Introduction

XPS is a surface-sensitive technique since photoemissions without energy loss are restricted to only a few nanometers on the surface interface of the material and the vacuum, on the other hand, the x-rays penetrate the material at a greater depth resulting in the scattering of emitted electrons by electrons located within the depth of the material and the material and sample interface which limits the intensity of primary electron peaks to depths that depend on the emission energy of electrons. Therefore depending on the binding energy for an atom from which the photoemission originates, the maximum sampling depths for photons can be less than 10 nm.[51,91]

XPS is considered to be an electron spectroscopy technique and generally investigates the emission and energy analysis of low-energy electrons within the range of 20-2000 eV.[91]

In XPS electrons are observed in a notation called the spectroscopist notation, described employing quantum numbers. Transitions are usually labeled as nl_i where *n* represents the principal quantum number that takes integer values such as 1, 2, 3 etc. and *l* represents the quantum number which describes angular momentum and takes the integer values 0, 1, 2, 3, however, to simplify the notation the quantum number is usually assigned a letter s, p, d, f respectively.[44,91]

The role of utilizing XPS is to solve the following pertaining:

1. The chemical states present in an element
2. To obtain the spatial distribution of the materials in three dimensions
3. The type of elements present at the surface
4. Determine the amount of each chemical state of each element

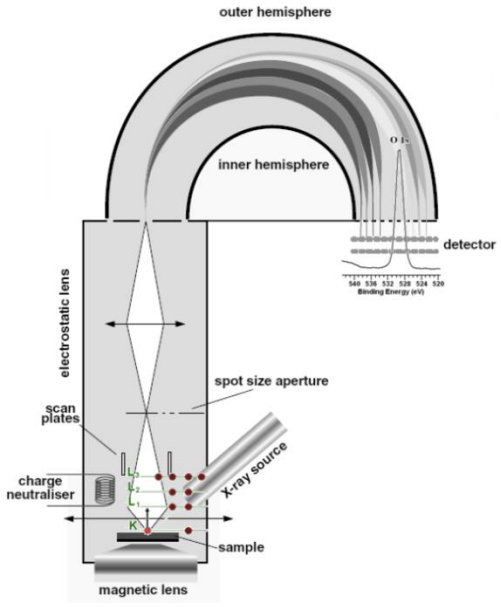


Fig. 3. 7 | Schematic of an XPS equipment.[92]

An XPS experiment contains.

1. An x-ray source that can generate photons
2. Vacuum chamber to allow an easy channel for electrons to move freely after being ejected from the sample
3. A transfer lens to help focus the beam into an energy analyzer
4. An energy analyzer and its function is to allow electrons of known or wanted energy to reach the detector
5. A stage to position the sample
6. A charge compensation mechanism used to prevent the dynamic buildup of negative charge generated by photoemissions of electrons.

Theory

The basic theory behind XPS involves removal of one singular core electron which is a special form of emission since it requires the removal of an electron from a core level by an X-ray photon of energy *hv*. Photoemissions occur when a photon of energy is transferred into the electrons located at the core area of an atom enabling electrons to gain kinetic energy to escape into the vacuum chamber. The obtained x-ray photoelectron spectrum is a sequence of measurements, were a certain amount of electrons at a particular energy and time interval are recorded. The objective is to measure the electrons emitted from an atom on the surface of a material as counts per second (CPs) as a function of kinetic energy. This allows for the measurement of different variations for electron intensities at varying energy furthermore aiding in quantifying to different electronic states present on material and thus revealing information about the surface composition.[45,91,92]

The XPS instrument measures the kinetic energy E_{ke} of the emitted photoelectrons and can be determined by the following equation.

$$E_{ke} = hv - E_{be} - \phi$$

Where the electrons located within the atom's environment specific to a parent element and atomic energy level are referenced as binding energy E_{be}, X-ray photon of energy as hv and the work function ϕ, which is the minimum amount of energy required to remove an electron from a solid to a point in the vacuum and sample interface. The quantities on the right-hand side of the equation are classified as measurable, while the kinetic energy of a material is fundamental in XPS analysis which gives the primary photoelectron peaks and is dependent on the photon energy of the X-rays used and therefore not considered an intrinsic material property.[52,92]

A typical process is shown below (**Fig. 3.8** (**a**)) where a 1s photoelectron is ejected form a k shell. Once an XPS spectrum has been generated, it contains both primary photoemission electron signal and inelastically scattered signal. The primary photoemission signal (**Fig. 3.8** (**b**)) is made up of the ejected electrons from the depth

of the material to the vacuum/sample interface for which no energy loss followed by photoionization and inelastic scattering causes a reduction in kinetic energy, the photoelectron ejected from its initial excitation energy which is using assigned as the background.[52,92]

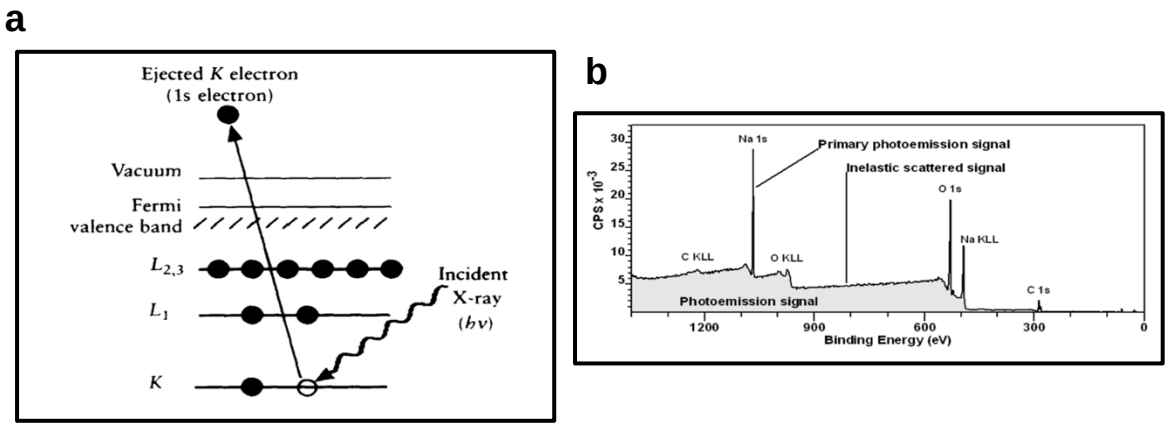


Fig. 3. 8 | Schematic of an XPS equipment. (**a**) and Photo emission signal due to inelastic scattered signal which is different form the primary photoemission signal that give rise to the elemental peak (**b**).[45,92]

3.2 Electroanalytical Techniques

3.2.1 Cyclic Voltammetry

CV is one of the most popular and most come techniques in electrochemistry used to investigate the reduction and oxidation process of molecular species, it is deemed appropriate analysis of possible systems of interest to battery technologies and to obtain desirable information for secondary batteries. CV provides a method to understand and determine the transfer coefficient, rate constants and kinetics of an electrode process, usually, the fast rate processes are of interest for battery development, thus serves as a tool to unravel complex electrochemical systems. **Fig. 3.9** depicts traces which are called cyclic voltammograms, the x-axis represents the applied potential/voltage (*E*) which is a parameter imposed by the system while the y-axis is the response as current (*i*). There are mainly two conventions used to report CV data, as indicated in **Fig. 3.9** (**a**), each curve contains an arrow indicating the direction in which the potential/voltage is swept to record the data. The sweep rate also known as scan rate with the units *v*, it controls the speed of the applied potential upon scanning and during an experiment, the potential is varied linearly at a given sweep rate. The direction of the arrow is the forward scan called the cathodic trace (reduction) then followed by the reverse scan known as the anodic trace (oxidation). The peaks obtained during the scan are called redox peaks due to the oxidation/reduction of a species.[9,53]

CV provides quantitative and qualitative information on the electrode processes. A reversible diffusion-controlled reaction represented in **Fig. 3.9** (**b**) shows symmetrical pair of current peaks and the difference between the anodic and cathodic peak potentials known as the peak-to-peak separation (ΔE_p)

$$\Delta E_p = \frac{2.3\ RT}{nF}$$

This value is independent of the voltage sweep. The chemical reversibility is determined if the analyte is stable upon reduction and can be reoxidized, this refers to the electron transfer kinetics between the electrode and the analyte. For quasi-reversible processes, the current peaks are separated with less sharp peaks that are more rounded as shown in **Fig. 3.9** (**c**) The voltage of the current peak is dependent on the voltage sweep rate with very high ΔE_p values. The irreversible process produces a single peak as shown in **Fig. 3.9** (**d**) it also has the voltage of the peak current dependent on the sweep rate.[9,53]

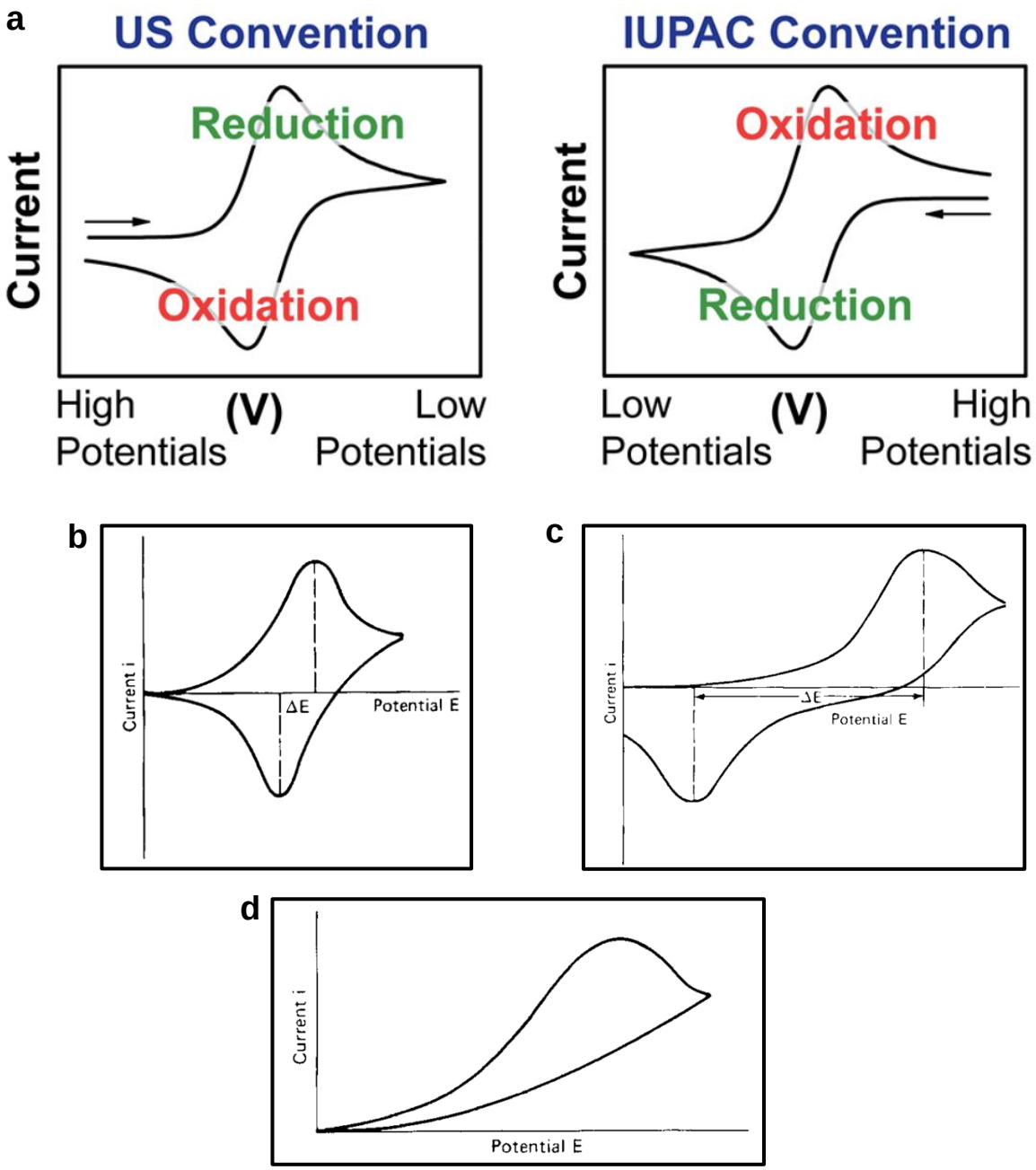


Fig. 3. 9 | Cyclic Voltammetry. Two methods used to report CV data (**a**), CV of reversible diffusion-controlled process (**b**), CV of quasi-reversible process (**c**), CV of irreversible process (**d**).[42]

3.2.2 Chronopotentiometry

Is the study of a short-lived voltage window at an electrode upon which is imposed a constant current. A current is applied to an electrode and then causes the electroactive species to be reduced, take for example:

$$\text{Oxidation (O)} + ne \rightleftarrows \text{Reduction (R)}$$

Upon applying current the potential of the electrode shifts to values that resembles redox couples and varies with time as the $\frac{[O]}{[R]}$ concentration ratio changes at the surface of the electrode. As for reduction, at the electrode, when the concentration of O drops to zero, the flux of O becomes negligible to receive all the electrons forced across the electrode-electrolyte interface, the cathodic reaction needs to commence and a sudden change in potential occurs and this is known as the transition time **Fig 3.10.**[9]

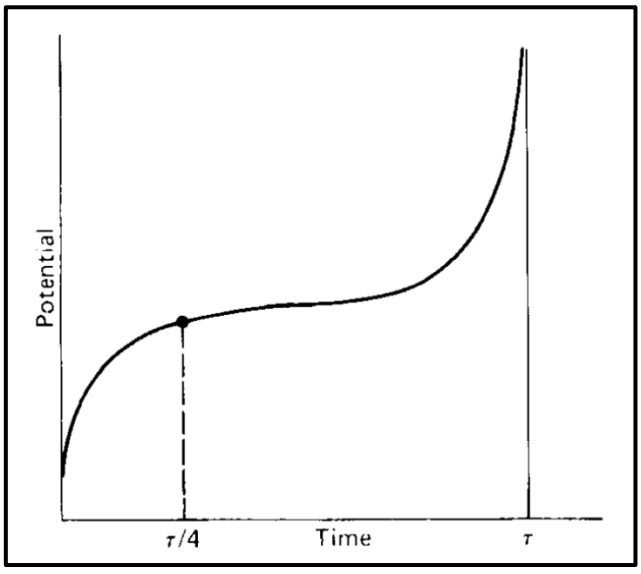


Fig. 3. 10 | Potential curve. at constant current for reversible reduction of active species.[9]

3.2.3 Electrochemical Impedance Spectroscopy (EIS)

This is a direct technique to interrogate the electrode processes is to measure the change in the impedance of an electrode by EIS.To match the impedance of the electrode-electrolyte interface to electrochemical parameters, an equivalent circuit has to be established to represent the dynamic characteristics of the interface **Fig. 3.10** in which a typical impedance for a charge-transfer process with kinetic control is displayed in were the capacitive component 1/wC is plotted vs a resistive component of the cell. **Fig. 3.12** (**a**) shows a plot of a kinetically controlled process only, the connection between the resistive and capacitive components yields a semicircle, with the top belonging to charge-transfer resistance r_{ct}, C_{nf} the non-faradaic capacitance, the intercept of the semi-circle and abscissa is the electrolyte resistance r_e. If both diffusion and kinetic control processes are present a plot shown in **Fig. 3.12** (**b**), the linear portion of 45 is were diffusion-controlled process are predominant.[9]

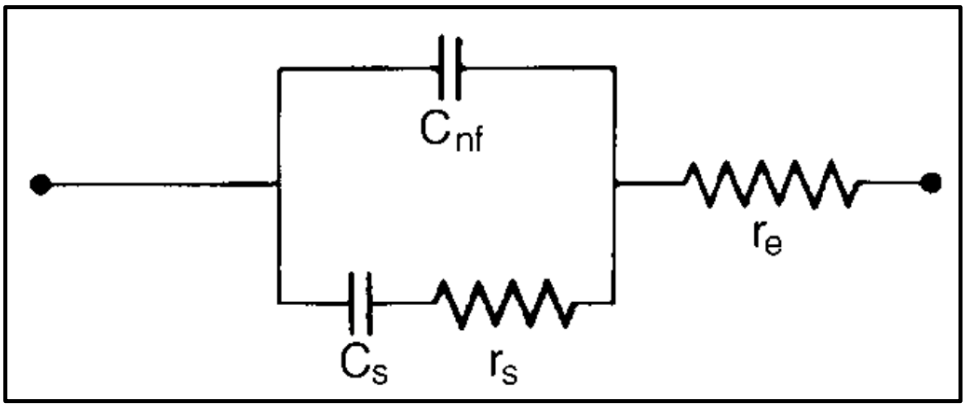
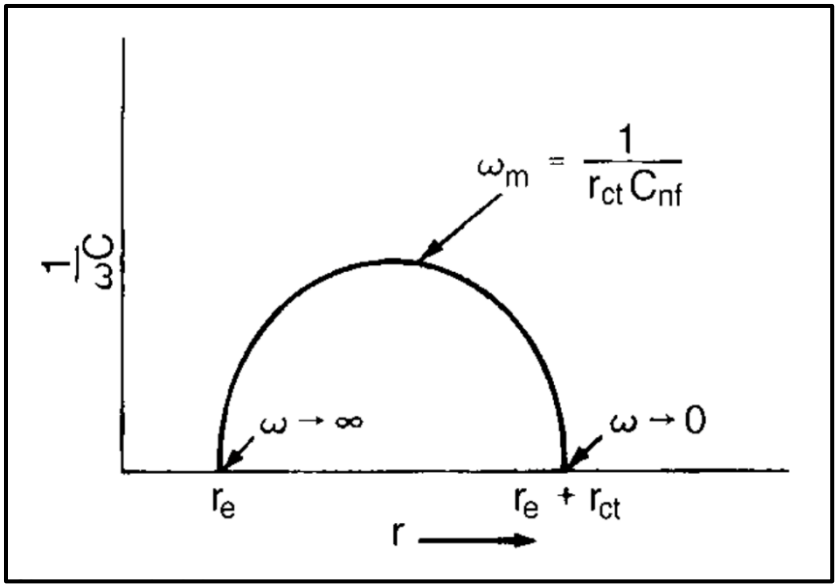


Fig. 3. 11 | Typical equivalence circuit. for a cell with an impedance that is kinetically controlled, r_s = faradic component, C_{nf} = non-faradic capacitance, r_e = electrolyte resistance.[9]

a



b

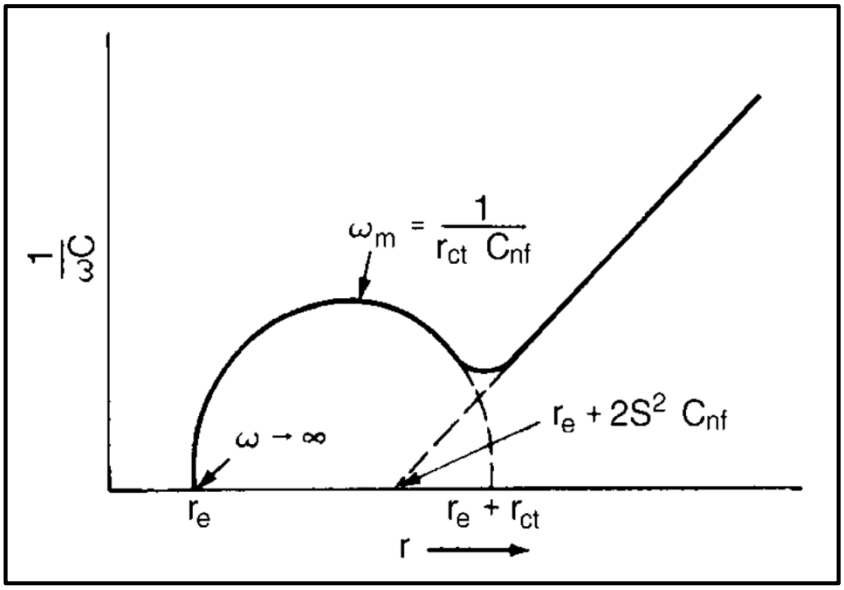


Fig. 3. 12 | Impedance Spectroscopy. Cell impedance for a charge-transfer process with kinetic control (**a**), Cell impedance for a charge-transfer process with kinetic and diffusion-controlled process (**b**).[9]

CHAPTER FOUR

Comparison of Pristine-MPF and MPF-CeO_2

4.1 Methodology

Materials. Sodium Fluoride, ammonium dihydrogen phosphate, manganese nitrate tetrahydrate, Cerium nitrate hexahydrate, potassium hydroxide, carbon black, polyvinylidene fluoride, sodium perchlorate and 1-methyl-2pyrrolodone (MPF) were purchased from Sigma-Aldrich.

4.1.1 Synthesis of Pristine-MPF (Mn_2POF)

Preparation of MPF. Dissolved 125.96 mg of NaF (3 mmol), 230.06 mg of $NH_4H_2PO_4$ (2 mmol) in 10 ml (separate beakers) deionized water and left to stir for 20 minutes/until fully dissolved. Then poured the solution containing $NH_4H_2PO_4$ into the beaker that contains NaF to make solution 1 and a clear solution was formed. For the preparation of solution 2, 502.01 mg $Mn(NO_3)_2.4H_2O$ (2 mmol) was dissolved in 20 ml

deionized water and left to stir for 10 minutes/until fully dissolved. Solution 1 was gradually added to solution 2 upon mixing and a gel-like whitish solution appeared and then left to stir for 12 hrs. at 1000 rpm at room temperature.[54,55,56,57] Microwave hydrothermal synthesis was carried out at 600 W, 180 ℃, 50 bar, while stirring at fan speed 2 and firstly ramped up for 10 minutes and then ran for 45 minutes.[58,59,60] The resulting product was tortilla brown in color, which was then centrifuged x5 with water then x3 with ethanol and left to dry at 60 ℃ for 12 hrs.[54,55,56] Then performed two-step solid-state synthesis, preheated sample at 350 ℃ for 4 h, then heated at 800 ℃ for 8 h. under Ar at a flow rate of 0.072 L/min under tube furnace. [54,55,56,57] The final product was tortilla to peanut brown.

4.1.2 Synthesis of MPF-CeO_2

Preparation of MPF-CeO_2. Obtained pristine-MPF and then performed a 2% coating with CeO_2, 500.00 mg of pristine – MPF (Mn_2POF) was added to a solution containing 25.23 mg $Ce(NO_3)_3.6H_2O$ in 50 ml deionized water and a coffee brown solution was formed. The mixture was kept under stirring for 30 mins and then sonicated for 30 mins at 25 ℃. The solution was adjusted to pH 12 with 2 M KOH and vigorously stirred for 2 h, forming a mocha brown solution. The product was centrifuged with H_2O until neutral pH, then dried at 60 ℃ for 12 h. and subsequently heated under air tube furnace at 250 ℃ for 2 h.[61], obtaining a wood to carob brown product.

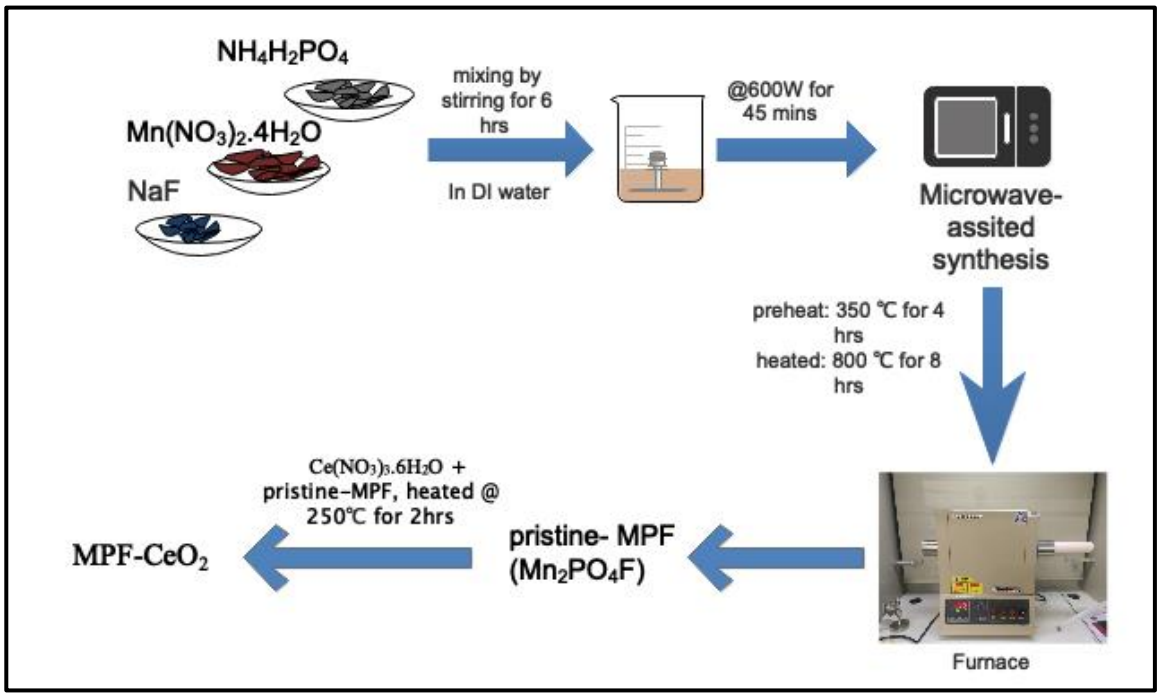


Fig. 4. 1 | Schematic representation of both preparation of pristine-MPF (4.1.1) and MPF-CeO_2 (4.1.2)

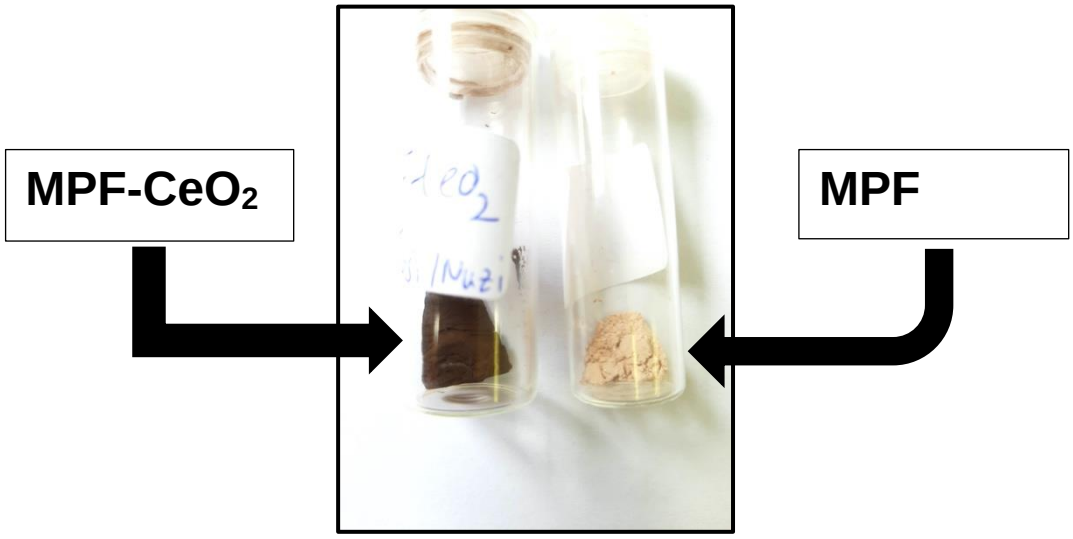


Fig. 4. 2 | Image showing finished products with their respective colours

4.1.3 Characterization

PXRD patterns were collected using Bruker D8-advance at NECSA with Cu Kα_1 = 0.154060 nm radiation source, the range was $15° \leq 2\theta \leq 110°$ in a 0.015° measurement step. The refinement data was analysed using TOPAS software.

Raman data was collected using a 514.5 nm (green) line from our Lexel Model 95 SHG argon ion laser.

FTIR was carried out using a Bruker Vecter 22 FT-IR spectrometer collected with the range of 500 t0 4000 cm^{-1}.

BET was collected using N_2 gas by desorption and adsorption using the Micrometric Tristar 3000 instrument at 77 K, the samples were degassed before analysis using N_2 at 423-473 k.

SEM was investigated by using the FEI Nova 600 instrument at 30kV at NIMSA, gold and carbon were used for plating.

TEM was analysed using a Tecnai Spirit T12 instrument at 120 kev. 2 mg od sample was dispersed in 5 ml of ethanol by ultra-sonication for about 15 minutes. Two drops of the solution were drop casted on a carbon coated copper grid, followed by drying at ambient temperature before commencing with the analysis.

XPS measurements were recorded at NIMSA using a Thermo ESCAlab 250Xi monochromatic Al K α (1486.7 eV), 300 W (X-ray power), 900 μm(X-ray spot size), 100 eV (Pass energy survey), 20 eV (Pass energy Hi-res) at < 10^{-8} mBar.

Electrochemical techniques were recorded using a BioLogic BCS-COM and SP-300 operating on a EC-Lab 11.3 BT-lab 11.2 software.

4.1.4 Electrode Processing

The positive electrode was prepared by mixing MPF or MPF-CeO_2, carbon black and PVDF (polyvinylidene fluoride) in a weight ratio of 80:10:10 by NMP, then casting the slurry on carbon paper. After drying at 80℃ for 12 hrs. MPF coin cell positive electrode had ~4 mg while MPF-CeO_2 had ~1.4 to 2.5 mg of active mass loading and as for the T-type cell MPF had ~2.1 mg and MPF-CeO_2 had ~1 mg of active mass loading.

4.1.5 Coin and T-type Cell Fabrication

Coin-cell Fabrication. CR2032 coin cells were assembled using the traditional method as shown in **Fig. 4.3** by utilizing a glass fibre separator, Zn foil as the anode (positioned on the negative case) and analyzed material coated on carbon paper as the cathode (positioned on the positive case). 4M $NaClO_4$ was used as electrolyte were $NaClO_4$ was dissolved in deionized water.



Fig. 4. 3 | Coin cell. Traditional coin-cell assemble.[89]

T-type cell Fabrication. A T-type-cell as indicted below in **Fig. 4.4 (a**) was assembled as described in **Fig. 4.4 (a**) by utilizing a glass fibre separator, Zn foil as anode (positioned on the negative case) and analyzed material coated on carbon

paper as cathode (positioned on the positive case). 4M $NaClO_4$ was used as electrolyte were $NaClO_4$ was dissolved in deionized water.

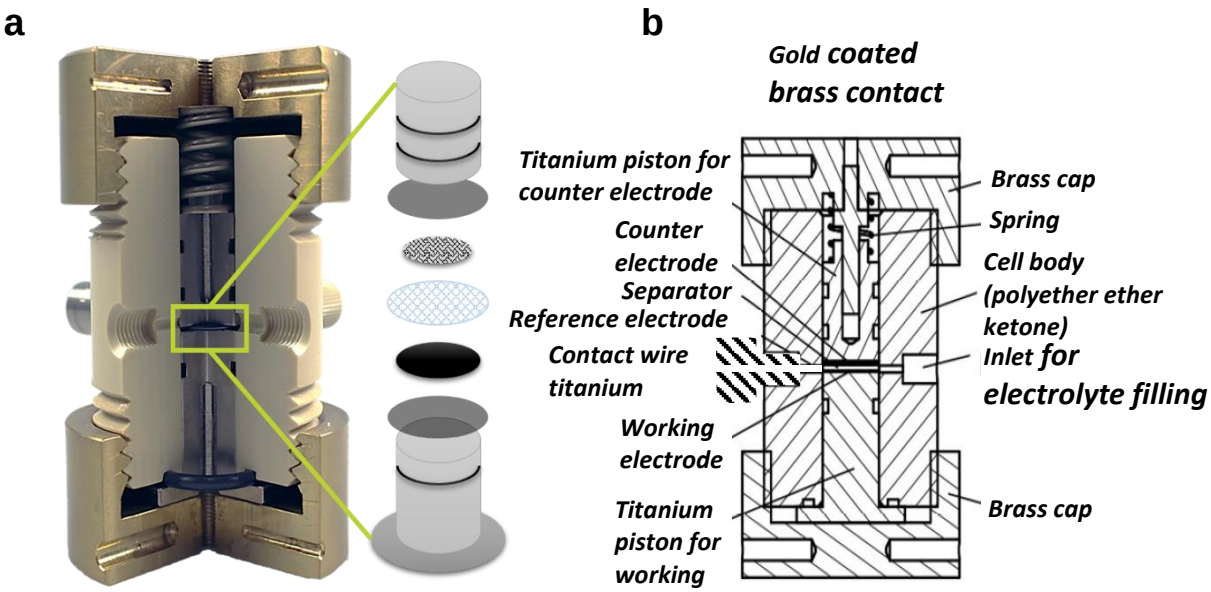


Fig. 4. 4 | T-type-cell. T-type-cell basic schematic (**a**), T-type-cell detailed schematic representation (**b**)

4.2 Results and Discussion

4.2.1 Materials characterization

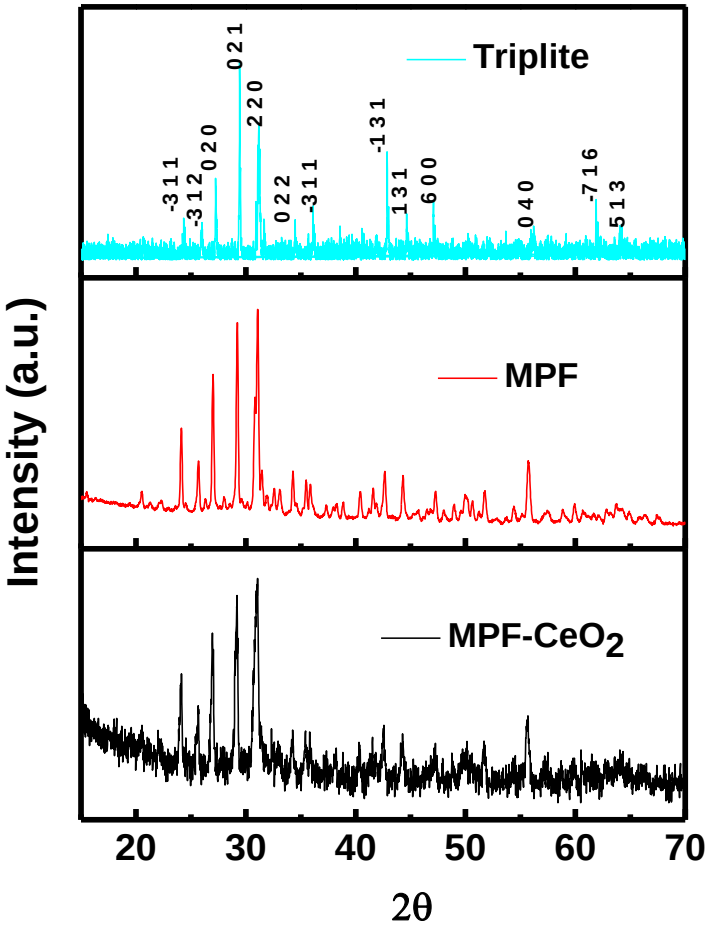


Fig. 4. 5 | PXRD Pattern comparison of Triplite, MPF, MPF-CeO_2

The above XRD patterns **Fig. 4.5** were determined using Cu Kα_1 = 0.154060 nm radiation which confirms that the phase pure Mn_2PO_4F was successfully synthesized as all the Bragg peaks can be fully indexed to a crystal structure of monoclinic symmetry corresponding to the space group C2/c (15), which is based on that of the triplite that was first structurally explored by Rea and Kostiner in 1972 of which they discovered triplite to have lattice parameters *a* = 13.410, *b* = 6.50960, *c* = 10.0940Å,

and β = 199.990°. it is clear from the comparison X-Ray diffraction that MPF and MPF-CeO_2 have the same peaks as mineral triplite, however, the peaks at 24.30° [-3 1 1], 31.33° [2 2 0] and 61.83° [-7 1 6] MPF and MPF-CeO_2 have a sharper intense peak compared to that of triplite, at 42.66° [-1 3 1] triplite has a much sharper intense peak, lastly, at 61.83° [-7 1 6] and 64.00° [5 1 3] these peaks are present in triplite but not purely visible for MPF and MPF-CeO_2. With this analysis, we can confidently deduce that MPF is triplite and that upon coating MPF with CeO_2 did not cause any changes in the phase or peak positioning of the original MPF, however, Rietveld refinement is needed to confirm if there are any changes in the position of the atoms in the lattice. Also, the analysis of the electrochemical behaviour will enlighten us on the best material for battery applications. **Appendix A3** displays the Rietveld refined peaks of both MPF (R_{exp}: 0.80, R_{exp}: 1.84, R_{exp}: 1.28) and MPF-CeO_2 (R_{exp}: 6.16, R_{exp}: 6.17, R_{exp}: 4.91), from the obtained refinement the lattice parameters which are summarized in **Table 4.1** for MPF are a = 13.42, b = 6.512, c = 10.11, and β = 119.99 with d spacing of 2.873 nm and a unit cell volume of 765.069 while MPF-CeO_2 lattice parameters are a = 13.40, b = 6.509, c = 10.09, and β = 119.99 with d spacing of 2.870 nm and the unit cell volume is 762.888. These results reveal that upon adding 2%-CeO_2 coating the lattice parameters changed by 0.1%, thus meaning that the coating does not shift the lattice positions of the atom but keeps the integrity of the material. The lattice strain (s) was also analysed, the analysis was conducted to determine the effects of CeO_2 by calculating the lattice strain, which is known to be related to the size of the particles. The lattice strain of MPF-CeO_2 is s_a = 0.104 %, s_b = 0.06 % and s_c = 0.126 %, meaning that at the coating of 2%-CeO_2 induces a very small lattice strain on the original structure (MPF).

Table 4. 1 : Parameters obtained from XRD patterns, interplanar

Sample	d (2 0 2)	a	s_a (%)	b	s_b (%)	c	s_c (%)
MPF	2.873	13.42		6.512		10.11	
MPF-CeO_2	2.870	13.40	0.104	6.509	0.06	10.09	0.126

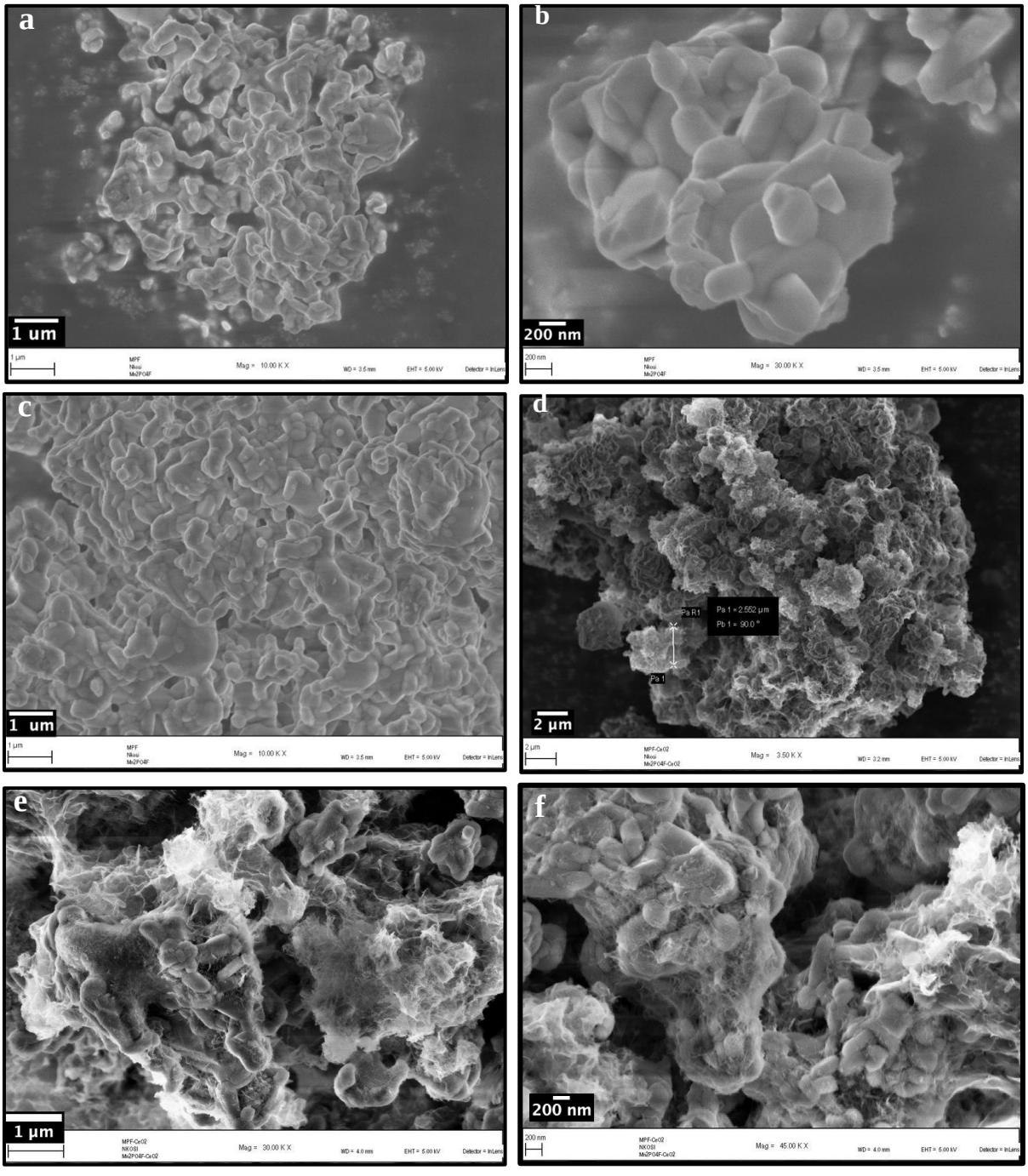


Fig. 4. 6 | SEM micrographs for MPF (a, b, c) and MPF-CeO_2 (d, e, f)

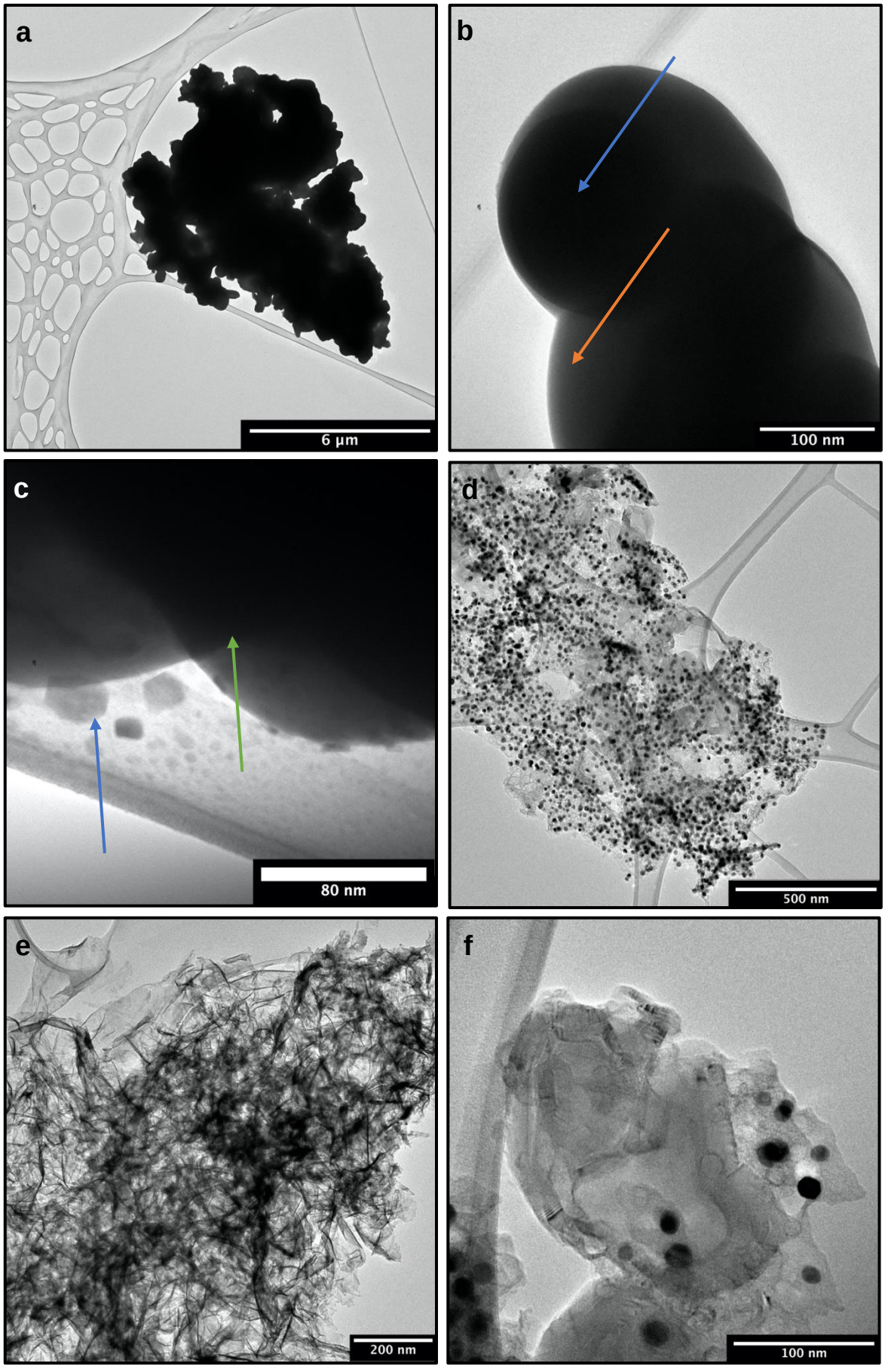


Fig. 4.7 | TEM micrographs for MPF (**a, b, c**) and MPF-CeO_2 (**d, e, f**)

Fig. 4.6 are the SEM micrographs of MPF and MPF-CeO_2, were **Fig. 4.6** (**a-c**) represent MPF appearing as nanosheets which are agglomerated and non-uniform with different particle sizes and morphologies, the average particle size was found between to be in the range 200 to 300 nm**.** In **Fig. 4.6** (**d-f**) are of MPF-CeO_2 observed as nanosheets with CeO_2 appearing as a spider-web like morphology covering MPF which is represented as white clumps on the grey substrate, this does indicate that the 2% coating by CeO_2 was achieved as both MPF and MPF-CeO_2 do not to look similar in morphology, however, as for MPF-CeO_2 it was impossible to determine the particle size distribution due to the grey-white color of the spiderweb-like coating formed by CeO_2.

The TEM micrographs were also obtained as shown in **Fig. 4.7** (**a-f**) for both samples. **Fig. 4.7** (**a-c**) represent TEM images for MPF, in image **Fig. 4.7** (**a**) they appear as one big particle with a darker shaded area running through the center and a lighter layer on the edges and as we look closely at the image (b), the particles seem to be stacked on top of one another with the blue arrow indicating the darker shaded layer and orange arrow the lighter shaded area, image (**c**) the green arrow indicating a layer which seems to be above the grey area, although we need a technique such as a beam tilting to be applied to further quantify this, also on the side of these two layers, there are smaller particles that do not make up the main particle indicated by the blue arrow, these could be due to impurities, starting reagent materials or even the actual material since the particle size distribution has a wide range of particle sizes. The TEM image of MPF-CeO_2 is shown in **Fig. 4.7** (**d-f**), image (**d**) shows a birds eye view of the sample with a dark shaded particles surrounded by a grey cloud, a closer look was taken in the image (**e**), the dark spots were recognized as the particles of the sample and the grey cloud confirmed in the image (**f**) to be the spider-web like morphology as seen from the SEM micrographs since it is covering the particles forming a protective layer in which CeO_2 acts as a coating to enhance the material stability and electrochemical performance. With this evidence 2%- CeO_2 coating was achieved.

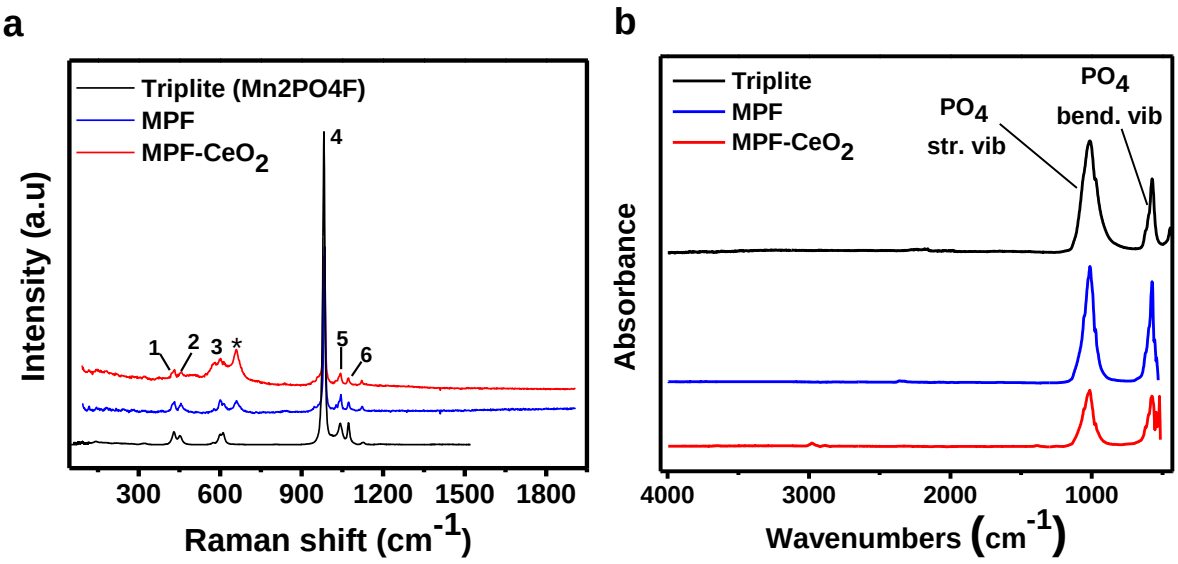


Fig. 4. 8 | Raman spectrum of MPF and MPF-CeO_2 (a), **Infrared spectrum** of MPF and MPF-CeO_2 (b)

The **Raman spectra** Fig. **4.8 (a**), was obtained using the 514.5 nm (green line) with the Raman bands summarized in **Table 4.2**. The points were collected at different regions of the sample with a few significant differences. Herewith in a comparison of the main Triplite sample, MPF and MPF-CeO_2 will be analyzed. For all the samples the spectrum is dominated by the phosphate group with the main Raman band which is very sharp and strong is centered at 980.5 cm^{-1} for Triplite, for MPF and MPF-CeO_2 at 983 cm^{-1}, this band is attributed to the *v1* vibration symmetric stretching of the phosphate unit. For Triplite the medium band at 1036 cm^{-1} is also located in MPF and MPF-CeO_2 at 1044 cm^{-1} with medium intensity and at 1040 cm^{-1} with a weak intensity respectively, this particular band corresponds to *v2* asymmetric vibration stretching of the phosphate unit. The weak band occurring at 1072 cm^{-1} for Triplite is also found in MPF at 1076 cm^{-1} with weak intensity and at MPF-CeO_2 1072 cm^{-1} also with weak intensity, this band is attributed to *v3* asymmetric stretching of the phosphate unit. For all samples the bands within the range 429-610 cm^{-1} can be grouped into two regions corresponding to different modes of the phosphate group, the range 429 and 458 cm^{-1} correspond to *v2* phosphate deformation and at 600 and 610 cm^{-1} correspond to *v4* phosphate deformation, the only difference is the peak indicated by a * observed at 664.24 cm^{-1}, this peak could be due to an impurity such as a minor byproduct of staring

material, it is a pity that we could not identify its origin. Thus comparison analysis of the Raman bands shows us that MPF and MPF-CeO_2 resemble that of Triplite, further solidifying our findings in PXRD patterns and PXRD-refinement. An **Infrared spectrum** (FTIR) was analyzed for both materials **Fig. 4.8 (b**) and was found to represent the Triplite sample reported in literature[35] which are characterized by absorption bands located between the regions 400 to 650 cm^{-1} which correspond to PO_4 bond vibration as well as lattice vibrations and stretching vibrational modes of the PO_4 tetrahedra within the region 1200 to 900 cm^{-1}.

Table 4. 2 : Raman Spectra

Sample	Raman Shift (cm^{-1})	Intensity	Vibration	Ref
Triplite	429 (1) 450 (2) 610 (3) 980.5 (4) 1036 (5) 1072 (6)	S W M Vs M W	*v2* Phosphate (deform) *v2* Phosphate (deform) *v4* Phosphate (deform) *v1* (symm str. Phosphate) *v2* (asymm str. Phosphate) *v3* (asymm str. Phosphate)	35
MPF	430 (1) 458 (2) 600 (3) 983 (4) 1044 (5) 1076 (6)	W W M Vs M W	*v2* Phosphate (deform) *v2* Phosphate (deform) *v2* Phosphate (deform) *v1* (symm str. Phosphate) *v2* (asymm str. Phosphate) *v3* (asymm str. Phosphate)	
MPF-CeO_2	430 (1) 454 (2) 600 (3) 983 (4) 1040 (5) 1072 (6)	W W S Vs W W	*v2* Phosphate (deform) *v2* Phosphate (deform) *v2* Phosphate (deform) *v1* (symm str. Phosphate) *v2* (asymm str. Phosphate) *v3* (asymm str. Phosphate)	

Table 4. 3 : Tabulated summary of BET data

Samples	Surface Area (m^2g^{-1})	Pore Volume (m^3g^{-1})	Pore Size nm
MPF	1.606	0.01140	20.96
MPF-CeO_2	16.98	0.1859	40.76

It is said that, surface area (S.A), pore volume and pore size will all influence the electrochemical performance of battery materials. **Table 4.3** sums up the BET analysis performed for both samples, these measurements were done to obtain information on the electrochemical active S.A, which is the area of the electrode that is accessible to the electrolyte for storage and charge transfer (double layer charging or pseudocapacitive), contributing to the capacitive nature of the material, therefore higher surface area constitutes a higher energy density. From the data, it is clear that MPF-CeO_2 has a higher S.A of 16.98 m^2g^{-1} than that of MPF at 1.606 m^2g^{-1}, also with a 95% (0.1859 m^3g^{-1}) greater pore volume than that of MPF (0.01140 m^3g^{-1}) and a pore size of 40.76 nm which is twice the size of MPF at 20.96 nm. These results give us an idea that MPF-CeO_2 will have the greatest electrochemical performance leading to a greater capacity over MPF and indicates that CeO_2 stabilizes the pristine-MPF structure whist offering more pores as charge transportation channels and storage as seen from the spider-web like morphology observed in SEM. The BET isotherm-plots were analyzed as shown in figure **Fig. 4.9** (**a, b**) both materials reveal a Type IVa classification characteristic of mesoporous materials, at pressures 0.8-1.0, there is a small Type H1 hysteresis loop which might be due to capillary condensation in the mesopores, this hysteresis is no surprise since it is observed for materials with pores wider than ~4 nm of which both MPF (20.98 nm) and MPF-CeO_2 (40.76 nm) exceed, followed by a sharp rise in N_2 gas adsorption volume suggesting the formation of secondary mesopores due to particle aggregation in which MPF-CeO_2 reaches to nearly ~350 cm^3g^{-1} of gas adsorption due to the CeO_2 coating that envelopes the material causing particle aggregation as seen in SEM **Fig. 4.6** (**d, e, f**) and TEM **Fig. 4.7** (**d, e, f**) micrographs.

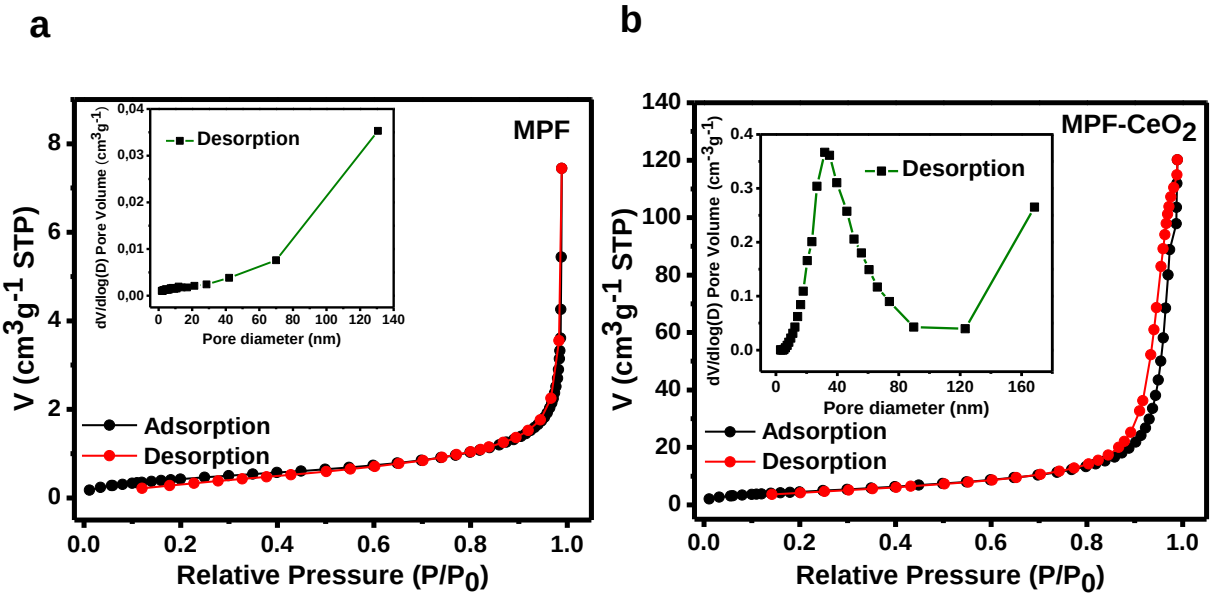


Fig. 4.9 | Brunauer-Emmett-Teller (BET) surface area analysis using N_2 adsorption-desorption studies, MPF (**a**) and MPF-CeO_2 (**b**) BET isotherm plots

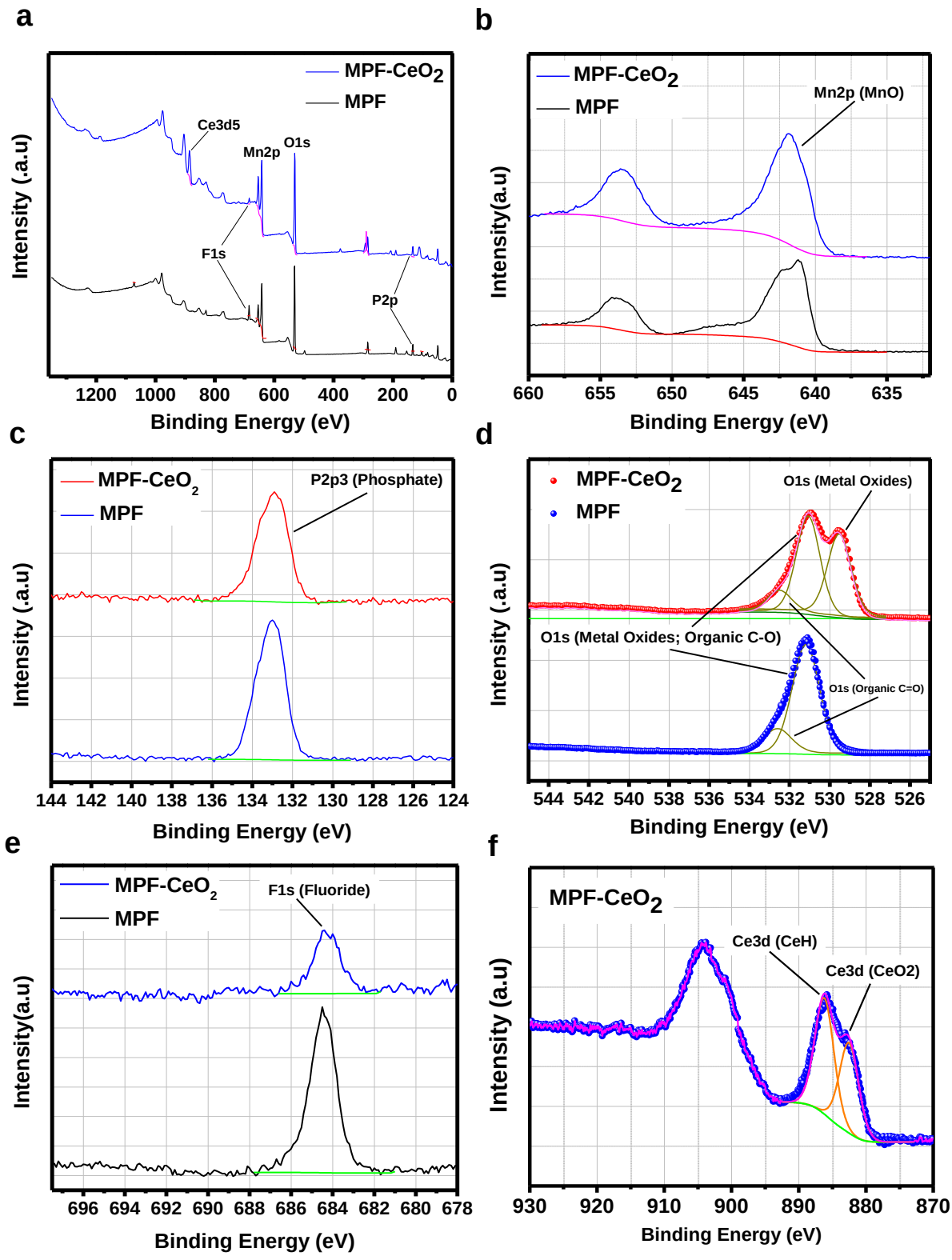


Fig. 4.10 | X-Ray Photo spectroscopy (XPS) of MPF. Elemental ID and quantification (**a**), Mn2p (**b**), P2p3 (**c**), O1s (**d**) and F1s (**e**)

Table 4. 4 : MPF and MPF-CeO_2 Elemental ID and Quantification

Name	Peak BE (MPF)	Peak BE (MPF-CeO_2)	Atomic % (MPF)	Atomic % (MPF-CeO_2)
O1s	531.4	530.7	48.3	55.9
Mn2p	642.1	642.1	13.2	16.5
P2p3	133.2	133.1	9.2	6.8
F1s	684.8	684.2	5.6	1.3
Ce3d5		885.0		2.7

Table 4. 5 : MPF and MPF-CeO_2 Peak ID and Quantification

Name	Peak BE (MPF)	Peak BE (MPF-CeO_2)	Atomic % (MPF)	Peak BE (MPF-CeO_2)
P2p3 (Phosphate)	133	132.9	13.7	6.9
O1s (Metal Oxides)		529.5		21.1
O1s (Metal Oxides, Organic C-O)	531.1	531.1	37.5	25.4
O1s (Organic C=O)	532.6	532.5	8	5.2
Mn2p (MnO)	641.5	641.8	12.1	15.6
F1s (Fluoride)	684.4	684.3	5.3	1.7
Ce3d (CeO2)		882.5		0.8
Ce3d (CeH3)		886.2		1.0

The XPS elemental analysis was done for MPF and MPF-CeO_2 displayed in **Fig. 4.10** with **table 4.4** and **table 4.5** representing the elemental ID (Survey scan), Peak ID, and quantification. The XPS analysis was done to understand the contribution of CeO_2 coating on MPF. **Fig. 4.10** (**a**) displays the comparison of both the survey scans with the elemental peaks O1s, Mn2p, P2p3, F1s and Ce3d5 being identified. **Fig. 4.10** (**b**) represents the element Mn2p, MPF has Mn2p (Manganese Oxide) positioned at 641.5eV with 12.1 % atomic content and MPF-CeO_2 has the Mn2p (Manganese Oxide) peak positioned at 641.8eV with atomic content 15.6 %, this means that the addition of CeO_2 does not interfere with Mn2p, since both peaks have the same binding energy. For both materials, the most prominent peak belongs to O1s **Fig. 4.10** (**d**), MPF has O1s (Metal Oxides, Organic C=O) peak positioned at 531.1eV with 25.4 % atomic content and O1s (Organic C=O) peak positioned at 532.6eV with 5.2 % atomic content. As for MPF-CeO_2 upon deconvolution the O1s (metal oxides, Organic Oxide) peak appear to be split in two, the first O1s (metal oxides) positioned at

529.5eV with 21.1% atomic content and the second O1s (metal oxides, Organic Oxide) peak is positioned at 531.1eV with 25.4% atomic content, this means that CeO_2 causes the MPF metal oxide peak to split and its electrochemical performance shall be studied in **chapter 4** to underline its significance. The identification of Mn2p and O1s on both materials confirm the presence of the manganese atoms that lie at the centers of the highly distorted octahedra are coordinated by four O atoms which were reported under literature review in **Chapter 2.6,** XPS confirms that Mn and O are both bonded together to form metal oxides. The phosphate P2p3 (**Fig. 4.10** (**c**)) for MPF is positioned at 132.9 eV with a metal content of 13.7%, comparing this phosphate with that of MPF-CeO_2 at 132.9 eV with a metal content of 6.9%, reveals that coating by CeO_2 does not distort the phosphate complex, this confirms the presence of the phosphate tetrahedra discussed in **Chapter 2.6**. The Fluoride F1s peak for MPF is positioned at 684.4eV with 5.3% atomic content and for MPF-CeO_2 is positioned at 684.3eV with 1.7% atomic content, both are the same, CeO_2 did not distort the Fluoride bonding. lastly, for MPF-CeO_2 the deconvoluted Ce3d (CeO_2) is positioned at 882.5eV with 0.8% atomic content and another Ce3d belonging to CeH is positioned at 886.2eV with atomic content 1.0%. therefore, with this analysis coupled with XRD, Raman and FTIR confirm that we have successfully synthesized mineral triplite (Mn_2PO_4F) using the microwave method coupled with 2% CeO_2 coating.

4.2.2 Electrochemical Characterization

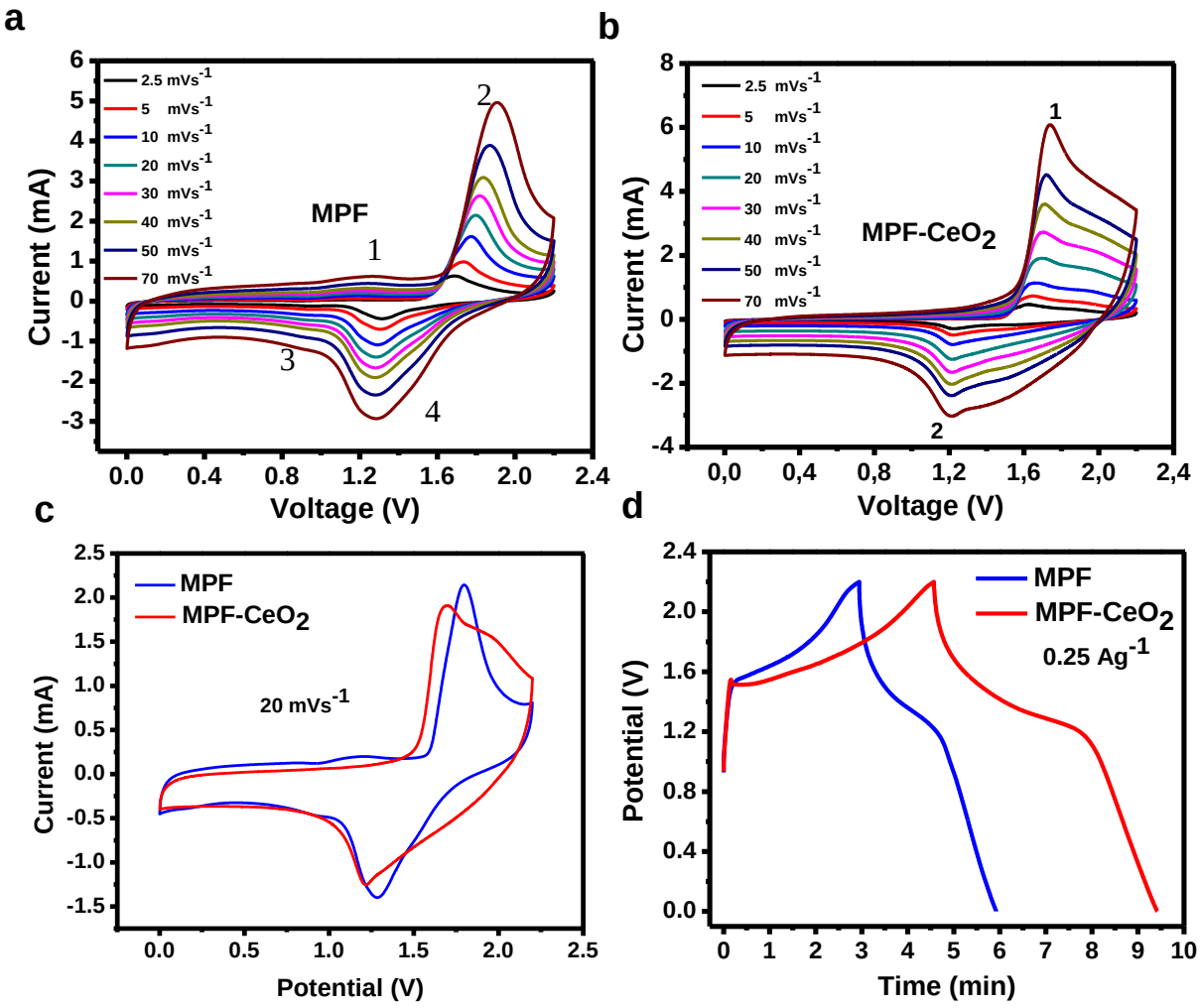


Fig. 4. 11 | Electrochemical behaviours of MPF and MPF-CeO_2 batteries with 4 M $NaClO_4$ as electrolyte. Cyclic voltammograms (CVs) at 2.5 to 70 mVs^{-1} MPF (**a**), MPF-CeO_2 (**b**), CV comparison at 20 mVs^{-1} (**c**) and galvanostatic charge-discharge (GCD) curve comparison for both MPF and MPF-CeO_2 at 0.25 Ag^{-1} (**d**)

In commencing the electrochemical studies for both materials it is necessary to state that to date there is no known literature pertaining the investigations of MPF electrochemical behaviors and performance, we will attempt in doing so using various examples from similar manganese-based materials. CV was first investigated. **Fig. 4.11 (a and b)** shows the CV curves for MPF **(a)** and MPF-CeO_2 (**b**) respectively in 4M $NaClO_4$ electrolyte fabricated using the T-type cell with a voltage window of 0-2.2V. Within the first observation, MPF with two pairs of oxidation/reduction peaks and MPF-CeO_2 with one pair of oxidation/reduction peaks. From 0 to 1V both materials

CVs have a capacitive shape and after 1V they resemble a battery-type material with redox peaks signifying oxidation and reduction of species. For MPF **(a)** both anodic peaks as the sweep rate is increased the peaks begin to broaden and start to shift towards higher potentials appearing within the range of 0.9-1V (Peak 1) and 1.69-1.79V (Peak 2), this might be due to increased polarization at higher sweep rates and the cathodic peak appearing at 0.9V (Peak 3) and 1.23V (Peak 4), these oxidation/reduction peaks are corresponding with the galvanostatic charge-discharge plateaus observed in **Fig. 4.11 (d)**. MPF-CeO_2 **(b**) also has a similar resemblance to MPF CVs, with peak broadening and shifting as sweep rate is increased, however, the shape is slightly more pronounced and reaches a slightly higher current at about 6 mA at 70 mVs^{-1}, although MPF has a better CV profile, this, however, with our support data from BET this means that MPF-CeO_2 will have more ions pass through the channels of the material and the fact that it has a high mesoporous size than MPF in which we can assume that MPF-CeO_2 will have a much higher capacity than of MPF, This assumption will be further illustrated under electrochemical performance. As the sweep rate increases the anodic peaks shift to higher potentials from 1.63-1.75V with the cathodic peaks occurring at 1.21V, these oxidation/reduction peaks are also corresponding with the galvanostatic charge-discharge plateaus observed in **Fig. 4.11 (d)**. The comparison CV curve is displayed in **Fig. 4.11 (c)** at 20 mVs^{-1}, just to further highlight the difference between the two, confirming that MPF-CeO_2 is more slightly pronounced than MPF, while MPF has two pairs of oxidation/reduction peaks and MPF-CeO_2 with one pair of oxidation/reduction peaks. For MPF It has been proposed that the anodic and cathodic peaks represent the oxidation and reduction of Mn from Mn^{2+} to Mn^{3+} (CV peak 1 and 3) Mn^{3+} to Mn^{4+} (CV peak 2 and 4), this indicates a presence of two phases undergoing structural transition highlighted in red. The galvanostatic charge-discharge curve comparison is highlighted in **Fig. 4.11 (d)** at 0.25Ag^{-1}, it is clear that both materials have a battery like properties based on the redox peaks, it is also evident that the 2% coating of CeO_2 on MPF did not affect the redox peaks, however, it improved its discharge time to 9.5 mins then that of MPF at 6 mins, these results solidify the slightly higher current observed in CV and pronounced peak broadening for MPF-CeO_2, therefore indicating that it will have a higher capacity (energy density) than MPF.

The proposed mechanism for Mn^{2+} to Mn^{3+} and from Mn^{3+} to Mn^{4+} is as follows:

$$Mn_2PO_4F_{(s)} + 2NaClO_{4(aq)} \longrightarrow Na_2MnPO_4F_{(s)} + Mn(ClO_4)_{2(aq)} \quad (1)$$

$$Na_2MnPO_4F_{(s)} \underset{+2e}{\overset{-2e}{\rightleftharpoons}} MnPO_4F_{(s)\ (g)} + 2Na^{+}_{(aq)} \quad (2)$$

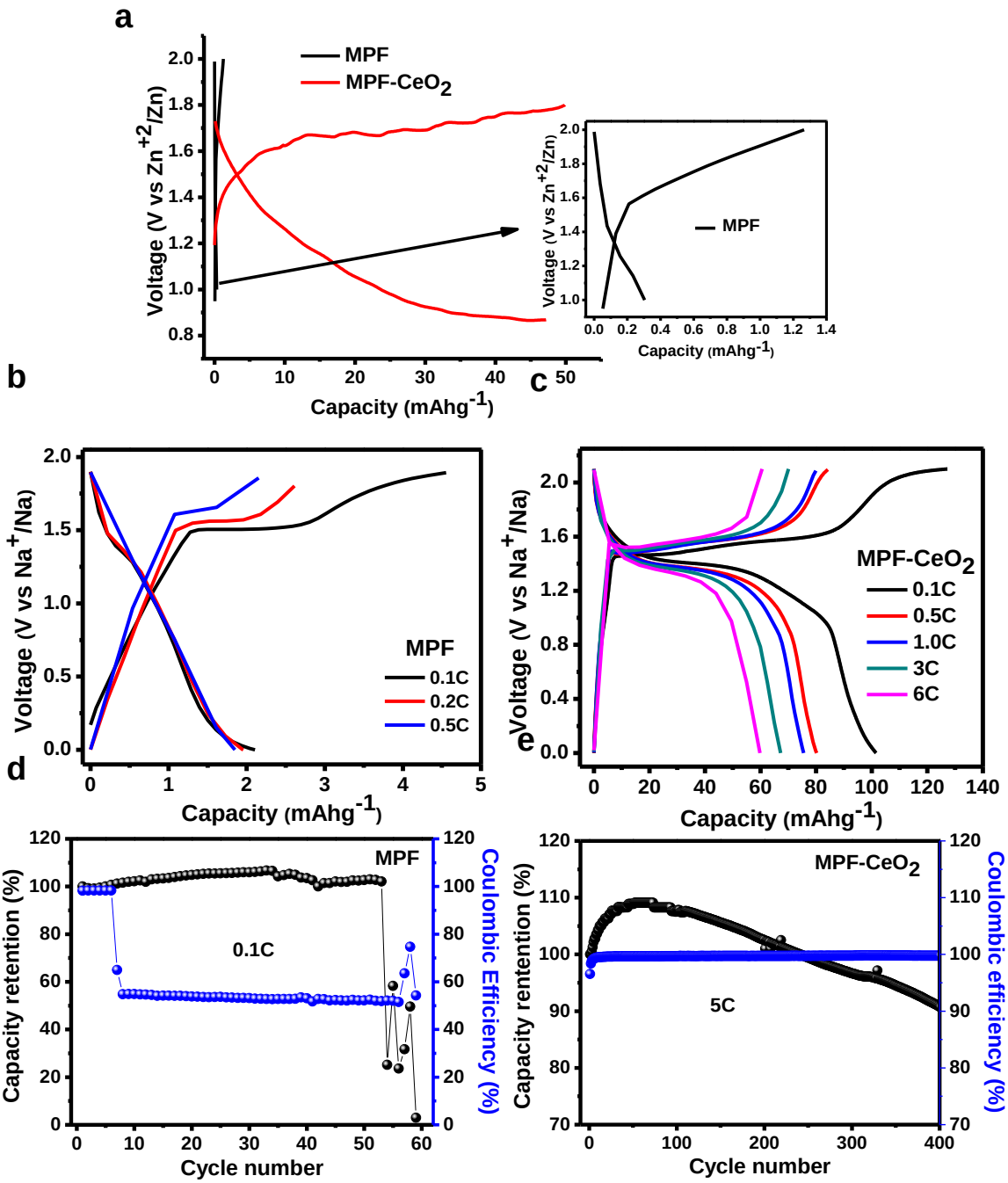


Fig. 4. 12 | Electrochemical performance of MPF and MPF-CeO_2 batteries with 4 M $NaClO_4$ as electrolyte. Charge/discharge curve comparison of MPF and MPF-CeO_2 coin-cell battery at 0.1C (**a**), Rate performance of MPF at 0.1, 0.2 and 0.5C using a T-cell battery (**b**) , Rate performance of MPF-CeO_2 from 0.1C to 6C using a T-cell battery (**c**), cyclic performance of MPF using T-cell battery (**d**), cyclic performance of MPF-CeO_2 using T-cell battery (**e**)

The electrochemical performance of MPF and MPF-CeO_2 was investigated as shown in **Fig. 4.12** (**a to e**) with 4 M $NaClO_4$ as electrolyte. To understand the electrochemical performance of both these materials the first tests were conducted using a coin-cell battery at a rated capability of 0.1 C **Fig. 4.12** (**a**), at 0.1C MPF charged and discharged at a voltage window of 0.85-2 V, had a discharge capacity of 0.3088 $mAhg^{-1}$, this is the first time in which MPF has been studied as a battery material and the capacity obtained is very poor, whilst MPF-CeO_2 charged and discharged at a voltage window of 0.85-1.8 V had a discharge capacity of 47.08 $mAhg^{-1}$ which is a drastic increase as compared to the parent material MPF, these results are in agreement with the electrochemical behaviours observed previously in **Fig. 4.11**, were MPF-CeO_2 had a higher response current and longer discharge time which does correlate with obtaining a higher capacity, however, these results are extremely far apart in comparison to what we had anticipated. This lead us to devise a new strategy in analyzing the performance of the material, one of our postulations was on speculating that the coin-cell packaging did not maximize the capacity obtained as discussed in **Chapter 2.4.3** under **battery engineering and design**, therefore we introduced the T-cell battery since manual packaging and screwing the components closely together is more efficient. The T-cell battery results obtained for MPF **Fig. 4.12** (**b**) charged and discharged at a voltage window of 0-1.9V rated at 0.1 C, 0.2 C and 0.3 C had a discharge capacity of 2.11, 1.9 and 1.85 $mAhg^{-1}$ respectively which is a slightly better value than that obtained from the coin-cell, however still very poor, whilst MPF-CeO_2 charged and discharged at a voltage window of 0-2.0V rated at 0.1C, 0.5C, 1C, 3C, and 5C had discharge capacities of 101.61, 80.18, 75.53, 67.19, 59.78 $mAhg^{-1}$ respectively. The results obtained were outstanding especially at 0.1 C with a 46% improvement in discharge capacity compared to using a coin cell. MPF-CeO_2 remains the best electrochemically performing material which does indicate that 2%-CeO_2 coating enhances the electrochemical performance of MPF inducing high mesoporous pores and size, capable of achieving high capacities. Thus MPF-CeO_2 is capable of even achieving higher capacities if the electrolyte and anode material are optimized.

The last step was determining the cyclic performance to observe material stability over a period of cycles, the capacity retention for MPF **Fig. 4.12** (**d**) went from 100% to 60% in just 6 cycles and remained at 60% until 55 cycles before crashing with a coulombic efficiency $\pm$ 99 %, this just goes to show that MPF alone is not a good battery material, although in the CVs it resembles battery-like behavior, but because of the low spin Jahn Teller distortions and Mn dissolution with the presents of oxygen evolution during charging and discharging lead to the collapse of the material. The capacity retention for MPF-CeO_2 **Fig. 4.12** (**e**) was rather interesting to observe, the 1st cycle at 100% increased to 109% in the 73rd cycle the reason of the increase may be due to the formation of the SEI (solid electrolyte interface), the periodic activation of the active material[62] and the suppression of oxygen evolution by CeO_2 coating as discussed in **Chapter 2.7.1.** Thereafter started to decrease drastically to 90% of its initial capacity then it collapsed at the 400th cycle with the coulombic efficiency remaining at $\pm$ 99% which is an improved columbic efficiency compared to MPF. This, however, suggests that CeO_2 did enhance the electrochemical performance but did not maintain capacity upon cycling. This was rather a strange observation since we had initially thought that the 2% coating by CeO_2 will improve its stability, however, it has been reported by G.Fang *et al*.[63] that manganese-based aqueous ZiBs cathode materials suffer from manganese dissolution that leads to capacity decay of the battery as well as depressed reaction kinetics are still a major obstacle in many Mn containing compounds. Furthermore X.Wu *et al*.[64] upon investigating the cyclic performance of $ZnMn_2O_4$ they discovered a similar initial capacity retention increase during cycling and then a sharp decrease in capacity similar to what we observed for MPF-CeO_2 of which they attributed it to oxidation of Mn^{2+} and the disproportionation reaction of MnOOH. Interestingly enough even M.H Alfaruqi *et al*.[65] and H.Pan et al.[66] upon investigating cyclic performances of γ-MnO_2 and α-MnO_2 respectively they both concluded that the capacity fading is most likely due to the Mn dissolution rather than structural distortion of MnO_2. G.Fang *et al*.[63] further went on to suggest incorporating potassium (K^+) ion to intrinsically stabilize Mn based cathodes, their results revealed at 1 Ag^{-1} α-MnO_2 (MO) obtained a discharge capacity of 50 $mAhg^{-1}$ after 200 cycles while KMO expressed an impressive durability over 1000 cycles and remained at 150 $mAhg^{-1}$. With, we assume that although the coating of CeO_2 on MPF was supposed to suppress the Mn dissolution. This means that CeO_2 suppresses the Mn dissolution

for 400 cycles (expanding the life cycle) but stills suffers from further Mn^{2+} dissolution (leading to capacity fading). However, more concrete explanations are needed in order to support and scrutinize our postulations, experiments such as in-situ/Operando Synchrotron-based X-ray techniques used to observe microstructural changes in electrode materials, complicated reaction mechanisms, working and degradation mechanisms of electrodes and possible side reactions during charging and discharging a battery. Another method is Tomography which is a techniques that allows nondestructive 3D imaging at various scales using an X-rays to achieve mapping of the local material morphology, crystal structure, chemical composition, dynamical processes such as degradation occurring during battery operation and intercalation/deintercalation dynamics.[67,68,69] We believe that these techniques may provide solutions to our problems, however they are not offered in SA and are beyond the scope of an average MSc qualification which takes one and a half years to complete, luckily these experiments will be performed at Argonne National Laboratory in Chicago, in collaboration with University of Witwatersrand funded by the department of Science and Innovation as part of our future work.

Another important facet not to ignore is the zinc metal foil anode dendritic formation as well as stripping/platting, leading to rapid capacity decay which has been highlighted in **Chapter 2.5.2**. We attempted to soak the zinc metal anode in the 4M $NaClO_2$ for four weeks, the electrolyte was recorded to be of pH ~4, the results revealed that zinc undergoes stripping/plating indicated by the black scratches on the surface (**Appendix A1**) confirming the above-mentioned problems, hence during charging and discharging we expect this to occur at a much faster rate. Various methods have been proposed to circumvent this issue, K. E. K. Sun *et al*. suggested synthesizing novel zinc electrode via electroplating with organic additives in the plating solution, organic additives suggested were thiourea (TU), sodium dodecyl sulfide (SDS) and polyethylene-glycol (PEG-800) after 1000 cycles they maintained an 80%, 79%, and 76% capacity retention while commercial zinc metal foil maintained 67.5% of the initial discharge capacity, also coating with carbon materials such as active carbon proposed by H. Tao concluded that not only does the cycle life improve from 36 to 210 compared to Zn metal foil it also increases the capacity to 150 $mAhg^{-1}$ from 114 $mAhg^{-1}$ obtained by the Zn metal foil while also using very high concentrated salts.[23,70,71] lastly by synthesizing zinc anodes via electroplating with inorganic

additives proposed by K. E. K. Sun *et al.* employing tin oxide, boric acid and indium sulfate maintaining 82%, 78% and 75% capacity retention after 1000 cycles while commercial zinc maintaining 67% of its capacity retention.[24] Initially, we wanted to investigate the electrochemical performance of both MPF and MPF-CeO_2 materials, Needless to say, we have discovered other possible obstacles along the way, there is a lot of work to be done to perfect and optimize our battery however these are all suggestions for possible future work.

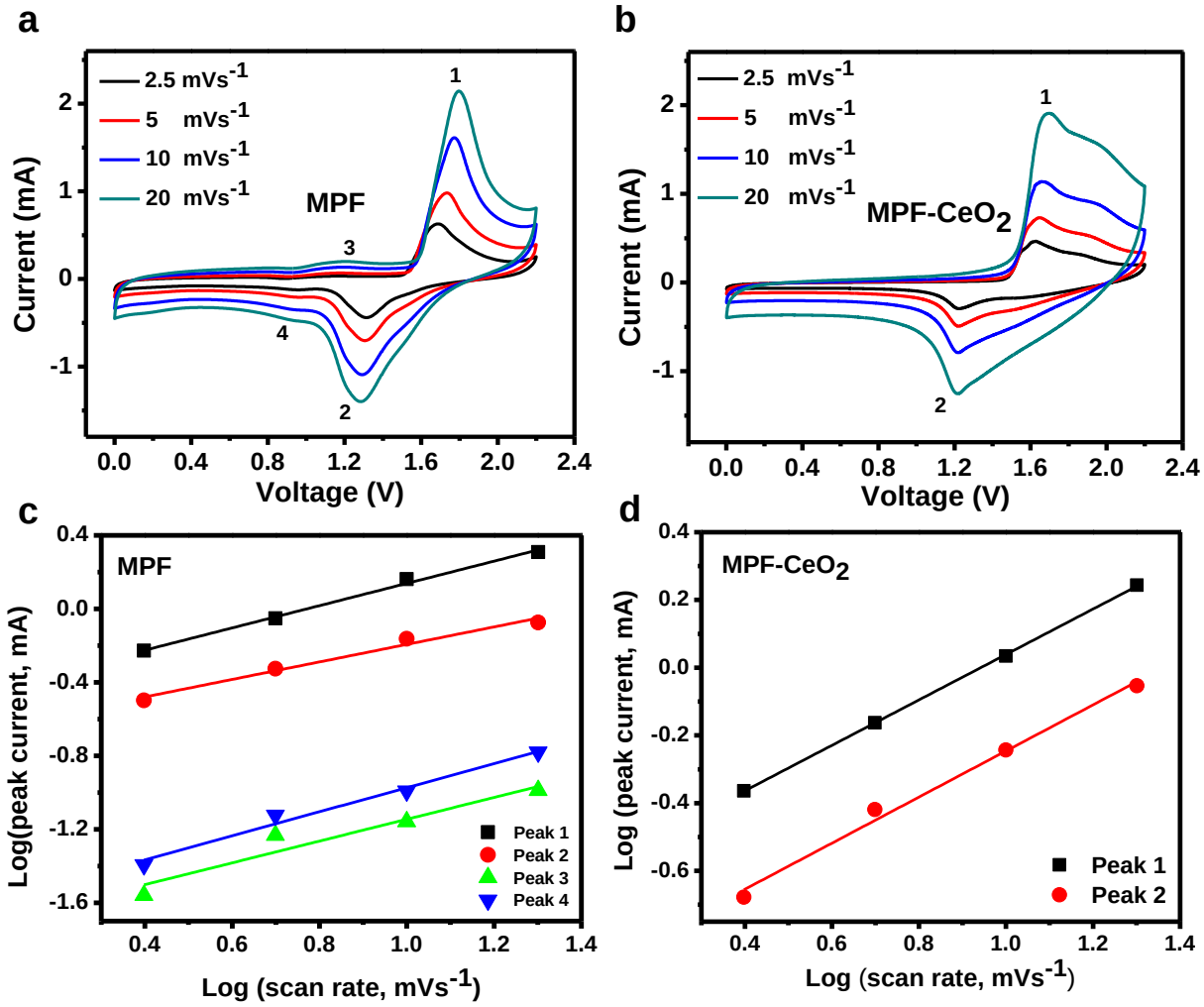


Fig. 4.13 | Electrochemical analysis of different kinetic responses. Active electrode material electrochemical CV curves for MPF (a) and MPF-CeO_2 (b) at sweep rates 2.5 to 20 mVs^{-1}, The dependence of parameter b on: MPF (c) and MPF-CeO_2 (d)

To further understand the high electrochemical performance of the MPF and MPF-CeO_2 as battery materials it significantly depends on their kinetics origin, which has been investigated by CV characterizations. **Fig. 4.13** displays the CV curves of the MPF (**a**) and MPF-CeO_2 (**b**) batteries at different sweep rates from 2.5 to 20 mVs^{-1} with a voltage window from 0.0-2.2 V. Their peak currents and scan rate have a relationship where the total current measured under a potential sweep rate can give a sum of the current related to the current required to charge the electrochemical double layer at the electrolyte interface, to start fast faradaic reactions on the electrode

surface known as a surface-controlled capacitive process (i_{cap}) and slow ionic diffusion-controlled process (i_{diff}) and expressed by the equations shown below:

$$i\,(v) = i_{cap} + i_{diff} = av^{b} \quad (1)$$

This can be written as:

$$\log i(v) = b\log v + \log a \quad (2)$$

Where both *a* and *b* are adjustable parameters

To understand the kinetic information about the electrochemical reactions, parameter *b* is determined from the slope of the linear plot log *i(v)* vs log *v*, *i* the current (A) and *v* the scan rate (Vs^{-1}). "The coefficient b varies in the range 0.5 – 1.0, the b value of 0.5 or less represents a slow ionic diffusion-controlled process that occur in the bulk, corresponding to a faradaic insertion/extraction reaction (battery-type process), while values ≈1.0 indicates a fast surface-controlled capacitive process, corresponding to redox reactions and charge/discharging the EDLCs (pseudocapacitive process) and the range between 0.5 – 1.0 indicates a transition area between battery-type and pseudocapacitive materials" as specified by Duun et *l.*[72,73,74,75,76] The analysis was taken at low scan rates from 2.5 to 20 mVs^{-2} as Dunn *et al*. did and as further elaborated by J Liu and Y Jiang, since the method does not fully hold at higher sweep rates were ohmic drop cannot be neglected.[76,77]

The calculated *b* values for MPF for peaks 1, 2, 3 and 4 are 0.60, 0.48, 0.59 and 0.65, the anodic peaks 1 and 3 can first be seen as a transition between battery-type and pseudocapacitive reaction/process and the cathodic peak 2 the *b* value decreases indicating slow ionic diffusion-controlled process whilst the cathodic peak 4 is seen as a transition between battery-type and pseudocapacitive reaction/process, meaning that the Na^{+} intercalation reaction dominated the current at peak 2. The calculated *b* values for MPF-CeO_2 for peak 1 and peak 2 are 0.67 and 0.68, the electrochemical reactions are simultaneously controlled by semi-infinite linear ionic diffusion and

partially by surface-controlled capacitive behavior, can be seen as a transition between battery-type and pseudocapacitive reactions.

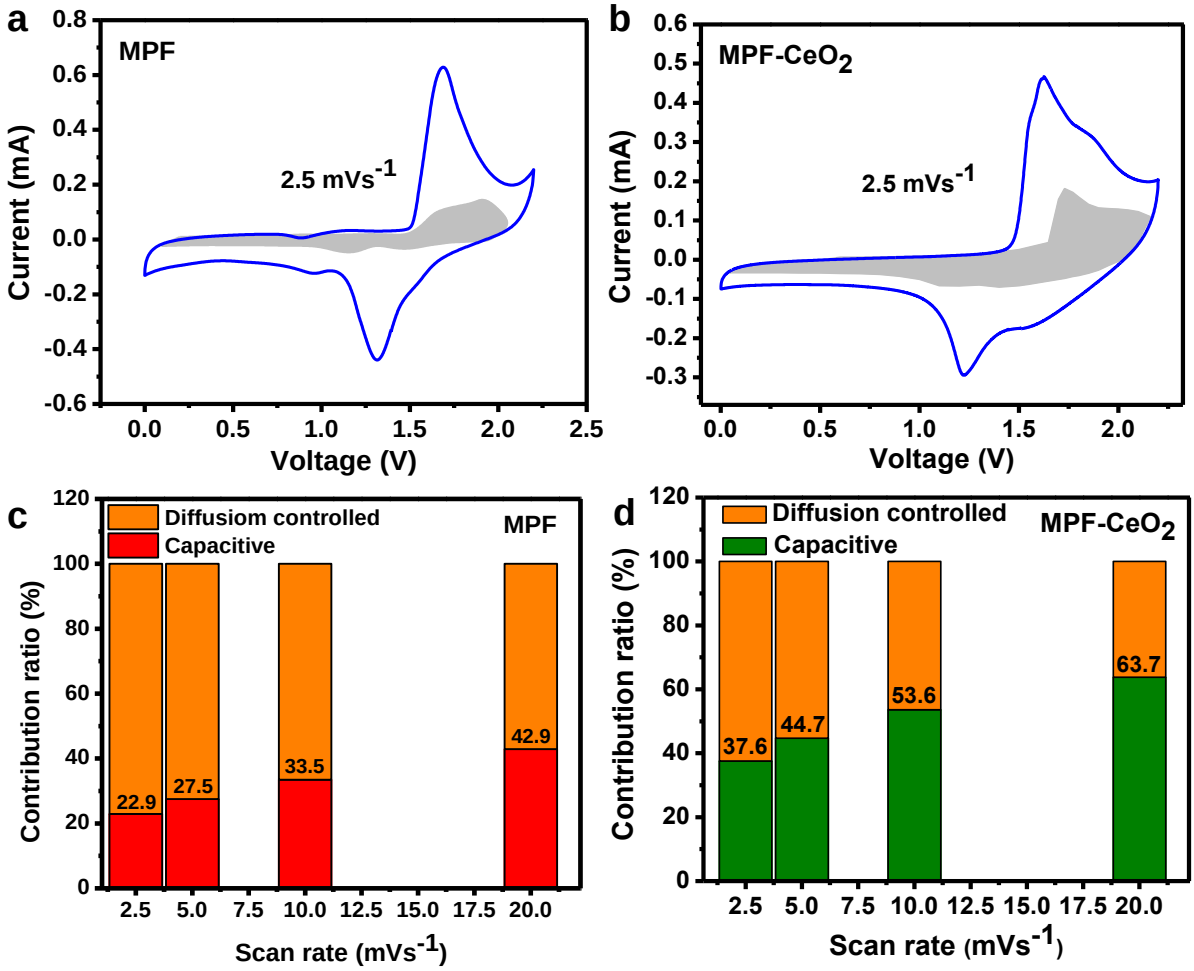


Fig. 4.14 | Differentiating capacitive effect from diffusion-controlled process using Dunn's Method. CV curves with the capacitive contribution fraction depicted by the shaded area at sweep rate 2.5 mVs^{-1} MPF (a) and MPF-CeO_2 (b), Capacitive contribution bar chart at sweep rates 2.5, 5, 10 and 20 mVs^{-1} MPF (c) and MPF-CeO_2 (d) respectively.

The pseudocapacitive contribution can be determined from different sweep rates calculated by the following equations known as the Dunn's method.

$$i\,(V) = i_{cap} + i_{diff} \quad (3)$$

$$i\,(V) = k_1 v + k_2 v^{1/2} \quad (4)$$

$$i/v^{1/2} = k_1 v^{1/2} + k_2 \quad (5)$$

where:

$i(V)$ = current at fixed potential

Capacitive current: $k_1 v$

Diffusion-controlled current: $k_2 v^{1/2}$

k_1 and k_2 are constants

From the plot of $i/v^{1/2}$ vs $v^{1/2}$ (5) gives k_1 and k_2 **appendix A3** (**a**, **b**) depicts the plot at fixed potentials for MPF at 0.3 V, 0.8 V and 1.86 V, for MPF-CeO_2 at 0.2 V, 0.6 V and 1.2 V with the capacitive contribution highlighted in gray at 2.5 mVs^{-1} **Fig. 4.14** (**a**, **b**). The calculated capacitive contribution measured at sweep rates 2.5 to 20 mVs^{-1} for MPF are 22.5%, 27.5%, 33.5% and 42.9% as for MPF-CeO_2 are 37.6%, 44.7%, 53.6%, 63.7%, as shown in **Fig. 4.14** (**c**, **d**), as the sweep rate increases the contribution ratios of the capacitive mechanism is evaluated to increase with sweep rate, with the diffusion contribution seen to remain dominant over lower sweep rates and at higher scan rates is seen as mild transitions between battery-type and pseudocapacitive reactions, however, ionic-diffusion seems to be dominant in MPF than capacitive-control which is in great agreement with the *b* value data obtained, thus indicating that MPF is kinetically dominated by the diffusion-controlled process at the potential 0-2.2 V. On the other hand, MPF-CeO_2 is controlled by both ionic-diffusion and capacitive-control which is also in agreement with the *b* value data obtained, this phenomenon is the main reason why it has better performing results than MPF.

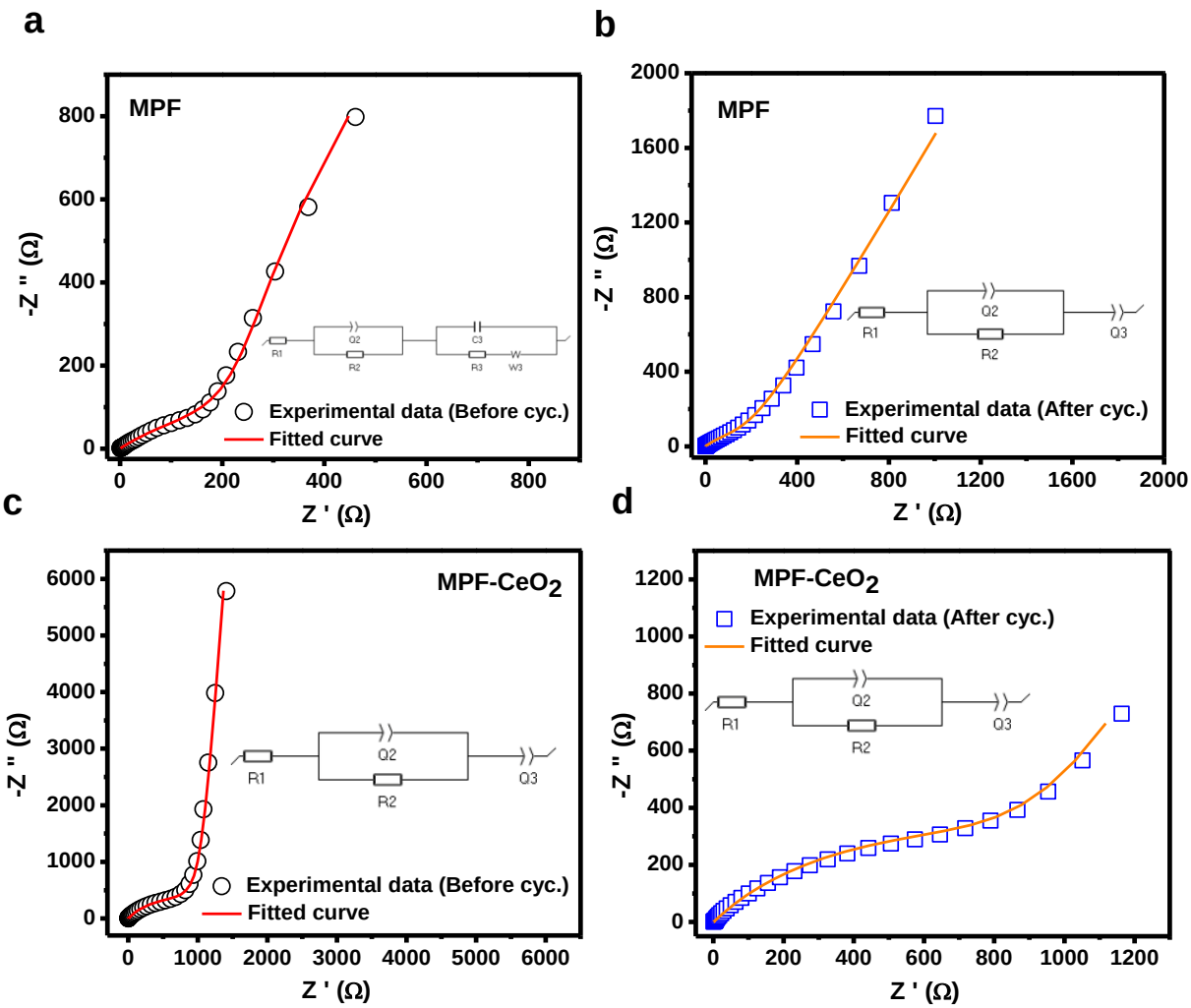


Fig. 4.15 | Electrochemical impedance spectroscopy (EIS). MPF before cycling stability (**a**) and after cycling (**b**), MPF-CeO_2 before cycling stability (**c**) and after cycling (**d**)

Table 4. 6 : Electrochemical impedance spectroscopy

	MPF-before cycling	MPF-after cycling	MPF-CeO_2-before cycling	MPF-CeO_2-after cycling
$R1_S$ (Ω)	7.589×10^{-15}	0.6083×10^{-15}	96.62×10^{-12}	0.6534
$R2_{ct}$ (Ω)	378.3	225.2	1094	0.8406×10^{-3}
$R3_{ct}$ (Ω)	3866			
$Q2_{cpe}$ (Fs^{-1})	2.496×10^{-3}	1.644×10^{-3}	0.3108×10^{-3}	1004
$Q3_{cpe}$ (Fs^{-1})		3.926×10^{-3}	251×10^{-3}	0.01293
C3 (F)	0.01365			
W3 ($\Omega s^{-0.5}$)	29.25×10^{-90}			

The electrochemical impedance spectra were recorded using an AC at 10 mV and the impedance spectra are fitted using an equivalent circuit, **Fig. 4.15** displays the results of both materials before and after cycling using a T-cell battery. **Table 4.7** summarizes the obtained data from fitting the equivalent circuit, $R1_S$ represents the solution resistance, $R2_{ct}$ and $R3_{ct}$ represent the charge-transfer resistance, $Q2_{cpe}$ and $Q3_{cpe}$ represent the constant phase element (CPE) related to double-layer capacitance, C3 represents capacitance and W3 the Warburg diffusion.

A comparison of MPF after and before cycling reveals that the material undergoes structural changes since the fitted equivalent circuit for before and after cycling are two different circuits which are both connected in series. The circuit before cycling at higher frequency region has $R1_S$, $R2_{ct}$, $Q2_{cpe}$ as its elements and at lower frequency region has C3, $R3_{ct,}$ and W3, which is the Warburg diffusion represented by the 45° line, this circuit correlates well with the results obtained for the capacitive contribution calculations which stated that the ionic-diffusion reactions are more dominant than capacitive-control. The circuit after cycling has $R1_S$, $R2_{ct}$, $Q2_{cpe,}$ and $Q3_{cpe}$, the straight line is due to the CPE, the second circuit after cycling confirms the fact that MPF losses its electrochemical performance since both before and after cycling need two different circuits, thus revealing to us the extreme dissolution of Mn^{2+} and zinc metal anode stripping/plating. MPF-CeO_2 uses the same circuit before and after cycling, with the elements $R1_S$, $R2_{ct}$, $Q2_{cpe}$ and $Q3_{cpe}$ confirming both ionic-diffusion and capacitive-control, indicating the significant difference in the addition of the CeO_2 coating to stabilizes the structure, however for only up to 400 cycles as discussed in **Fig. 4.15** (**e**) indicating that CeO_2 slightly suppress Mn dissolution. The only large significant difference is the $Q3_{cpe}$, before cycling the value is 251 x 10^{-3} Fs^{-1} (represented by the almost ~80°, sharp line and after cycling the $Q3_{cpe}$ value increases to 0.01293 Fs^{-1}, further elaborating the decrease in the electrochemical performance of the material which correlates with the results obtained after cycling stability leading to the dissolution of Mn^{2+}.

4.2.3 Application

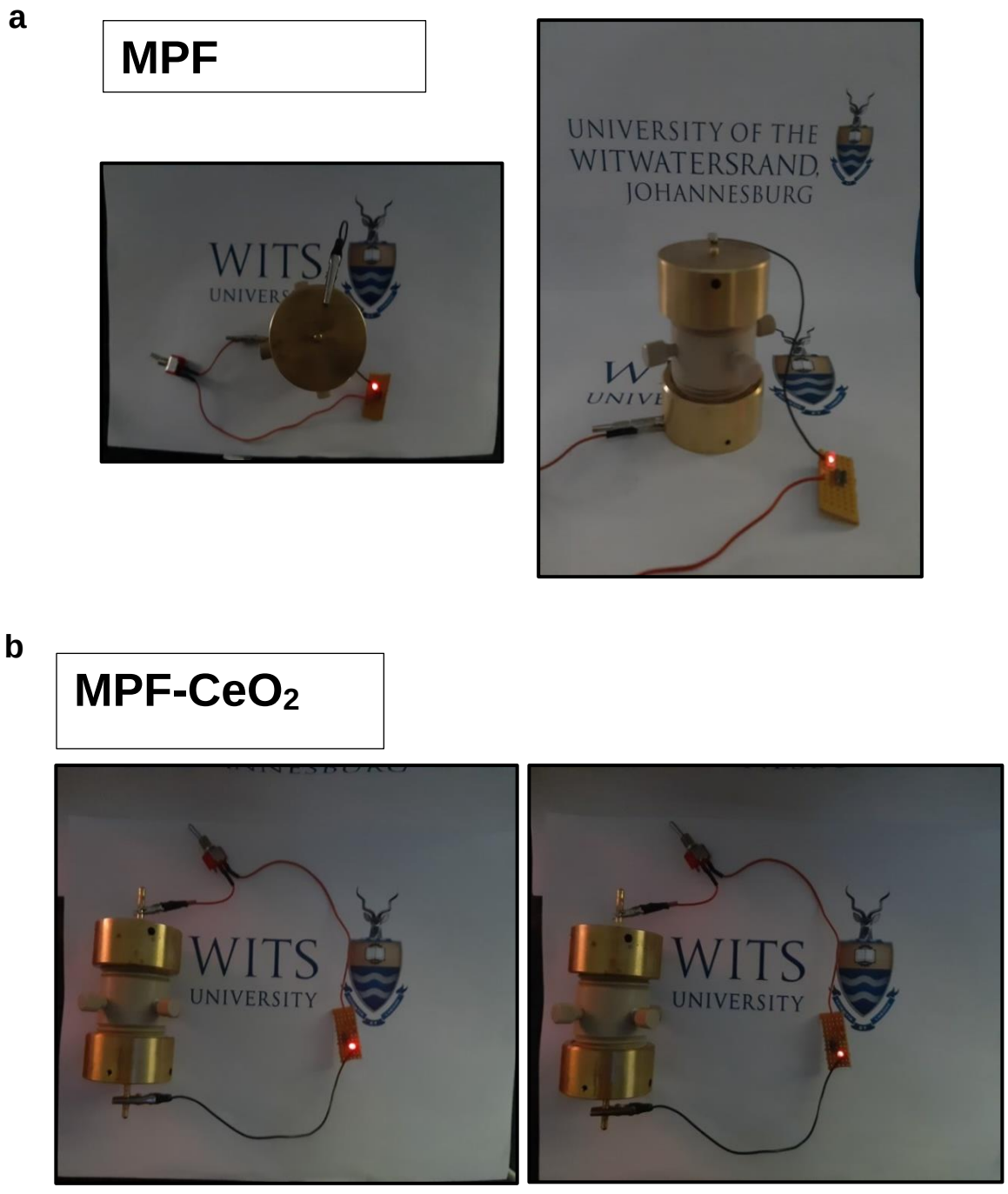


Fig. 4.16 | Application tests. MPF lasted for 02 mins:20.81 secs (**a**), MPF-CeO_2 lasted for 11 mins:07.80 secs (**b**)

The last experiment that was performed as to test the battery as an energy storage device as proof of application that the materials can be used for commercial purposes as displayed in **Fig. 4.16** (**a**, **b**). The test was to determine which battery material will have the longest discharge time, meaning a larger energy density, this test is to solidify our electrochemical behavior and performance data as we had assumed that MPF-CeO_2 shall have high energy storage characteristics over MPF. The results are as follows, MPF had a discharge time of 02 mins:20.81 secs and MPF-CeO_2 had a discharge time of 11 mins:07.80 secs, indeed our predictions were true, therefore indicating that our electrochemical data is correct and precise with MPF-CeO_2 being the materials with the better electrochemical performance and is the most suitable for commercial immobile energy storage applications and MPF behaving more like a capacitor supplying short burst of energy.

4.3 Conclusion

In summary, the attempt to synthesize the mineral triplite (Mn_2PO_4F) as MPF via microwave synthesis and the 2% coating of CeO_2 was accomplished. The XRD, Raman and IR results revealed to us that Mn_2PO_4F was obtained with XPS displaying the elements along with their respective bonding involved, although minor impurities were obtained from these results which are suspected to belong to the starting materials. The main aim was to determine the electrochemical performance of the two material, from that get the best performing material. By taking the results obtained from the T-type cell MPF at 0.1 C gave 2.11 $mAhg^{-1}$ while MPF-CeO_2 at 0.1 C had 101.61 $mAhg^{-1}$, the stability analysis revealed that MPF cycled at 0.1 C only maintained 60% of its initial capacity until 55 cycles, thereafter crashing with $\pm$ 99% CE and cycled at 5C MPF-CeO_2 from the 1st to the 73rd cycle increased its initial capacity to from 100% to 109%, the reason is due to the formation of the SEI, the periodic activation of the active material species and suppression of the oxygen evolution by CeO_2 coating, thereafter the capacity decreased to 90% lasting only 400 cycles with $\pm$ 99% CE, which suggests that the coating by CeO_2 enhances the electrochemical behavior as well as the performance of MPF. The reason for the crash instability is reported in the literature is caused by Mn^{2+} dissolution and zinc metal foil anode dendritic formation as well as stripping or plating. The analysis of different kinetic responses reveal that MPF has the following b values for peaks 1, 2, 3 and 4 are 0.60, 0.48, 0.59 and 0.65, whilst MPF-CeO_2 has b vales for peak 1 and 2 at 0.67 and 0.68. By further differentiating capacitive effects from the diffusion-controlled process using Dunn's Method, the capacitive contributions were measured at sweep rates 2.5 to 20 mVs^{-1}. MPF had 22.5%, 27.5%, 33.5%, and 42.9% and MPF-CeO_2 had 37.6%, 44.7%, 53.6%, and 63.7%, these results reveal that MPF may be seen to represent transitions between battery-type and pseudocapacitive reactions or process which are mainly kinetically dominated by diffusion-controlled process making it a good candidate for capacitors and battery materials. MPF-CeO_2 electrochemical reactions are simultaneously controlled by semi-infinite linear ionic diffusion and partially by surface-controlled capacitive behavior and results reveal that MPF-CeO_2 is the best suited material for energy storage with all its dominant electrochemical

behaviour and performance over MPF, thus 2%-CeO_2 coating is crucial to stabilizing the MPF structure.

CHAPTER FIVE

Comparison of MPF-CeO_2-CB And MPF-CeO_2-C

5.1 Methodology

Materials. Sodium Fluoride, ammonium dihydrogen phosphate, manganese nitrate tetrahydrate, Cerium nitrate hexahydrate, potassium hydroxide, carbon black, polyvinylidene fluoride, sodium perchlorate and 1-methyl-2pyrrolodone (MPF) were purchased from Sigma-Aldrich.

5.1.1 Synthesis of MPF-CeO_2-CB

Preparation of MPF-CeO_2-CB, obtained 371 mg of pristine – MPF (preparation as shown in **Chapter 4.1.1**) and 55.65 mg of carbon black (15%) were added to a solution containing 18.72 mg of $Ce(NO_3)_3.6H_2O$ (2%) in 50 ml deionized water to form a black solution. The mixture was kept under stirring for 30 mins and then sonicated

for 30 mins at 25 ℃. The solution was adjusted to pH 12 with 2M KOH and vigorously stirred for 2 h. with no color change. The product was centrifuged with H_2O until neutral pH, then dried at 60 ℃ for 12 h. and subsequently heated under air tube furnace at 250 ℃ for 2 h.[61], to obtain a black product in color.

5.1.2 Synthesis of MPF-CeO_2-C

Preparation of MPF-CeO_2-C, dissolved 503.86 mg of NaF (3 mmol), 920.24 mg of $NH_4H_2PO_4$ (2 mmol), 882.58 mg of citric acid in 10 ml (separate beakers) deionized water and left to stir for 20 minutes/until fully dissolved. Then poured the solution containing $NH_4H_2PO_4$ into the beaker that contains NaF to make solution A and a clear solution was formed. For the preparation of solution B, 2.00 g of $Mn(NO_3)_2.4H_2O$ (2 mmol) was dissolved in 20 ml deionized water and left to stir for 10 minutes/until fully dissolved. Solution A was gradually added to solution B upon mixing a gel-like whitish solution that appeared and then left to stir for 6 h and subsequently added the solution containing citric acid to make up solution C, with no color change being observed. Solution C was left to stir for another 6 h at 1000 rpm at room temperature.[54,55,56,57] Microwave hydrothermal synthesis was carried out at 600 W, 180 ℃, 50 bar, while stirring at fan speed 2 and firstly ramped up for 10 minutes and then ran for 45 minutes.[58,59,60] The resulting product was coffee to carob brown in color, which was then centrifuged x5 with water then x3 with ethanol and left to dry at 60 ℃ for 12 h. [54,55,56]

Thereafter **two-step-solid state synthesis** was performed, preheated sample at 350 ℃ for 4 h., then heated at 800 ℃ for 8 h. under Ar at a flow rate of 0.072 L/min under tube furnace. [54,55,56,57] The final product was carob brown in color. Lastly, **2% coating with CeO_2** 524.90 mg of MPF-C (Mn_2POF-C) was added to a solution containing 26.49 mg $Ce(NO_3)_3.6H_2O$ in 50 ml deionized water and a carob brown solution was formed. The mixture was kept under stirring for 30 mins and then sonicated for 30 mins at 25 ℃. The solution was adjusted to pH 12 with 2M KOH and vigorously stirred for 2 h, forming a pure brown solution. The product was centrifuged with H_2O until neutral pH, then dried at 60 ℃ for 12 h. and subsequently heated under air tube furnace at 250 ℃ for 2 h.[61], obtaining a brown product.

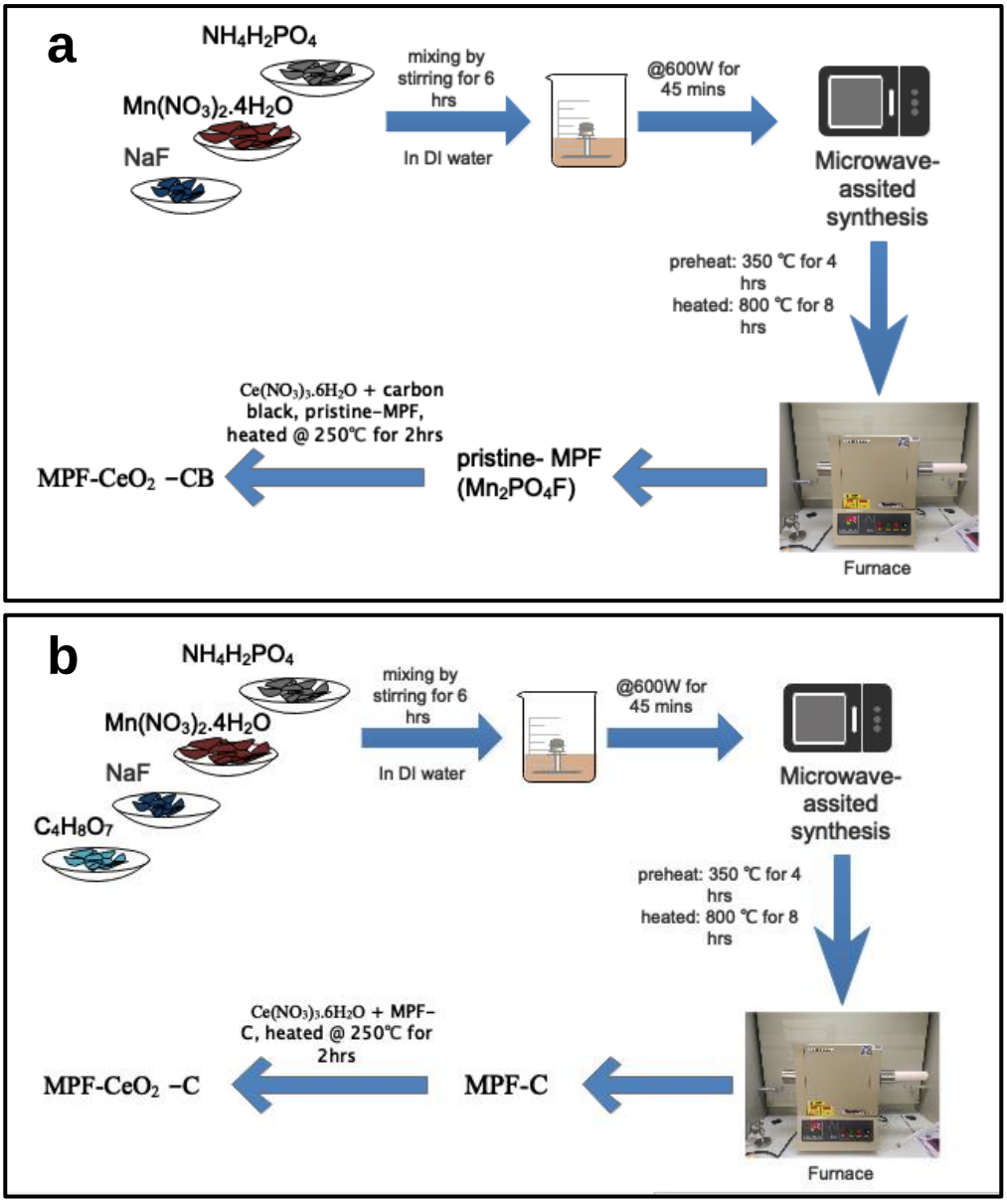


Fig. 5. 1 | Schematic representation of the preparation of MPF-CeO_2-CB (a, 5.1.1) and MPF-CeO_2-C (b, 5.1.2)

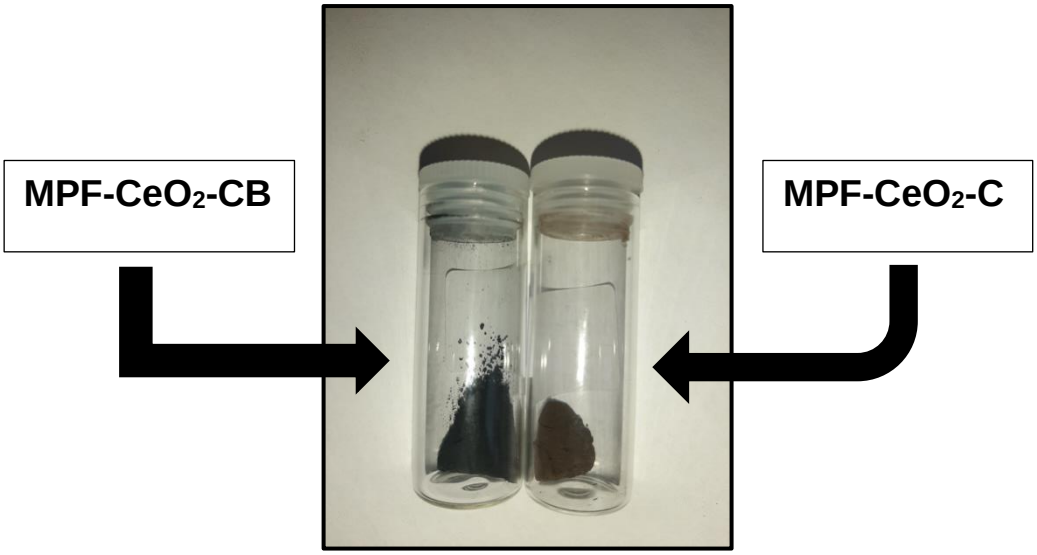


Fig. 5.2 | Image showing finished products with their respective colours

5.1.3 Characterization

Similar to **Chapter 4.1.3**

5.1.4 Electrode Processing

The positive electrode was prepared by mixing MPF-CeO_2-CB or MPF-CeO_2-C, carbon black and PVDF (polyvinylidene fluoride) in a weight ratio of 80:10:10 by NMP, then casting the slurry on carbon paper. After drying at 80℃ for 12 hrs. MPF-CeO_2-CB coin cell positive electrode had ~3.8 mg while MPF-CeO_2-C had ~1.9 to 2.6 mg of active mass loading and as for the T-type cell, MPF-CeO_2-CB had ~1.0 to 1.4 mg and MPF-CeO_2-C had ~1.0 to 1.3 mg of active mass loading.

5.1.5 Coin and T-type Cell Fabrication

Coin-cell Fabrication. As shown in **Chapter 4.1.4**

T-type cell Fabrication. As shown in **Chapter 4.1.4**

5.2 Results and Discussion

5.2.1 Materials Characterization

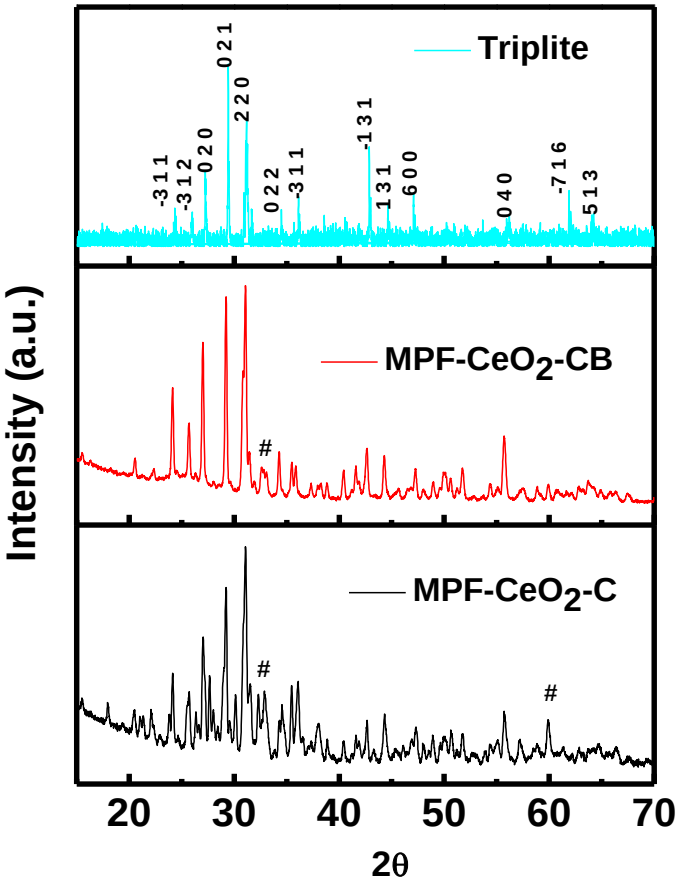


Fig. 5. 3| PXRD Pattern comparison of Triplite, MPF-CeO_2-CB, MPF-CeO_2-C

The above XRD patterns **Fig. 5.3** were determined using Cu Kα_1 = 1.54060 radiation which confirms that the phase pure Mn_2PO_4F was successfully synthesized using the microwave syntheses, as all the Bragg peaks can be fully indexed to a crystal structure of monoclinic symmetry corresponding to the space group C2/c (15), which is based on that of the triplite that was first structurally explored by Rea and Kostiner in 1972 of which they discovered triplite to have lattice parameters *a* = 13.410, *b* = 6.50960, *c* = 10.0940 Å, and β = 199.990°. it is clear from the comparison X-Ray diffraction that MPF-CeO_2-CB and MPF-CeO_2-C have the same peaks as mineral triplite, however the peaks at 24.30° [-3 1 1], 31.33° [2 2 0], 61.83° [-7 1 6], 42.66° [-1 3 1], 61.83° [-7 1

6] and 64.00° [5 1 3] they a similar in explanation as of those obtained in **chapter 4.2.1** (**Fig. 4.3**),. The differences observed are at 32.81° for both MPF-CeO_2-CB and MPF-CeO_2-C, however, MPF-CeO_2-C has extra peaks at 27.65°, 29.98° and 59.98° indexed by a hashtag (#), these maybe are also due to the in-situ addition of carbon during reaction mechanism. The next step is to determine if the in-situ or ex-situ addition of carbon will have an impact on the electrochemical performance. However, this does indicate that both synthesis procedures are different and in-situ addition of carbon via citric acid will yield extra peaks with little to no shift in the peak positions.

Appendix A4 displays the PXRD Rietveld refined peaks of both MPF-CeO_2-CB (R_{exp}: 0.80, R_{exp}: 1.96, R_{exp}: 1.34) and MPF-CeO_2-C (R_{exp}: 0.79, R_{exp}: 3.92, R_{exp}: 2.60), from the obtained refinement the lattice parameters which are summarized in **Table 5.1** for MPF-CeO_2-CB are a = 13.42, b = 6.514, c = 10.11, and β = 119.99 with d spacing of 2.874 nm and a unit cell volume of 765.539 while MPF-CeO_2-C lattice parameters are a = 13.40, b = 6.513, c = 10.08, and β = 119.99 with d spacing of 2.872 nm and a unit cell volume of 762.724. The lattice strain (*s*) **Table 5.1** was also analyzed to give an understanding of how each carbon in-situ and ex-situ coating affects the sample lattice parameters. The lattice strain of MPF-CeO_2-CB was significantly small and as for MPF-CeO_2-C the lattice strains were just higher than MPF-CeO_2-CB, with this set of data it is inconclusive to determine whether the carbon coating had an actual effect on the structure.

Table 5. 1 : Parameters obtained from XRD patterns, interplanar distance, lattice parameters and strain

Sample	d (2 0 2)	a	s_a (%)	b	s_b (%)	c	s_c (%)
MPF-CeO_2-CB	2.873	13.42	0.0049	6.514	0.024	10.11	0.031
MPF-CeO_2-C	2.870	13.40	0.129	6.513	0.0171	10.09	0.195

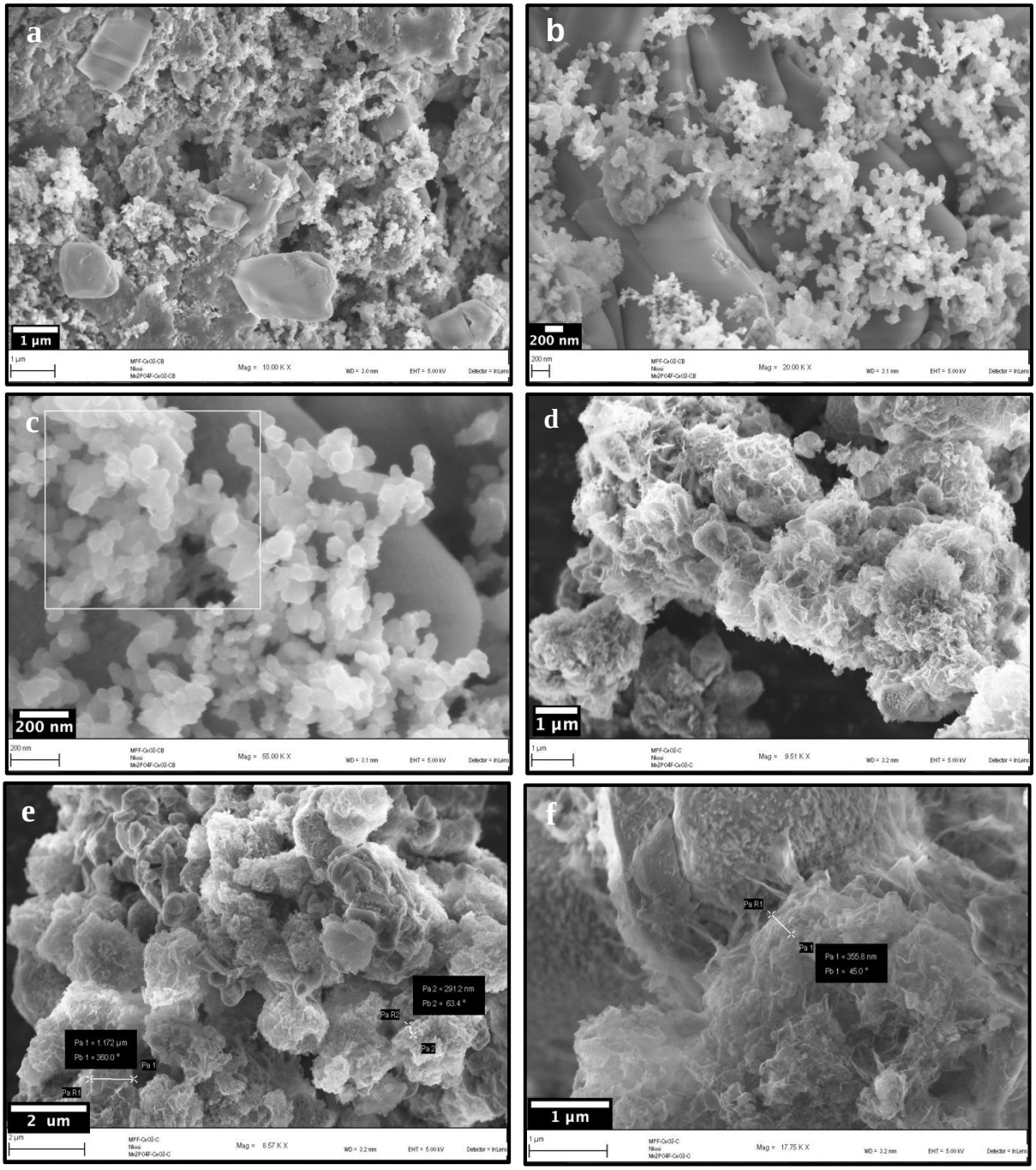
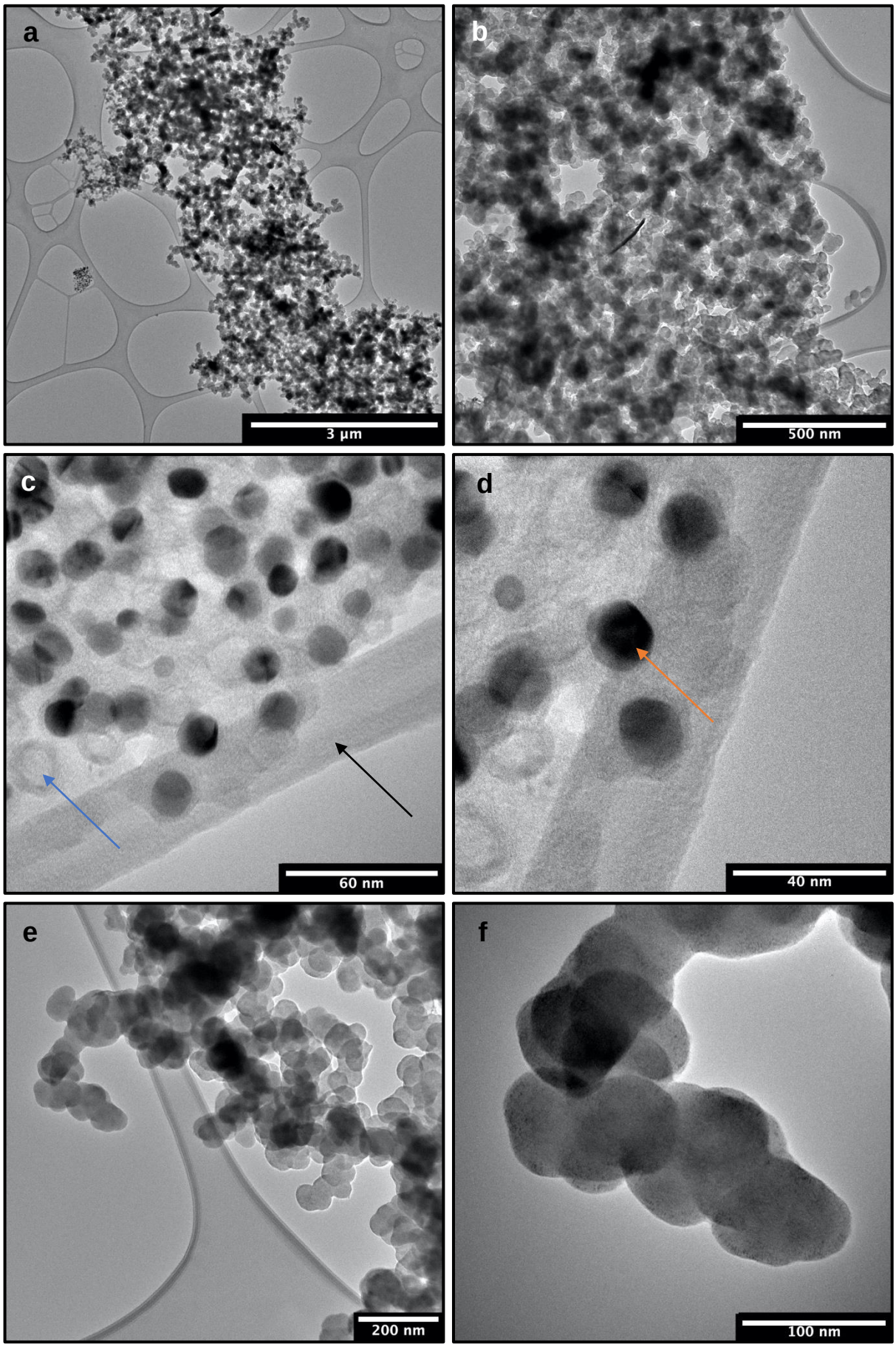


Fig. 5.4 | SEM micrographs of MPF-CeO_2-CB (**a-c**), MPF-CeO_2-C (**d-f**)


a
3 µm
b
500 nm
c
60 nm
d
40 nm
e
200 nm
f
100 nm

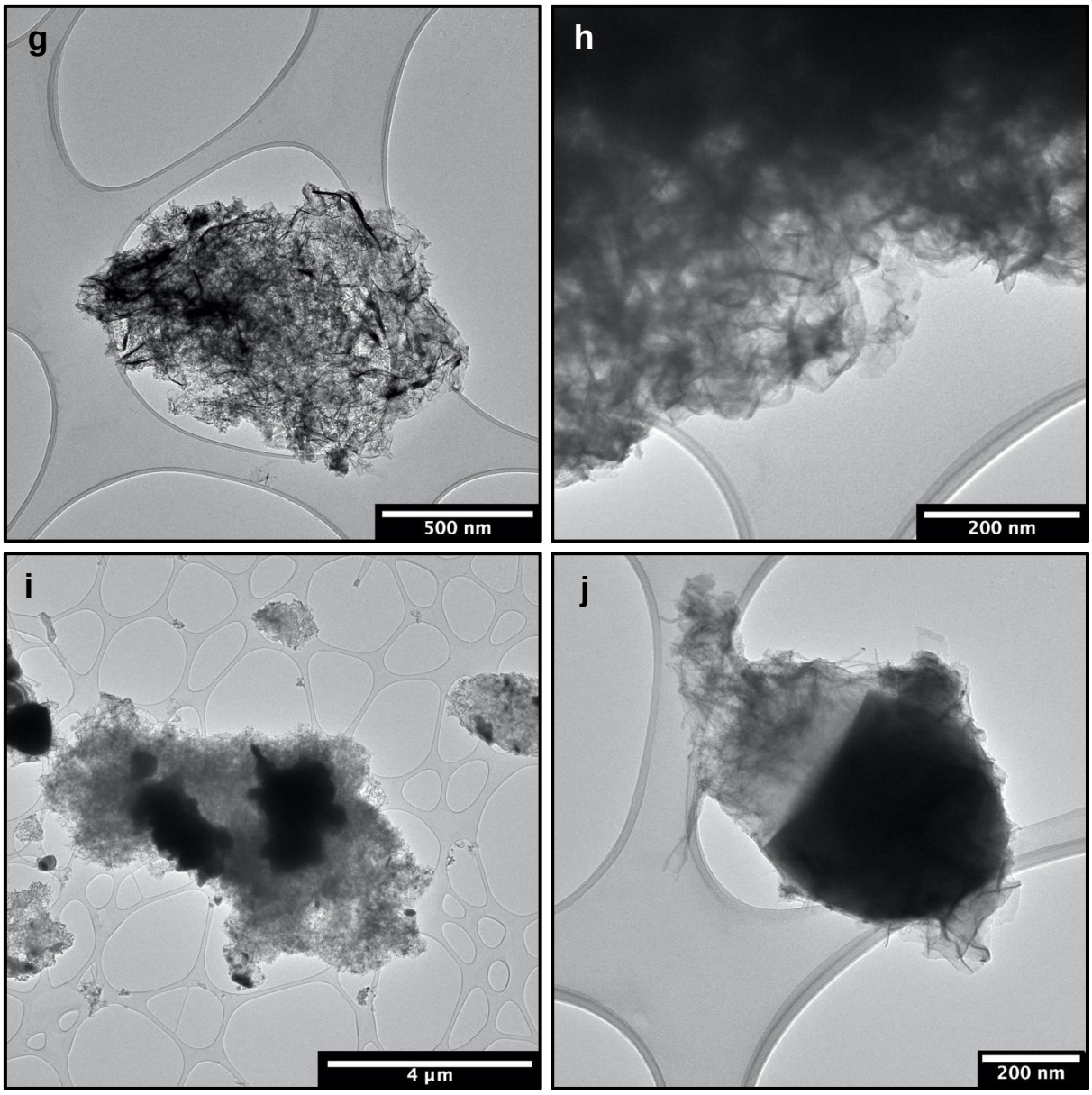


Fig. 5.5 | TEM micrographs of MPF-CeO_2-CB (**a-f**), MPF-CeO_2-C (**g-j**)

Fig. 5.4 are the SEM micrographs of MPF-CeO_2-CB and MPF-CeO_2-C, were **Fig. 5.4** (**a-c**) represents MPF-CeO_2-CB appearing as a mixture of nanoparticles and agglomerated particles with different morphologies. From these three images, it is very hard to deduce the carbon coating from the CeO_2 coating, however, it is very clear that there is no spider-web like morphology resting over the particles as seen in **chapter 4** (**Fig. 4.6** (**d-f**)) of MPF-CeO_2, thus we hope that TEM can help aid solidify our speculations. **Fig. 5.4** (**d-f**) are of MPF-CeO_2-C observed as agglomerated particles with CeO_2 coating appearing as a spider-web like morphology covering the agglomerated particles in which the coating is represented as white clumps on the

grey substrate, this does indicate that the 2% coating by CeO_2 was achieved, however, the coating by carbon is not clear since it was included at the beginning of the synthesis. It was difficult to determine the particle size distribution for both materials.

The TEM micrographs were also obtained as shown in **Fig. 5.5** (**a-j**) for both samples. **Fig. 5.5** (**a-c**) represent TEM images for MPF-CeO_2-CB, in the image (**a**) they appear as one big particle and in the image (**b**) there are darker areas which are surrounded by grey soot, this might indicate the coating by CeO_2 since it was not clearly defined in SEM, in the image (**c**) ignore the black arrow it resembles the carbon grid, the blue arrow marks an area where a particle might have occupied the position but somewhat got displaced, the real reasoning for this occurrence is unknown, however, we assume that the coating of carbon black might have had a negative impact on the nanoparticles which will be interrogated later if there is any effect on the electrochemical performance, image (**d**) the orange arrow demarks the MPF particle with the surroundings representing the coated area. Image (**e, f**) are interesting since they are agglomerated particles sitting on top of each other with no presence of any spider-web like coating by CeO_2, this could be detrimental when investigating the electrochemical behaviors and performance if not all the particles are coated, therefore coating by CeO_2 was not fully achieved in this process, we believe that the presence of carbon black might have caused this effect because when we did the coating for MPF-CeO_2 in **chapter 4** the particles were covered by the spider-web-like morphology, but in this case, it is not true, only a partial amount is coated.

The TEM micrographs of MPF-CeO_2-C is shown in **Fig. 5.5** (**g-j**), image (**g**) shows an area view of the sample with dark and a grey cloud surrounding the dark spots, a closer look was taken on the image (**h**) which confirms the spider-web-like represented by the grey cloud observed in SEM as the coating of CeO_2. Image (**i**) depicts particles as dark shaded spots representing the MPF-C material surrounding by a coating which belongs to the CeO_2 coating and image (**j**) shows a much clearer closer look at the particle MPF-C with the CeO_2 coating, it is worth noting that the coating by carbon from citric acid is not visible, however many have reported such as John B. Goodenough *et al.*, S. Zhong *et al.* and B. Zhong *et al.*, that the addition of citric acid not only acts as a chelating agent but can also introduce carbon as a shell coating around particles to improve the materials conductivity[11,56,78], however, to observe such

a phenomenon we would require a technique such as HRTEM in which we plan to do in our future work.

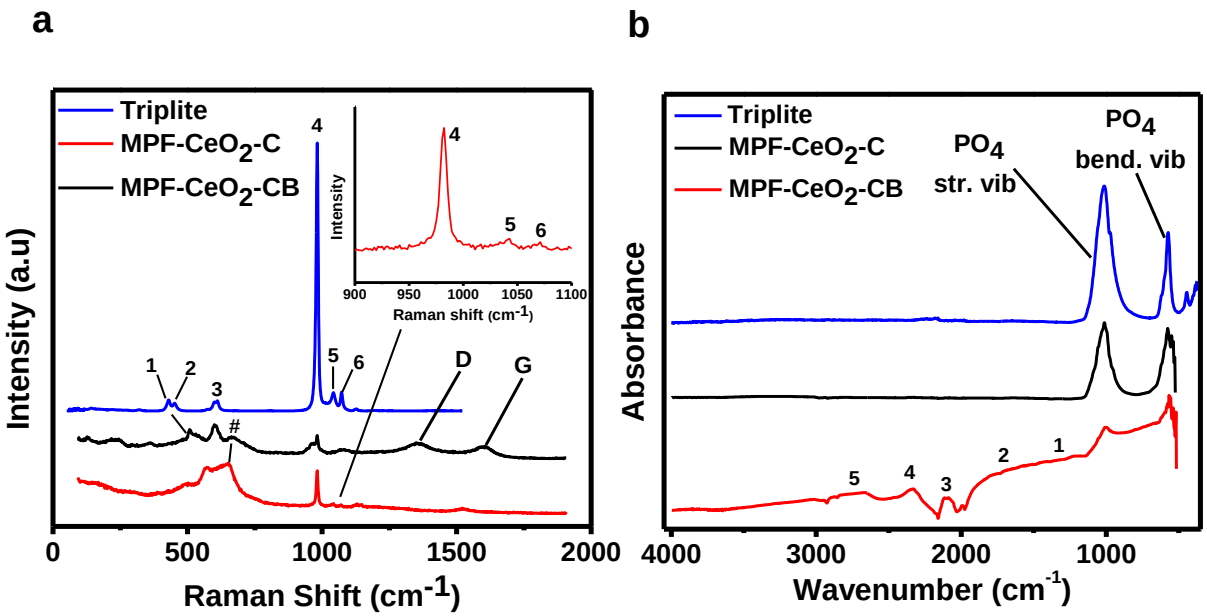


Fig. 5.6 | Raman spectrum of MPF-CeO_2-CB and MPF-CeO_2-C (**a**), **Infrared spectrum** of MPFCeO_2-CB and MPF-CeO_2-C (**b**)

The Raman spectra **Fig. 5.6** (**a**, **b**), was obtained using the 514.5 nm (green line) with the Raman bands summarized in **Table 5.2**. The points were collected at different points on the sample with a few significant differences. Herewith in contains a comparison of the main Triplite sample, MPF-CeO_2-CB and MPF-CeO_2-C. For the samples the spectrum is dominated by the phosphate group with the main Raman band which is very sharp and strong is centered at 980.5 cm^{-1} (4) for Triplite, for MPF-CeO_2-CB at 980 cm^{-1} (4) with medium intensity and for MPF-CeO_2-C at 984 cm^{-1} (4) with a strong intensity, this band is attributed to the *v1* vibration symmetric stretching of the phosphate unit.

For Triplite the medium band at 1036 cm^{-1} (5) is also located in MPF-CeO_2-C at 1043 cm^{-1} (5) with very-weak intensity, this particular band corresponds to *v2* asymmetric vibration stretching of the phosphate unit. The weak band occurring at 1072 cm^{-1} (6) for Triplite is also found in MPF-CeO_2-C at 1071 cm^{-1} with very-weak intensity, this band is attributed to *v3* asymmetric stretching of the phosphate unit. As for MPF-CeO_2-

CB the *v2* and *v3* asymmetric stretching of the Phosphate unit are coupled together occurring at 1080 cm^{-1} (5, 6) with a weak intensity, this is due to the carbon addition and its ability to shift the positions of the atoms in the crystal structure and interaction with the metal oxide, thus the addition of carbon in-situ (citric acid) or ex-situ (carbon black) will give similar results in terms of Raman peak shifting.

For all samples the bands within the range 429-610 cm^{-1} can be grouped into two regions corresponding two different modes of the phosphate group, firstly the range 429 (1) and 458 cm^{-1} (2) correspond to *v2* phosphate deformation, for MPF-CeO_2-CB these are coupled together occurring at 513 (1, 2) cm^{-1} with medium intensity due to the addition of carbon as mention previously, however, the effects are more prominent at this region. As for MPF-CeO_2-C these peaks positioned 495 (1) and 573.25 (2) cm^{-1} with medium intensity these occur further to the right of the Raman shift due to the same reason mentioned above, then secondly at 600 and 610 cm^{-1} correspond to *v4* phosphate deformation in which MPF-CeO_2-CB has these peaks positioned at 600 cm^{-1} (3) and MPF-CeO_2-C positioned at 603.49 cm^{-1} (3).

Lastly MPF-CeO_2-CB has D and G bands at 1350.89 cm^{-1} and 1605.31 cm^{-1} respectively, the measures I_D/I_G deconvoluted curve ratio is 1.18 indicating that there are more defects in the sample and more sp^3 bonds are being broken to form sp^2 bonds, whilst for MPF-CeO_2-C there is no D-band, however, there is a small G band positioned at 1523.85 cm^{-1}. It is known that having more defects increases surface area and increases conductivity, unfortunately for MPF-CeO_2-C we were unable to determine the I_D/I_G ratio due to the lack of the D-band. Thus, comparison analysis of the Raman bands shows us that MPF-CeO_2-CB and MPF-CeO_2-C resemble that of Triplite, with slit peak shifting due to the presences of carbon in the structure

An **Infrared spectrum** was analyzed for both samples **Fig. 5.7 (b**) and both were found to represent the Triplite sample reported in literature[35] which are characterized by absorption bands located between the regions 400 to 650 cm^{-1} which correspond to PO_4 bond vibration as well as lattice vibrations and stretching vibrational modes of the PO_4 tetrahedra within the region 1200 to 900 cm^{-1}.[35] However in the case of MPF-CeO_2-CB it has extra peaks which have been identified to belong to the groups with

the following adsorption; (1) C-C stretching at 1200 to 1500 cm^{-1}, (2) C-O stretching at 1500 to 2000 cm^{-1}, (3) C=O stretching at 2098 cm^{-1}, (4) O-C=O stretching at 2352 cm^{-1} and (5) 2656 to 3500 cm^{-1} this region is usually dominated by O-H and C-H stretching, however, we have to check with results from XPS if such bonding exist, the rest are due to the presents of carbon black which was added in ex-situ around the material.

Table 5. 2 : Tabulated Raman data

Sample	Raman Shift (cm^{-1})	Intensity	Vibration	Ref
Triplite	429 (1) 450 (2) 610 (3) 980.5 (4) 1036 (5) 1072 (6)	S W M Vs M W	*v2* Phosphate (deform) *v2* Phosphate (deform) *v4* Phosphate (deform) *v1* (symm str. Phosphate) *v2* (asymm str. Phosphate) *v3* (asymm str. Phosphate)	42
MPF-CeO_2-CB	513 (1,2) 600 (3) 980 (4) 1080 (5,6) 1350.89 (D) 1605.31 (G)	M M M W M M	*v2* Phosphate (deform) *v2* Phosphate (deform) *v1* (symm str. Phosphate) *v2 and v3* (asymm str. Phosphate) *D-mode sp^3 vibrations* *G-mode sp^2 vibrations*	
MPF-CeO_2-C	495 (1) 573.25 (2) 603.49 (3) 984 (4) 1043 (5) 1071 (6) 1523.85 (G)	M M M S Vw Vw Vw	*v2* Phosphate (deform) *v2* Phosphate (deform) *v2* Phosphate (deform) *v1* (symm str. Phosphate) *v2* (asymm str. Phosphate) *v3* (asymm str. Phosphate) *G-mode sp^2 vibrations*	

Table 5. 3 : Tabulated summary of BET data

Samples	Surface Area (m^2g^{-1})	Pore Volume (m^3g^{-1})	Pore Size nm
MPF CeO_2-CB	16.12	0.1518	34.29
MPF-CeO_2-C	13.59	0.1705	46.50

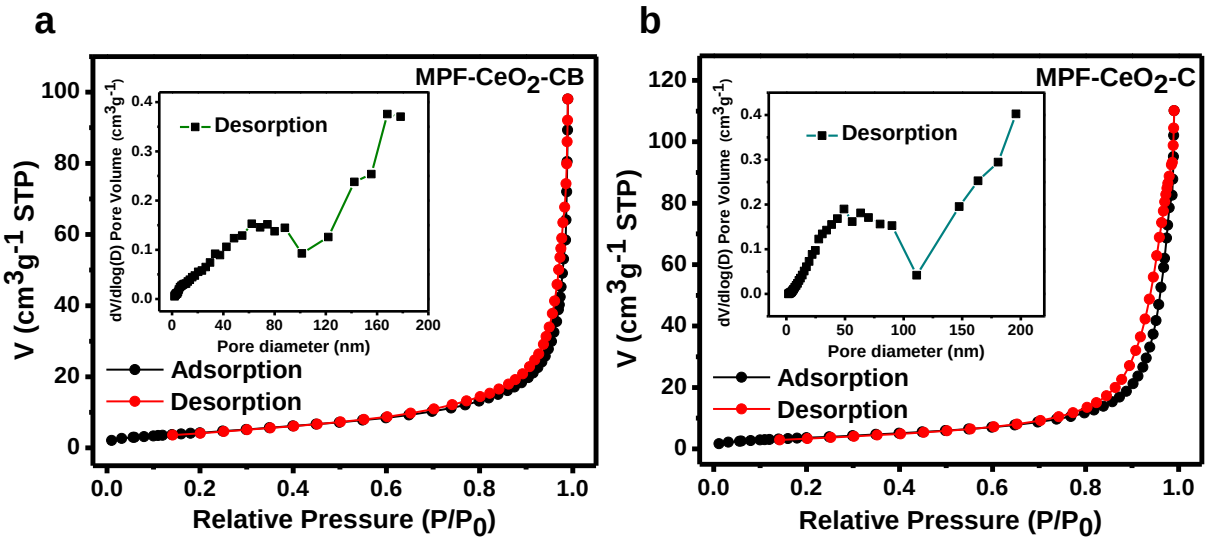


Fig. 5.7 | Brunauer-Emmett-Teller (BET) surface area analysis using N_2 adsorption-desorption studies, MPF-CeO_2-CB (**a**) and MPF-CeO_2C (**b**) BET isotherm plots

As we know, surface area (S.A), pore volume and pore size will all influence the electrochemical performance of battery material. **Table 5.3** sums up the BET analysis performed for both samples, these measurements were done to obtain information on the electrochemical active S.A, which is the area of the electrode that is accessible to the electrolyte for storage and charge transfer (double layer charging or pseudocapacitive), contributing to the capacitive nature of the material, therefore higher surface area coupled with higher pore volume and size constitutes a higher energy density. From the data it is clear that MPF-CeO_2-CB has a higher S.A of 16.12 m^2g^{-1} than that of MPF-CeO_2-C at 13.59 m^2g^{-1}, however, MPF-CeO_2-CB falls short in the pore volume which is 11% (0.1518 m^3g^{-1}) smaller than that of MPF-CeO_2-C which has a pore volume of 0.1705 m^3g^{-1}, also its pore size is 34.29 nm whilst MPF-CeO_2-C has a pore size of 46.60 nm. This data implies that although MPF-CeO_2-CB may have a higher surface area than that of MPF-CeO_2-C, meaning that it has a more exposed area for easy accessibility of the electrolyte electrode interface, unfortunately, it falls short in pore volume and size. It is safe to assume that MPF-CeO_2-C will have a much higher energy storage capabilities and this may be due to the in-situ addition of carbon which expands the pore size of the structure, this will be interrogated in the electrochemical behavior and performance.

The data also indicates that CeO_2 stabilizes both sample structures whilst offering more pores as charge transportation channels and storage as seen from the spider-web like morphology observed in SEM. The BET isotherm-plots were analyzed as shown in figure **Fig. 5.7** (**a, b**) both materials reveal a Type IVa classification characteristic of mesoporous materials, at pressures 0.8-1.0, there is a small Type H1 hysteresis loop which might be due to capillary condensation in the mesopores, this hysteresis is no surprise since it is observed for materials with pores wider than ~4 nm of which both MPF-CeO_2-CB (34.29 nm) and MPF-CeO_2-C (46.50 nm) exceed, followed by a sharp rise in N_2 gas adsorption volume suggests the formation of secondary mesopores due to particle aggregation which confirms the results obtained in SEM and TEM, in which MPF-CeO_2-CB reaches to nearly ~100 cm^3g^{-1} and MPF-CeO_2-CB to nearly ~120 cm^3g^{-1} of gas adsorption due to the 2%-CeO_2 and carbon coating that further envelopes the materials by forming a protective shell coating causing particle aggregation as seen in SEM **Fig. 5.4** (**a, to c**) and TEM **Fig. 5.5** (**d, to f**).

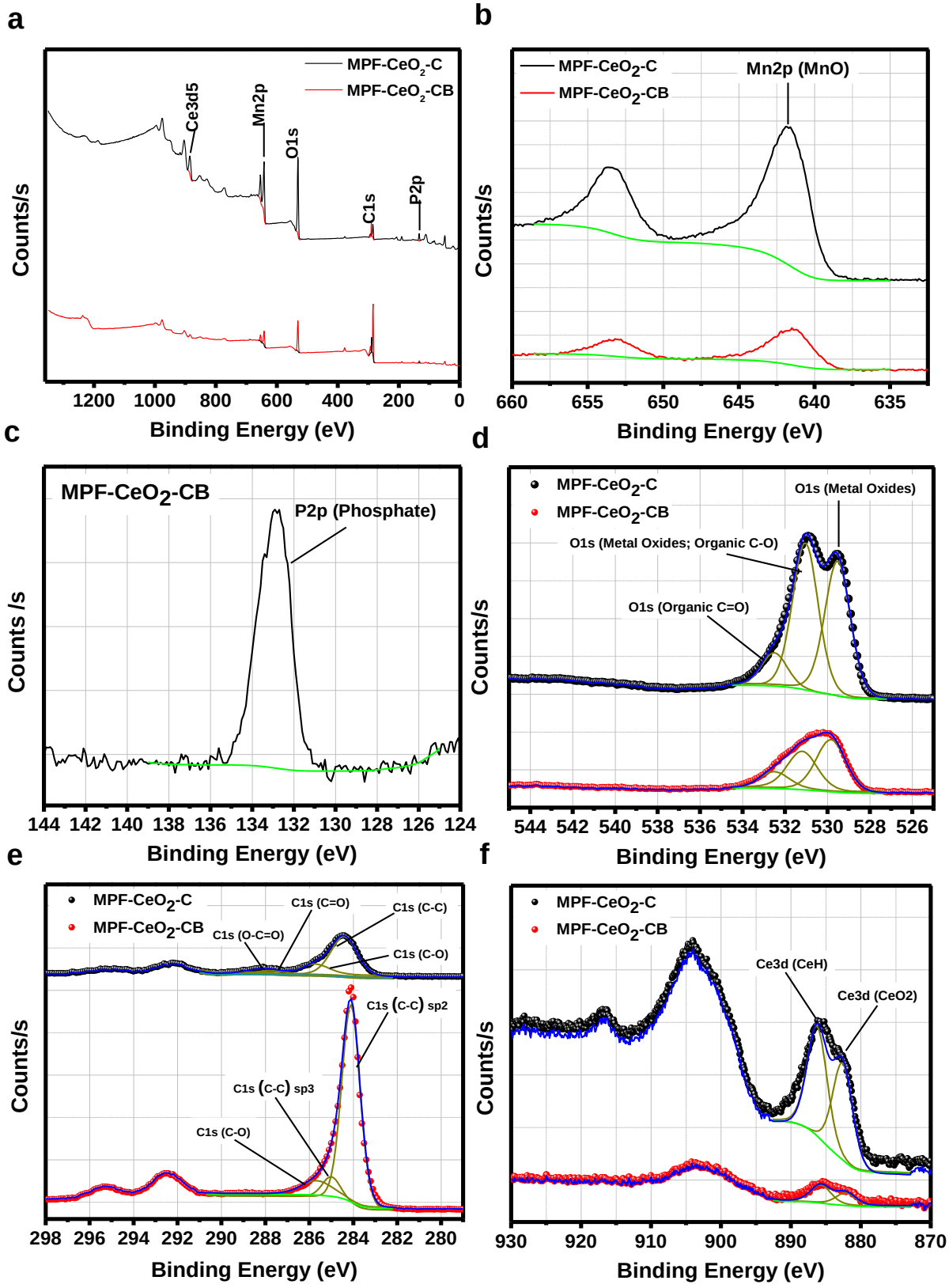


Fig. 5.8 | X-Ray Photo spectroscopy (XPS) of MPF-CeO2-CB. XPS survey spectra (**a**), Mn2p (**b**), P2p3 (**c**), O1s (**d**) and F1s (**e**)

Table 5. 4 : MPF-CeO_2-CB and MPF-CeO_2-C Survey Elemental ID and Quantification

Name	Peak BE (MPF-CeO_2-CB)	Peak BE (MPF-CeO_2-C)	Atomic % (MPF-CeO_2-CB)	Atomic % (MPF-CeO_2-C)
C1s	284.2	530.7	68.6	56.1
O1s	530.8	284.7	22.1	18.2
Mn2p	641.8	642.1	4.2	16.4
P2p	132.8	133.0	2.0	6.1
Ce3d5	884.4	884.8	0.3	2.3

Table 5. 5 : MPF-CeO_2-CB and MPF-CeO_2-C Peak ID and Quantification

Name	Peak BE (MPF-CeO_2-CB)	Peak BE (MPF-CeO_2-C)	Atomic % (MPF-CeO_2-CB)	Atomic % (MPF-CeO_2-C)
P2p3 (Phosphate)	132.6	132.8	2.3	6.5
C1s (C-C) sp2	284.1		55.8	
C1s (C-C) sp3	285.0		6.0	
C1s (C-C)		284.4		15.5
C1s (C-O)	285.7	285.7	6.3	3.5
C1s (C=O)		287.8		1.4
C1s (O-C=O)		288.5		1.0
O1s (Metal Oxides)	292.8	529.5	10.0	6.5
O1s (Metal Oxides; Organic C-O)	531.2	531.0	7.2	15.5
O1s (Organic C=O)	532.5	532.5	3.1	3.5
Mn2p (MnO)	641.5	641.7	4.3	1.4
Ce3d (CeO2)	882.1	882.6	0.1	1.0
Ce3d (CeH3)	885.7	886.2	0.1	22.3

The XPS elemental analysis was done for MPF-CeO_2-CB and MPF-CeO_2-C displayed in **Fig. 5.8** and **Table 5.4** and **Table 5.5** which represent the elemental ID, Peak ID, and quantification. The survey scan is depicted in **Fig. 5.8** (**a**), MPF-CeO_2-CB has Manganese oxide (MnO) Mn2p is positioned at 641.5 eV with 4.3% atomic content.

The most prominent peak belongs to C1s carbon with C-C sp2 bonding positioned at 284,1 eV with 55.8% atomic content and C-C sp3 bonding positioned at 285.0 eV with

6.0% atomic content, this confirms what is observed in Raman with more sp3 bonds being broken to form sp2 bonds. The other deconvoluted carbon peak is for C1s C-O bonding positioned at 285.7eV with 6.3% atomic content.

and phosphate P2p3 positioned at 132.6 eV with 2.3% atomic content, along with O1s (Metal oxide; organic C-O) at 529.8eV (7.2%), O1s (metal oxides) at 532.5 eV (10%) and O1s (organic C=O) at 532.5 eV (3.1%) all demonstrate that original MPF triplite material is still in-tact with additional carbon-oxygen bonds. Ce3d (CeO_2) is positioned at 882.1 eV with 0.1% atomic content and Ce3d (CeH3) is positioned at 885.7 eV with 0.1% atomic content, this shows that the coating by 2%-CeO_2 was insignificant since the atomic amounts are really small thus correlating with the observed SEM and TEM images, were some of the particles were not fully coated. The next step is to determine how will this affect the electrochemical performance.

The XPS elemental analysis was done for MPF-CeO_2-C displayed in **Fig. 5.8** and **Table 5.5** and **Table 5.6** represent the elemental ID, Peak ID, and quantification. The XPS analysis was done to understand the contribution of CeO_2 coating and carbon in-situ coating on MPF. The most prominent peak belongs to C1s carbon with C-C bonding poisoned at 284,4 eV with 15.5% atomic content. O1s (metal oxides) positioned at 530.7 eV, upon deconvolution the peaks appear to be split in two, the first positioned at 529.5 eV with 21.1% atomic content and the second at 531.0 eV with 24.4% atomic content, this means that CeO_2 causes the MPF metal oxide peak to split and its electrochemical performance shall be studied in **chapter 4** to underline its significance. Mn2p manganese oxide peak is positioned at 641.6 eV with atomic content 16.1% this confirms the octahedra formed by manganese and oxygen. The phosphate P2p3 is positioned at 132.8 eV with metal content of 6.5%. Lastly, the deconvoluted Ce3d (CeO_2) is positioned at 882.6eV with 0.8% atomic content and another Ce3d belonging to CeH is positioned at 886.2eV with atomic content 0.9%. Comparing the two materials it is evident that MPF-CeO_2-CB has more C-C sp2

bonding and the results confirm that both in-situ and ex-situ carbon coating do not affect the integrity of the material.

5.2.2 Electrochemical Characterization

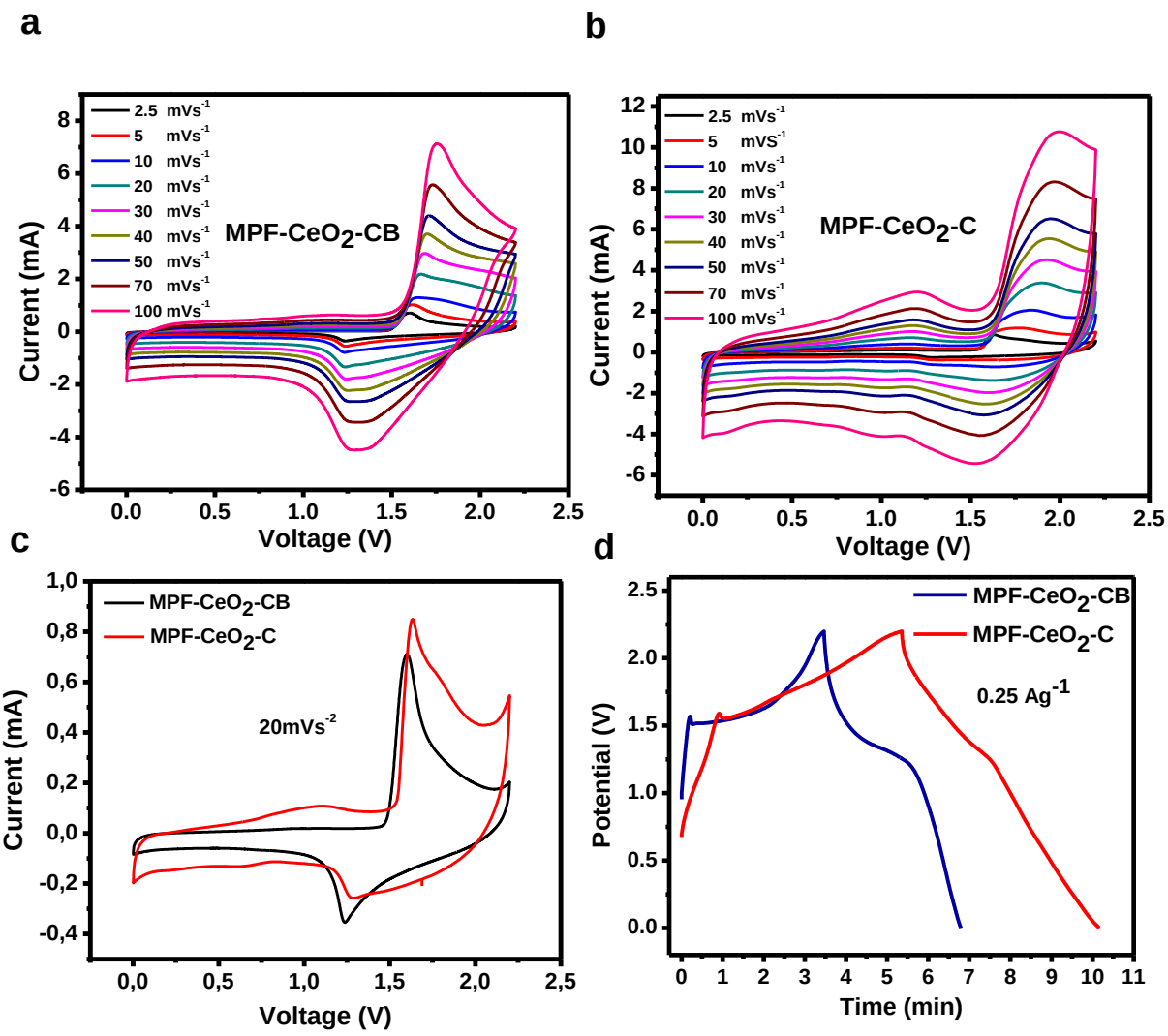


Fig. 5.9 | Electrochemical behaviours of MPF-CeO_2-CB and MPF-CeO_2-C batteries with 4 M $NaClO_4$ as electrolyte. Cyclic voltammograms (CVs) at 2.5 to 70 mVs^{-1} MPF-CeO_2-CB (**a**), MPF-CeO_2-C (**b**), CV comparison of MPF-CeO_2-CB and MPF-CeO_2-C at 20 mVs^{-1} (**c**) and galvanostatic charge-discharge (GCD) curve comparison for both MPF-CeO_2-CB and MPF-CeO_2-C at 0.25 Ag^{-1} (**d**)

Cyclic voltammetry was first investigated. **Fig. 5.9 (a and b)** shows the cyclic voltammograms (CVs) curves for MPF-CeO_2-CB (**a**) and MPF-CeO_2-C (**b**) respectively in 4 M $NaClO_4$ electrolyte fabricated using the T-type cell with a voltage window of 0-2.2 V. Within the first observation, MPF-CeO_2-CB has one pair of

oxidation/reduction peaks and MPF-CeO_2-C has two pairs of oxidation/reduction peaks. From 0 to 1 V MPF-CeO_2-CB has a capacitive shape whilst MPF-CeO_2-C has a pseudocapacitive shape and after 1V they resemble a battery-type material with redox peaks signifying oxidation and reduction of species. For MPF-CeO_2-CB (**a**) the anodic peak as the sweep rate is increased the peaks begin to broaden and start to shift slightly towards higher potentials appearing within the range of 1.59-1.75 V, this might be due to increased polarization at higher sweep rates and the cathodic peak appearing at 1.25-1.30 V, these oxidation/reduction peaks are corresponding with the galvanostatic charge-discharge plateaus observed in **Fig. 5.9** (**d**). MPF-CeO_2-C (**b**) CV has both pseudocapacitive and battery like resemblance which is different to what is observed for MPF-CeO_2-CB, with peak broadening and shifting as sweep rate is increased, however, the shape is more pronounced and reaches higher current values than that of MPF-CeO_2-CB, meaning that more current is being generated and more ions pass through the channels of the material in which we can assume that MPF-CeO_2-C will have a much higher capacity than of MPF-CeO_2-CB which is also supported by the high mesoporous size observed in the BET analysis, this assumption will be further interrogated under electrochemical performance. MPF-CeO_2-C has two pairs of oxidation/reduction peaks, the first pair occurs at lower potentials and the other occurs at higher potentials and as the sweep rate increases the anodic peaks shift to higher potentials from 1.28-1.53 V and 1.63-2.0 V with the cathodic peaks occurring at 0.65-0.99 V and 1.11-1.20 V, these oxidation/reduction peaks are also corresponding with the galvanostatic charge-discharge plateaus observed in **Fig. 5.9** (**d**). The comparison CV curve is displayed in **Fig. 5.9** (**c**) at 20 mVs^{-1}, just to further highlight the difference between the two, confirming that MPF-CeO_2-C is more pronounced than MPF-CeO_2-CB, while MPF-CeO_2-C has two pairs of oxidation/reduction peaks it has been proposed that the anodic and cathodic peaks represent the oxidation and reduction of Mn from Mn^{2+} to Mn^{3+} and then from Mn^{3+} to Mn^{4+} which might indicate a presence of two phases undergoing a structural transition, as for the pseudocapacitive peak observed at lower potentials might be attributed to the addition of citric acid and CeO_2 contributions enhancing the materials electrochemical performance. The galvanostatic charge-discharge curve comparison is highlighted in **Fig. 5.9** (**d**) at 0.25 Ag^{-1}, it is clear that both materials have a battery like properties based on the redox peaks, however, MPF-CeO_2-C leans towards both pseudocapacitive and battery-like properties since the second plateau does not show

full redox properties, it is also evident that the 15% coating by citric acid does, however, cause a change in the CV and the charge-discharge curves. The discharge time for MPF-CeO_2-CB was reported to be 7 mins and for MPF-CeO_2-C 10 mins, with this information we expect MPF-CeO_2-C to have a higher capacity than MPF-CeO_2-CB.

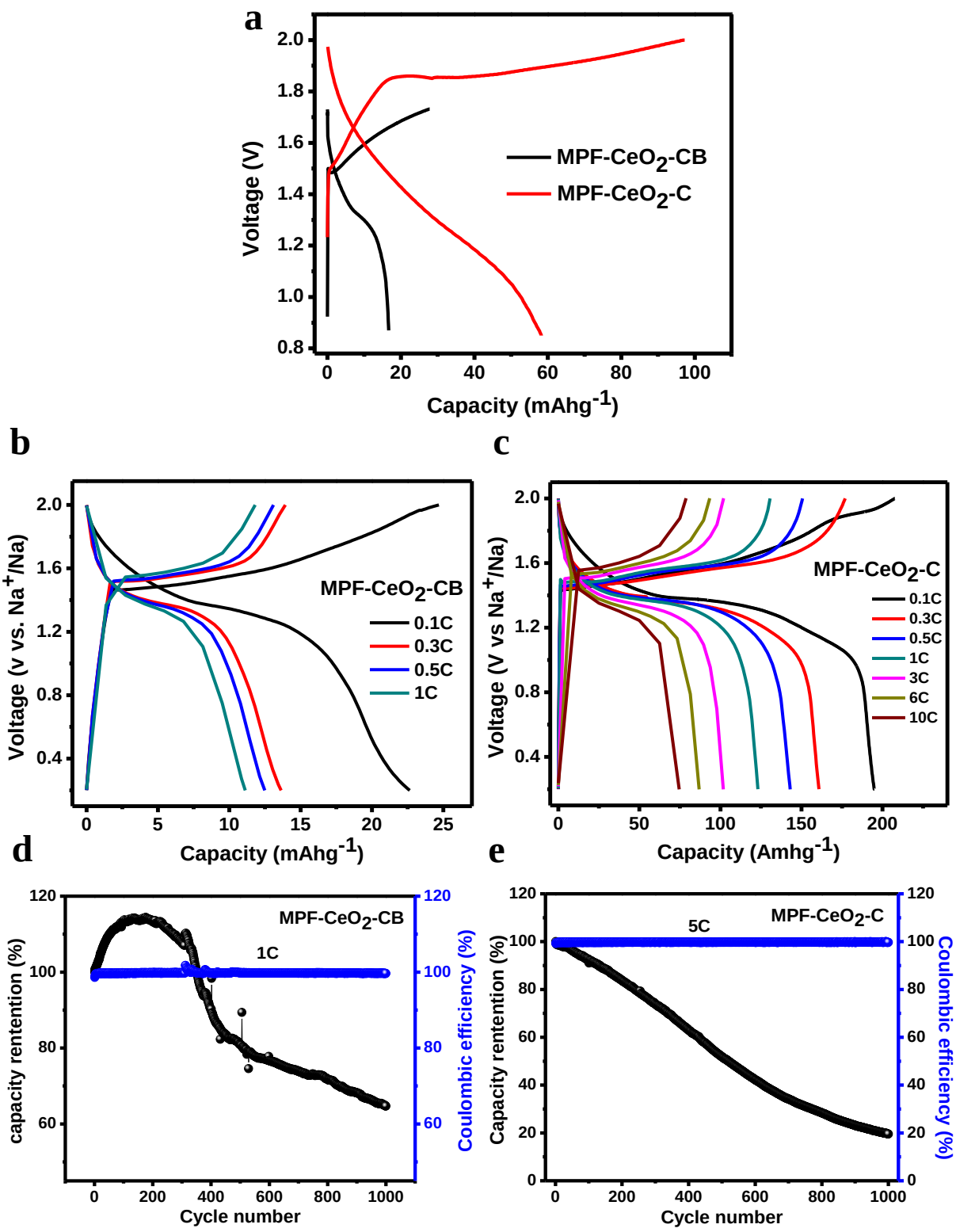


Fig. 5.10 | Electrochemical performance of MPF-CeO_2-CB and MPF-CeO_2-C batteries with 4 M $NaClO_4$ as electrolyte. Charge/discharge curve comparison of MPF-CeO_2-CB and MPF-CeO_2-C coin-cell battery at 0.1C (**a**), Rate performance of MPF CeO_2-CB at 0.1, 0.5, 0.5C and 1C using a T-cell battery (**b**) , Rate performance of MPF-CeO_2-C from 0.1C to 10C using a T-cell battery (**c**), cyclic performance of MPF-CeO_2-CB using T-cell battery (**d**), cyclic performance of MPF-CeO_2-C using T-cell battery (**e**)

The electrochemical performance of MPF-CeO_2-CB and MPF-CeO_2-C were investigated as shown in **Fig. 5.10** (**a-e**) with 4M $NaClO_4$ as electrolyte. To understand the electrochemical performance of both these materials the first tests were conducted using a coin-cell battery at a rated capability of 0.1 C **Fig. 5.10** (a), at 0.1C MPF-CeO_2-CB charged and discharged at a voltage window of 0.85-1.72 V had a discharge capacity of 16.67 $mAhg^{-1}$, whilst MPF-CeO_2-C charged and discharged at a voltage window of 0.85-2.0 V had a discharge capacity of 58.27 $mAhg^{-1}$ which is a ~71% increase as compared to MPF- CeO_2-CB, these results are in agreement with the electrochemical behaviours observed previously in **Fig. 5.9**, were MPF-CeO_2-C had a higher response current and longer discharge time which does indeed correlate with obtaining a higher capacity, however, these results are extremely far apart in comparison than what we had anticipated, we had assumed they would have similar or close discharge capacities due to the addition of carbon. Like **chapter 4** this led us to use the T-cell battery since manual packaging and screwing the components closely together are more efficient. The T-cell battery results obtained for MPF-CeO_2-CB **Fig. 5.10** (**b**) charged and discharged at a voltage window of 0.2-2.0 V rated at 0.1 C, 0.3 C, 0.5 C, and 1 C had a discharge capacity of 22.60, 13.62, 12.45 and 11.12 $mAhg^{-1}$ respectively which is are much better discharge capacities than that obtained from the coin-cell, however still very poor, whilst MPF-CeO_2-C charged and discharged at a voltage window of 0.2-2.0 V rated at 0.1 C, 0.3 C, 0.5 C, 1 C, 3 C, 6 C, and 10 C had discharge capacities of 195.16, 161.04, 142.97, 123.43, 101.99, 86.37 and 74.62 $mAhg^{-1}$ respectively, the results obtained were outstanding especially at 0.1C with a ~70% improvement in discharge capacity compared to that of using a coin cell. MPF-CeO_2-C has the best electrochemically performance and behaviours capable of achieving higher capacities if the electrolyte, zinc metal, and material characterization is optimized, this is heavily due to its impressive mesoporous pores, pore volume and pore size induced by CeO_2 coating and especially the carbon in-situ coating including to both pseudocapacitive and battery like properties as discussed addressed under the electrochemical behaviour led to an improvement in electrochemical performance.

The last step was determining the cyclic performance to observe material stability throughout cycles, the capacity retention for MPF-CeO_2-CB **Fig. 5.10** (**d**) went from 100% to 109.17% in just 319 cycles this increase may be due to the formation of the

SEI (solid electrolyte interface) and also the periodic activation of the active material[62], however, started to decrease drastically to 64.24% of its initial capacity at the 1000th cycle with the coulombic efficiency remaining at $\pm$ 99% before the total collapse of the active material. Furthermore X.Wu et al.[64] upon investigating the cyclic performance of $ZnMn_2O_4$ they discovered a similar initial increase and then a sharp decrease in a capacity similar to what is observed in MPF-CeO_2-CB in the which the capacity decay may be attributed it to oxidation of Mn^{2+} and the disproportionation reaction of MnOOH. As for MPF-CeO_2-C **Fig. 5.10** (**e**) the capacity retention after 1000 cycles was 19.91%, with a steady $\pm$ 99% coulombic efficiency. However, both these materials undergo capacity decay over 1000 cycles, it is clear that the coating of CeO_2 is not the most optimal. It is important to note that manganese-based aqueous ZiBs cathode materials suffer from manganese dissolution that leads to capacity decay of the battery as well as depressed reaction kinetics are still a major obstacle in many Mn containing compounds which were reported by G.Fang et al.[63] Which is also explained in detail in **Chapter 4.2.2** along with other underlying issues.

Initially, we wanted to investigate the electrochemical performance of both MPF-CeO_2-CB and MPF-CeO_2-C materials, however, we have discovered possible major obstacles along the way which need to be addressed, there is a lot of future work to be done to perfect and optimize our battery.

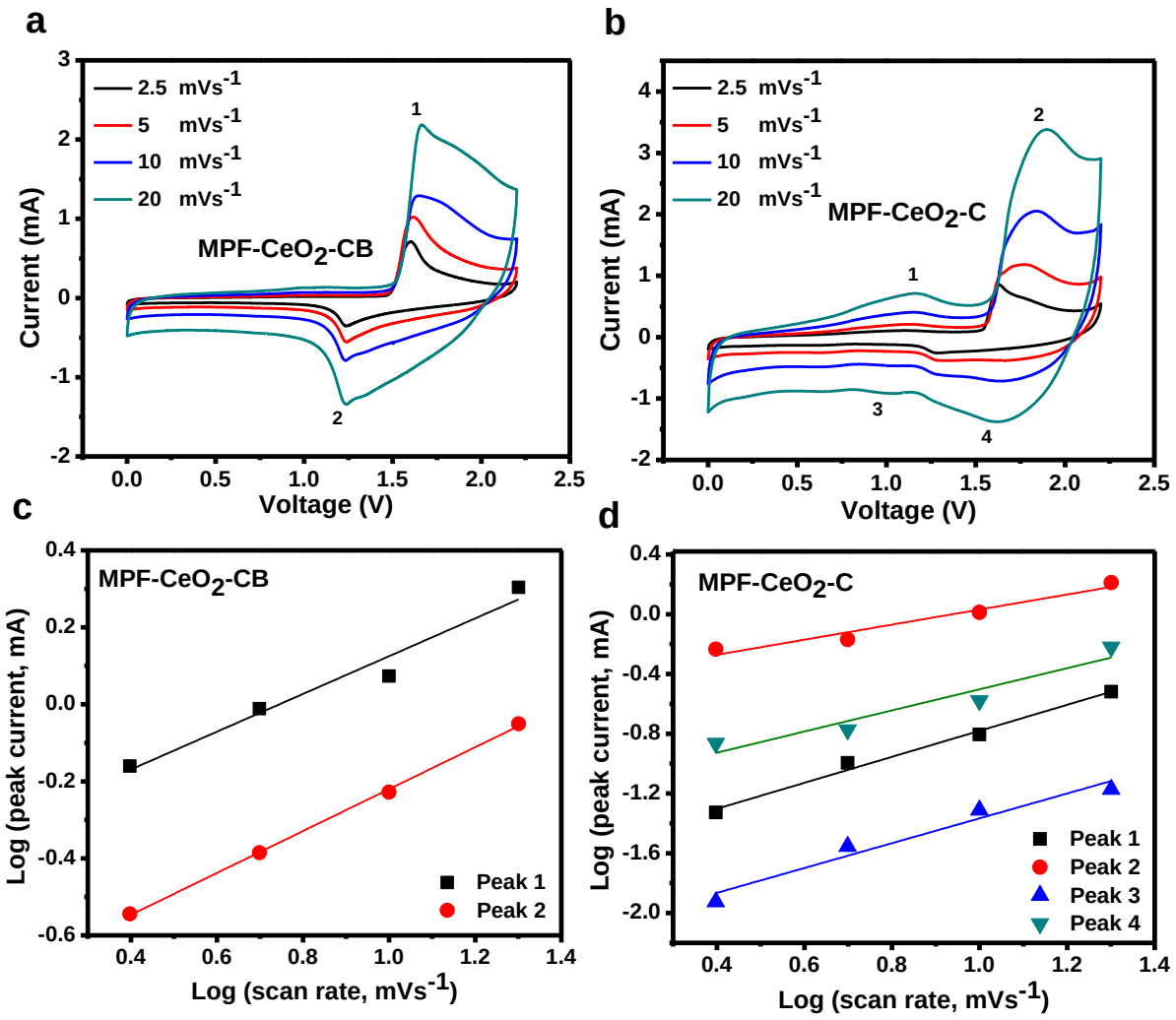


Fig. 5.11 | Electrochemical analysis of different kinetic responses. Active electrode material electrochemical CV curves for MPF-CeO_2-CB (a) and MPF-CeO_2-C (b) at sweep rates 2.5 to 20 mVs^{-1}, the dependence of parameter b on: MPF-CeO_2-CB (c) and MPF-CeO_2-CB (d)

To further understand the high electrochemical performance of the MPF-CeO_2-CB and MPF-CeO_2-C as battery materials it significantly depends on their kinetics origin, which has been investigated by CV characterizations. **Fig. 5.11** displays the CV curves of the MPF-CeO_2-CB (a) and MPF-CeO_2-C (b) batteries at different sweep rates from 2.5 to 20 mVs^{-1} with a voltage window from 0.0-2.2 V. Their peak currents and sweep rates have a relationship where the total current measured under a potential sweep rate can give a sum of the current related to the current required to charge the electrochemical double layer at the electrolyte interface, to start fast faradaic reactions

on the electrode surface known as a surface-controlled capacitive process (i_{cap}) and slow ionic diffusion-controlled process (i_{diff}) as described in **Chapter 4.2.2**

The respective plots for log *i(v)* vs log *v* are shown in **Fig. 5.11** (**a, b**), were MPF-CeO_2-CB **Fig. 5.11** (**a**) has two peaks recognized as peak 1 (anodic) and peak 2 (cathodic), MPF-CeO_2-C **Fig. 5.11** (**b**) with four peaks recognized as peak 1 and 2 both being anodic with peak 3 and 4 being cathodic. The calculated *b* values for MPF-CeO_2-CB for peak 1 and peak 2 are 0.49 and 0.54, both peaks can be seen as slow ionic diffusion-controlled process indicating a battery-like material, meaning that the Na^+ intercalation reaction dominated the current at both peaks. The calculated *b* values for MPF-CeO_2-C for peak 1, peak 2, peak 3 and peak 4 are 0.87 and 0.50, 0.83 and 0.71 respectively, the electrochemical reactions are simultaneously controlled by semi-infinite linear ionic diffusion (battery-type) and pseudocapacitive, these findings correlate with the observed CV and charge-discharge response indicating both battery-like and pseudocapacitive reactions contribute massively towards the materials performance.

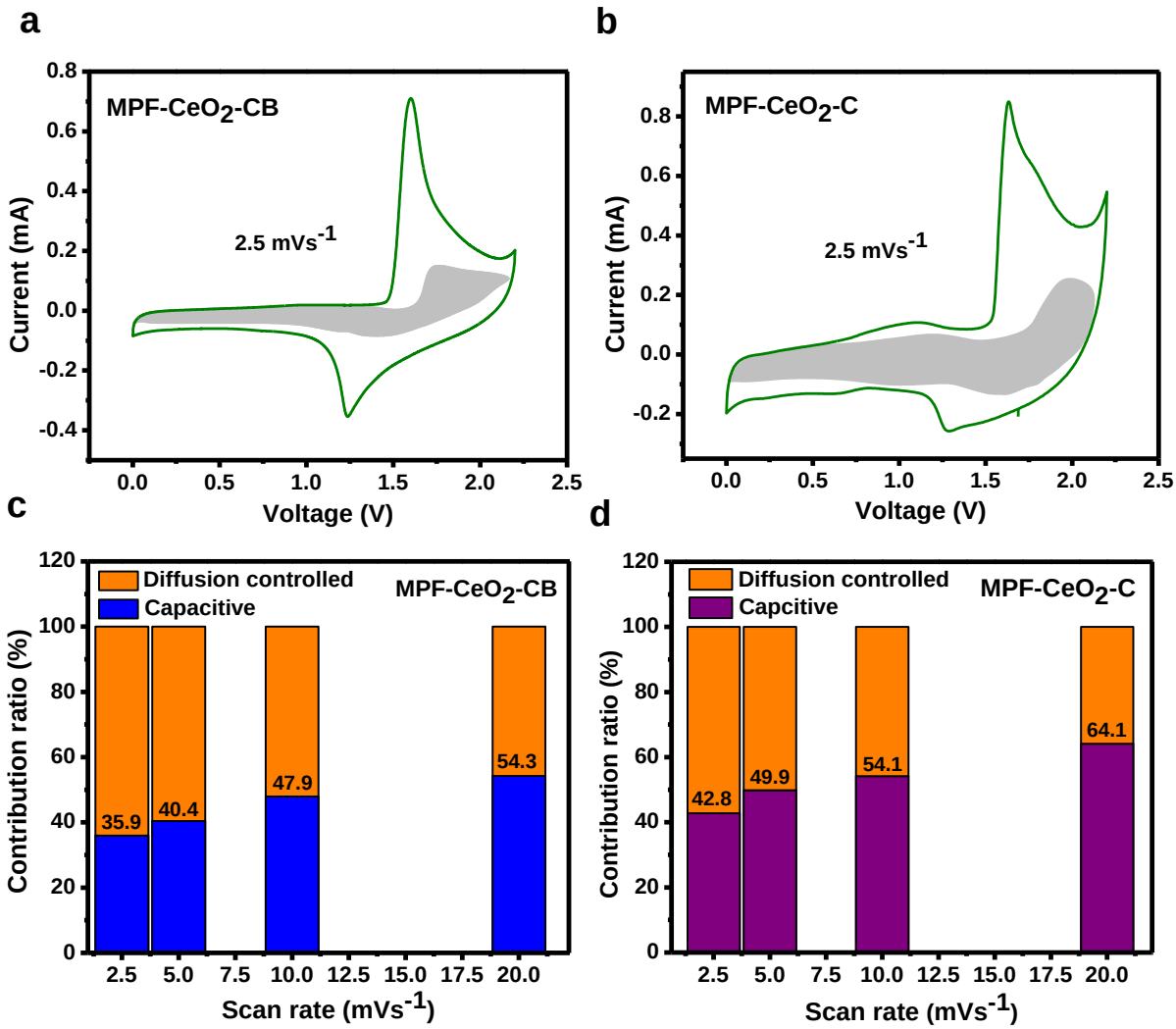


Fig. 5.12 | Differentiating capacitive effect from diffusion-controlled process using Dunn's Method. CV curves with the capacitive contribution fraction depicted by the shaded area at sweep rate 2.5 mVs^{-1} MPF-CeO_2-CB (**a**) and MPF-CeO_2-C (**b**), Capacitive contribution bar chart at sweep rates 2.5, 5, 10 and 20 mVs^{-1} MPF-CeO_2-CB (**c**) and MPF-CeO_2-C (**d**) respectively.

The pseudocapacitive contribution can be determined from different sweep rates calculated by the following equations known as the Dunn's method with equations discussed in **Chapter 4.2.2**

From the plot of $i/v^{1/2}$ vs $v^{1/2}$ (5) gives k_1 and k_2 **appendix A2** (**c**, **d**) depicts the plot at fixed potentials for MPF-CeO_2-CB at 0.3V, 0.6V and 1.0V, for MPF-CeO_2-C at 0.3 V, 0.6 V and 1.2 V with the capacitive contribution highlighted in gray at 2.5 mVs^{-1} **Fig. 5.12** (**a**, **b**). The calculated capacitive contribution measured at sweep rates 2.5 to 20

mVs^{-1} for MPF-CeO_2-CB are 35.9%, 40.4%, 47.9% and 54.3% as for MPF-CeO_2-C 42.8%, 49.9%, 54.1%, 64.1%, as shown in **Fig. 5.12** (**c**, **d**), as the sweep rate increases the contribution ratios of the capacitive mechanism is evaluated to increase with sweep rate, with the diffusion contribution seen to remain dominant over lower sweep rates and at higher scan rates is seen as mild transitions between battery-type and pseudocapacitive reactions, however, ionic-diffusion seems to be dominant in MPF-CeO_2-CB than capacitive-control which is in great agreement with the *b* value data obtained, thus indicating that MPF-CeO_2-CB is kinetically dominated by the diffusion-controlled process at the potential 0-2.2 V. On the other hand, MPF-CeO_2-C is simultaneously controlled by both ionic-diffusion and capacitive-control which is also in agreement with the *b* value data obtained, this phenomenon is the main reason why MPF-CeO_2-C has great electrochemical behaviour and performance.

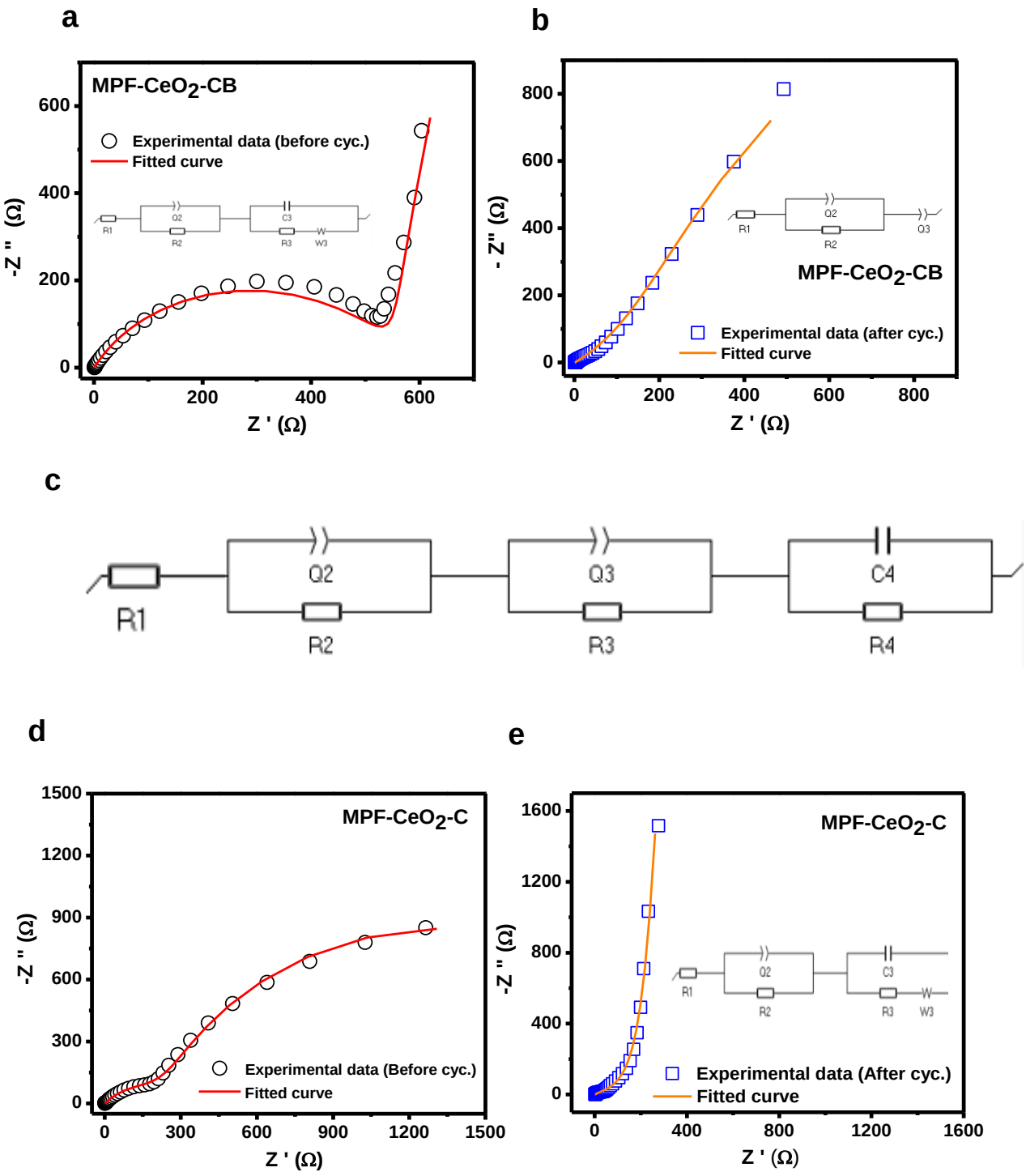


Fig. 5.13 | Electrochemical impedance spectroscopy (EIS). MPF-CeO_2-C before cycling stability (**a**) and after cycling (**b**), equivalent circuit (**c**)

Table 5. 6 : Electrochemical Impedance spectroscopy

	MPF-CeO_2-CB - before cycling	MPF-CeO_2-CB -after cycling	MPF-CeO_2-C before cycling	MPF-CeO_2-C after cycling
$R1_S$ (Ω)	0.6604	1.154	0.08449	23.58×10^{-15}
$R2_{ct}$ (Ω)	564.5	1.786	2213	459.9
$R3_{ct}$ (Ω)	14.19		255.6	
$R4_{ct}$ (Ω)			2598	
$Q2_{cpe}$ (Fs^{-1})	0.217×10^{-3}	0.03255	3.399×10^{-3}	5.201×10^{-3}
$Q3_{cpe}$ (Fs^{-1})		7.554×10^{-3}	0.6647×10^{-3}	0.01108
C4 (F)	0.02499		1811×10^{-6}	

The electrochemical impedance spectra (EIS) was recorded using an AC at 10 mV and the impedance spectra are fitted using an equivalent circuit, **Fig. 5.13** displays the results of both materials before and after cycling using a T-cell battery. **Table 5.7** summarizes the obtained data from fitting the equivalent circuit, $R1_S$ represents the solution resistance, $R2_{ct}$, $R3_{ct}$ $R3_{ct,}$ and $R4_{ct}$ represent the charge-transfer resistance, $Q2_{cpe}$ and $Q3_{cpe}$ represent the constant phase element (CPE) related to double-layer capacitance, C4 represents capacitance and W3 the Warburg diffusion.

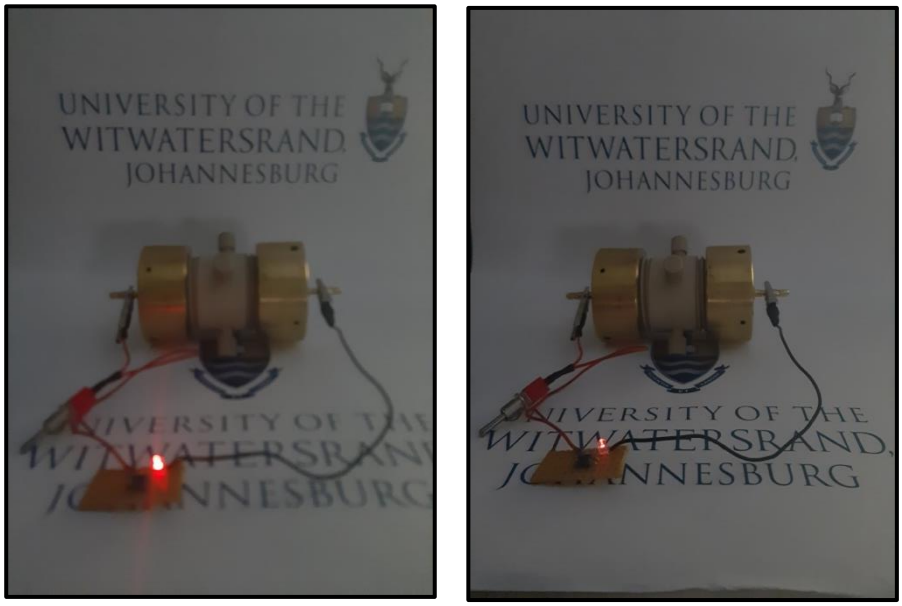
The comparison of MPF-CeO_2-CB before and after cycling, the results obtained show that the material before cycling is in agreement with the diffusion-controlled process and after cycling, it loses its capabilities which also correlates with the materials destabilization observed over 1000 cycling. EIS Before cycling has a semi-circle followed by capacitive diffusion characterized by the following elements $R1_S$, $R2_{ct}$, $R3_{ct}$, $Q2_{cpe}$ and $Q3_{cpe,}$ and EIS-after cycling is characterized by the elements $R1_S$, $R2_{ct}$, $Q2_{cpe,}$ and $Q3_{cpe}$.

The comparison of MPF-CeO_2-C EIS before and after cycling reveals that the material changes since the fitted equivalent circuit for before and after cycling is two different circuits that are both connected in series. The EIS-before cycling has two semi-circles, at higher frequency region (first semi-circle) is characterized by $R1_S$, $Q2_{cpe,}$ and $R2_{ct}$, the mid-frequency region (second semi-circle) is characterized by $Q3_{cpe}$ and $R3_{ct}$ and the higher frequency region is characterized by C4 and $R4_{ct}$, which correlate well with the results obtained for the capacitive contribution in which the reactions are

simultaneously controlled by both ionic-diffusion and capacitive-control. MPF-CeO_2-C after cycling has elements $R1_S$, $Q2_{cpe}$, $R2_{ct,}$ and $Q3_{cpe}$, characterized by a half semi-circle followed by an almost $\sim 90°$ straight line up the -Z" y-axis. This shows that the materials undergo some change within the internal structure further explaining the truth behind dissolution and decrease instability of the material of a period of cycles which was mention in **Fig 5.13** (**e**).

5.2.3 Application

a **MPF-CeO_2-CB**



b **MPF-CeO_2-C**

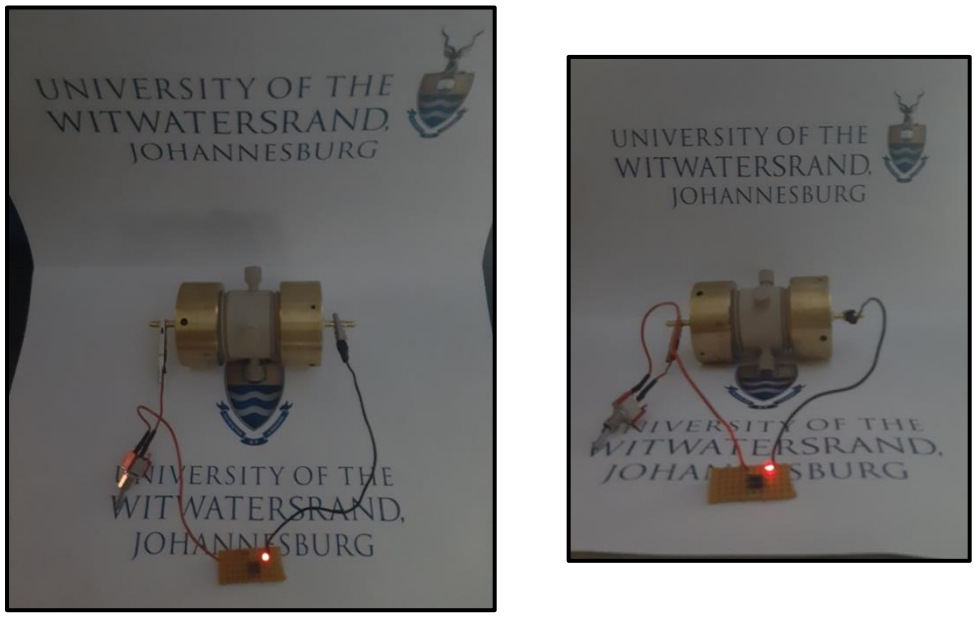


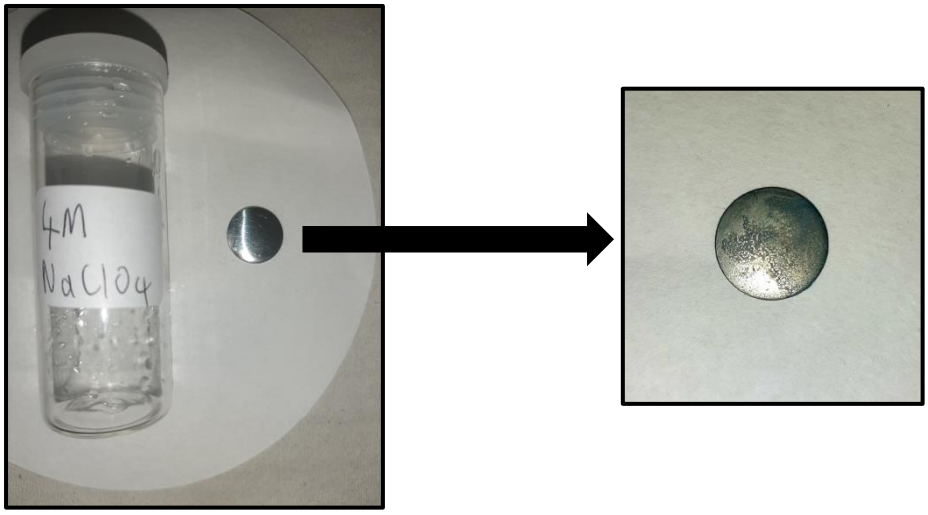
Fig. 5.14 | Application tests. MPF-CeO_2-CB 11 mins:07.80 secs (**a**), MPF-CeO_2-C 35 mins:05.76 secs (**b**)

The last experiment that was performed as to test the battery as an energy storage device as proof of application that the materials can be used for commercial purposes **Fig.5.14** (**a, b**). The test was to determine which battery material will have the longest discharge time, meaning a larger energy density, this test is to solidify our electrochemical behavior and performance data as we had assumed that MPF-CeO_2-C shall have high energy storage characteristics over MPF-CeO_2-CB. The results are as follows, MPF-CeO_2-CB had a discharge time of 11 mins:07.80 secs and MPF-CeO_2-C had a discharge time of 35 mins:05.76 secs, indeed our predictions were true, therefore indicating that our electrochemical data is correct and precise with MPF-CeO_2-C being the materials with the best electrochemical performance and is the most suitable for commercial immobile energy storage applications.

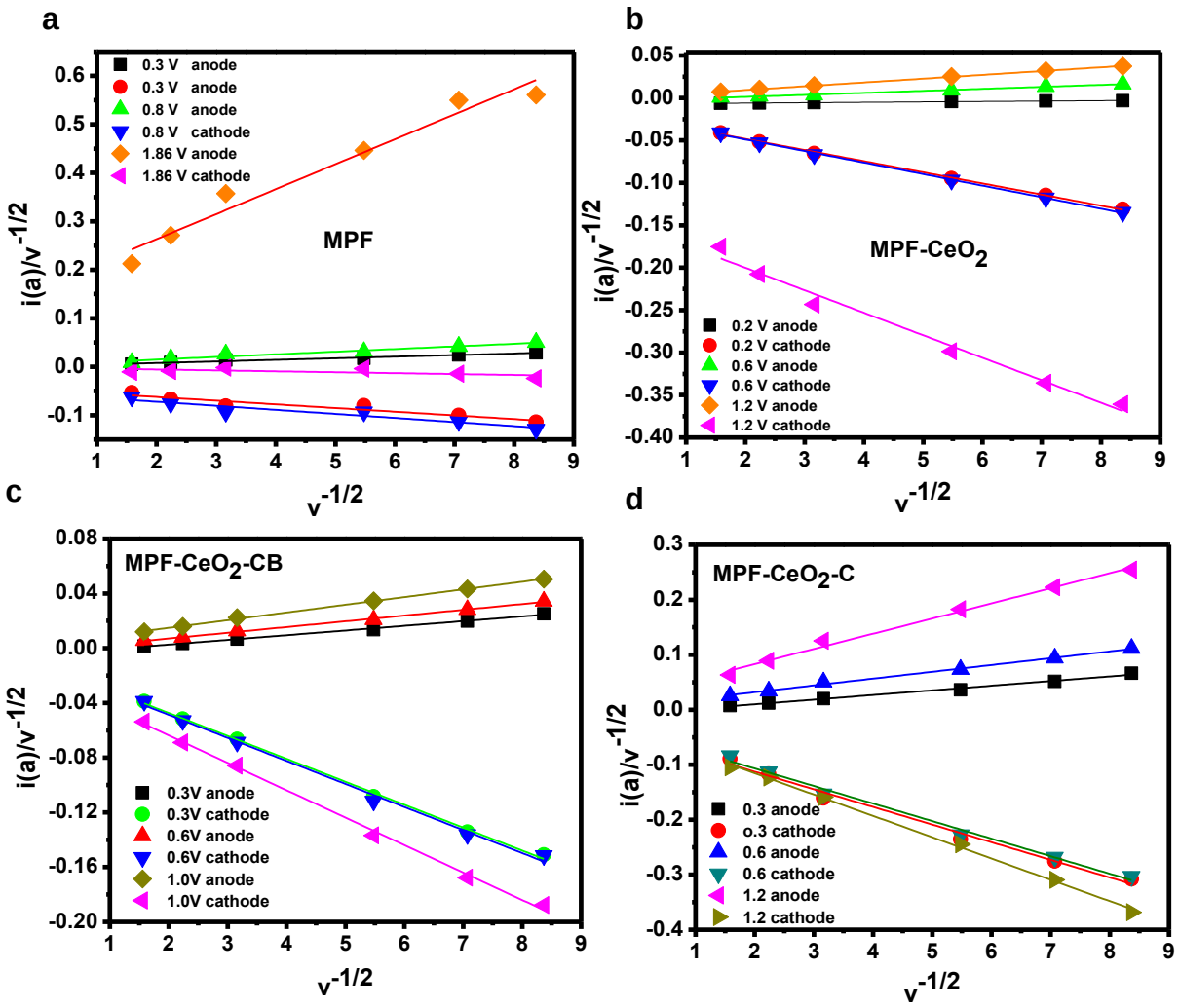
5.3 Conclusion

In summary, the attempt to improve the triplite synthesis of MPF-CeO_2-CB and MPF-CeO_2-C via microwave synthesis, 2% coating of CeO_2 and incorporating carbon coating both in-situ and ex-situ were successfully achieved. The XRD, Raman and IR results reveal that both materials were successfully obtained with XPS displaying the elements along with their respective bonding configurations involved, minor impurities were also observed in XRD which may result in some side products or starting materials obtained. From analyzing the electrochemical data, specifically looking at the T-type cell MPF-CeO_2-CB at 0.1 C, 0.3 C, 0.5 C, and 1 C gave 22.60, 13.62, 12.45 and 11.12 $mAhg^{-1}$ while MPF-CeO_2-C at 0.1 C, 0.3 C, 0.5 C, 1 C, 3 C, 6 C, and 6 C had 195.16, 161.04, 142.97, 123.43, 101.99, 86.37 and 74.64 $mAhg^{-1}$ both charged and discharged within a potential window of 0.2 to 2.0 V, these results reveal that MPF-CeO_2-C has greater energy storage capabilities withstanding even higher C-rates. The stability analysis revealed that MPF-CeO_2-CB cycled at 1 C only maintained 64.24% at 1000 cycles with $\pm$ 99% CE and MPF-CeO_2-C cycled at 5 C had a capacity retention of 19.91% $\pm$ 99% CE also cycled for 100 times, which suggests that the coating by CeO_2 enhances the electrochemical behavior as well as the performance of MPF, while ex-situ carbon coating improves cycling performance. Similar to the samples analyzed in **Chapter 4** the reason for the crash instability is reported in the literature is caused by Mn^{2+} dissolution and zinc metal foil anode dendritic formation as well as stripping or plating. The analysis of different kinetic responses from CV reveals that MPF-CeO_2-CB had two peaks peak 1 and 2 with the following b values 0.49 and 0.54 respectively, whilst MPF-CeO_2-C four peaks peak 1, 2, 3 and 4 with the following b values at 0.87, 0.50, 0.83 and 0.71 respectively. By further differentiating capacitive effects from the diffusion-controlled process using Dunn's Method, the capacitive contributions were measured at sweep rates 2.5 to 20 mVs^{-1}. MPF-CeO_2-CB had 35.9%, 40.4%, 47.9% and 54.3% and MPF-CeO_2-C had 42.8%, 49.9%, 54.1% and 64.1%, these results reveal that MPF-CeO_2-CB kinetically dominated by the diffusion-controlled process. MPF-CeO_2-C is simultaneously controlled by both ionic-diffusion and capacitive-control, this makes MPF-CeO_2-C the most desirable battery material for zinc-metal anode aqueous sodium-ion batteries.

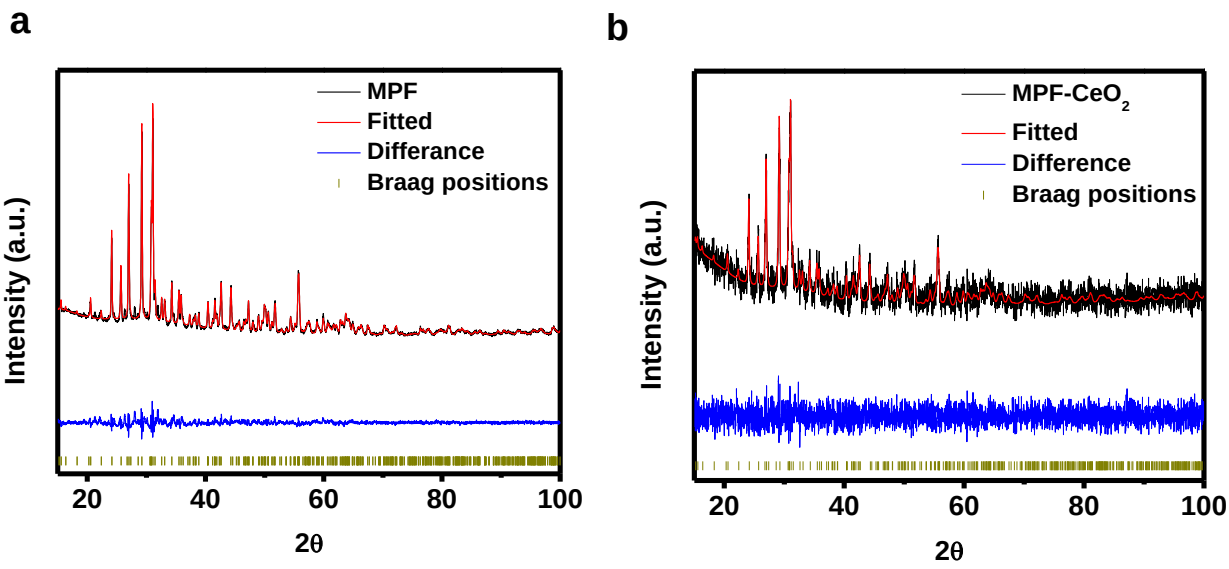
Appendix



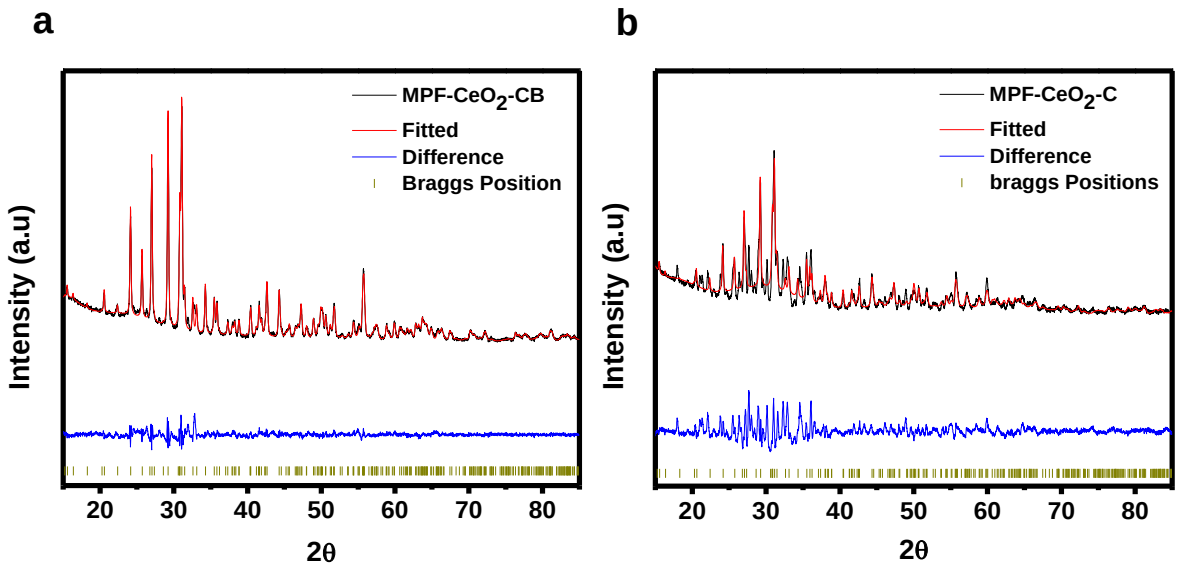
Appendix A1 | Soaked Zn-metal anode in 4M $NaClO_4$ aqueous electrolyte. Pure Zn-metal before being soaking (**a**), after soaking for 4 weeks (**b**)



Appendix A2 | Capacitive contribution calculations for plotting the capacitive and diffusion-controlled percentages as a bar graph and cyclic voltammetry. MPF (**a**), MPF-CeO_2 (**b**), MPF-CeO_2-CB (**c**) and MPF-CeO_2-CB (**d**)



Appendix A3 | PXRD Rietveld Refinement. MPF (**a**) and MPF-CeO_2 (**b**)



Appendix A4 | PXRD Rietveld Refinement of MPF-CeO_2-CB (**a**) and MPF-CeO_2-C (**b**)

References

1. Hall, P. J. & Bain, E. J. Energy-storage technologies and electricity generation. *Energy Policy* **36**, 4352–4355 (2008).

2. Ouedraogo, N. S. Opportunities, Barriers and Issues with Renewable Energy Development in Africa: a Comprehensible Review. *Curr. Sustain. Energy Reports* **6**, 52–60 (2019).

3. McLellan, B., Florin, N., Giurco, D., Kishita, Y., Itaoka, K. and Tzezuka, T., 2015.. Decentralised energy futures: The changing emissions reduction landscape. In The 22nd CIRO conference on Life Cycle Engineering. Elsevier. *Procedia CIRP* **29**, 138–143 (2015).

4. Pollet, B. G., Staffell, I. & Adamson, K. A. Current energy landscape in the Republic of South Africa. *Int. J. Hydrogen Energy* **40**, 16685–16701 (2015).

5. Chen, H. *et al.* Progress in electrical energy storage system: A critical review. *Prog. Nat. Sci.* **19**, 291–312 (2009).

6. Arunachalam, V. S. & Fleischer, E. L. The Global Energy Landscape and Materials Innovation. *MRS Bull.* **33**, 264–288 (2008).

7. Liu, J. Addressing the grand challenges in energy storage. *Adv. Funct. Mater.* **23**, 924–928 (2013).

8. Hwang, J. Y., Myung, S. T. & Sun, Y. K. Sodium-ion batteries: Present and future. *Chem. Soc. Rev.* **46**, 3529–3614 (2017).

9. Ehrlich, G. M. Handbook of Batteries 3rd Edition. *Handbook of Batteries* 35.1-35.94 (2002). doi:10.1016/0378-7753(86)80059-3

10. Wei, Y., Dai, S., Yu, J., Wu, S. & Wang, J. Research on status and prospects of

battery energy storage stations on energy internet. *Proc. 2019 IEEE 3rd Inf. Technol. Networking, Electron. Autom. Control Conf. ITNEC 2019* 964–969 (2019). doi:10.1109/ITNEC.2019.8729063

11. Wu, L. *et al.* Synthesis of carbon-coated Na2MnPO4F hollow spheres as a potential cathode material for Na-ion batteries. *J. Power Sources* **374**, 40–47 (2018).

12. Ni, Q., Bai, Y., Wu, F. & Wu, C. Polyanion-type electrode materials for sodium-ion batteries. *Adv. Sci.* **4**, (2017).

13. Guo, S. P., Li, J. C., Xu, Q. T., Ma, Z. & Xue, H. G. Recent achievements on polyanion-type compounds for sodium-ion batteries: Syntheses, crystal chemistry and electrochemical performance. *J. Power Sources* **361**, 285–299 (2017).

14. You, Y. & Manthiram, A. Progress in High-Voltage Cathode Materials for Rechargeable Sodium-Ion Batteries. *Adv. Energy Mater.* **8**, 1–11 (2018).

15. Kumar, P. R., Jung, Y. H., Wang, J. E. & Kim, D. K. Na3V2O2(PO4)2F-MWCNT nanocomposites as a stable and high rate cathode for aqueous and non-aqueous sodium-ion batteries. *Journal of Power Sources* **324**, 421–427 (2016).

16. Shen, W. *et al.* Improved electrochemical performance of the $Na_3V_2(PO_4)_3$ cathode by B-doping of the carbon coating layer for sodium-ion batteries. *J. Mater. Chem. A* **3**, 15190–15201 (2015).

17. Shen, C. *et al.* $Na_3V_2(PO_4)_2F_3$@C dispersed within carbon nanotube frameworks as a high tap density cathode for high-performance sodium-ion batteries. *J. Mater. Chem. A* **6**, 6007–6014 (2018).

18. Zhao, A. J., Sonigara, K.K., Li, J., Chen, B., Zhang, J., Soni, S.S., Zhou, X., Cui, G. and Chen, L., 2017. A smart flexible zinc battery with cooling recovery ability. . Angewandte Chemie. 129(27), pp.7979-7983

19. Hwang, J.-Y., Myung, S.-T. & Sun, Y.-K. Sodium-ion batteries: present and future. *Chem. Soc. Rev.* **46**, 3529–3614 (2017).

20. Delmas, C. Sodium and Sodium-Ion Batteries: 50 Years of Research. *Adv. Energy Mater.* **8**, 1–9 (2018).

21. Slater, M. D., Kim, D., Lee, E. & Johnson, C. S. Sodium-ion batteries. *Adv. Funct. Mater.* **23**, 947–958 (2013).

22. Kundu, D. *et al.* Aqueous: Vs. nonaqueous Zn-ion batteries: Consequences of the desolvation penalty at the interface. *Energy Environ. Sci.* **11**, 881–892 (2018).

23. Wang, F. *et al.* Highly reversible zinc metal anode for aqueous batteries. *Nat. Mater.* **17**, 543–549 (2018).

24. Sun, K. E. K., Hoang, T. K. A., Doan, T. N. L., Yu, Y. & Chen, P. Highly Sustainable Zinc Anodes for a Rechargeable Hybrid Aqueous Battery. *Chem. - A Eur. J.* **24**, 1667–1673 (2018).

25. Yan, J. *et al.* Rechargeable hybrid aqueous batteries. *J. Power Sources* **216**, 222–226 (2012).

26. Konarov, A. *et al.* Present and Future Perspective on Electrode Materials for Rechargeable Zinc-Ion Batteries. *ACS Energy Lett.* **3**, 2620–2640 (2018).

27. Shen, W., Wang, C., Xu, Q., Liu, H. & Wang, Y. Nitrogen-doping-induced defects of a carbon coating layer facilitate Na-storage in electrode materials. *Adv. Energy Mater.* **5**, (2015).

28. Zhang, H. *et al.* Towards High-Performance Aqueous Sodium-Ion Batteries: Stabilizing the Solid/Liquid Interface for NASICON-Type Na2VTi(PO4)3 using Concentrated Electrolytes. *ChemSusChem* **11**, 1382–1389 (2018).

29. Triplite, A. MINERALOGY OF TRIPLITE E. Wn. HnrNucu, Uniaersity of Michigan, Ann Arbor, Michigan. 256–271 (1940).

30. Richmond, W.E., 1940. Crystal chemistry of the phosphates, arsenates and vanadates of the type A2XO4 (Z). American Mineralogist Journal of Earth and Planetary Materials, 25(7), pp.441-479.

31. Wolfe, C.W. and Heinrich, E.W., 1947. Triplite crystals from Colorado. American Mineralogist: Journal of Earth and Planetary Materials, 32(9-10), pp.518-526.

32. Haapala, I. & Ojanperä, P. Triplite and wolframite from a greisen-bordered veinlet in Eurajoki, SW Finland. *Bull. Geol. Soc. Finl.* **41**, 99–105 (2017).

33. WALDROP, L. The crystal structure of triplite, (Mn,Fe)2FPO4. *Zeitschrift für Krist. - Cryst. Mater.* **130**, 1–14 (2014).

34. Rea, J. R. & Kostiner, E. The crystal structure of manganese fluorophosphate, Mn 2 (PO 4)F . *Acta Crystallogr. Sect. B Struct. Crystallogr. Cryst. Chem.* **28**, 2525–2529 (2002).

35. Vignola, P., Gata, G. D., Hatert, F., Guastoni, A. & Bersani, D. On the crystal-chemistry of a near-endmember triplite, Mn2+2(PO4)F, from the Codera Valley (Sondrio Province, Central Alps, Italy). *Can. Mineral.* **52**, 235–245 (2014).

36. Tang, B., Shan, L., Liang, S. & Zhou, J. Issues and opportunities facing aqueous zinc-ion batteries. *Energy Environ. Sci.* **12**, 3288–3304 (2019).

37. Zhan, C. *et al.* Mn(II) deposition on anodes and its effects on capacity fade in spinel lithium manganate-carbon systems. *Nat. Commun.* **4**, 1–8 (2013).

38. Zhan, C., Wu, T., Lu, J. & Amine, K. Dissolution, migration, and deposition of transition metal ions in Li-ion batteries exemplified by Mn-based cathodes-A

critical review. *Energy Environ. Sci.* **11**, 243–257 (2018).

39. Ramulifho, T., Ozoemena, K. I., Modibedi, R. M., Jafta, C. J. & Mathe, M. K. Fast microwave-assisted solvothermal synthesis of metal nanoparticles (Pd, Ni, Sn) supported on sulfonated MWCNTs: Pd-based bimetallic catalysts for ethanol oxidation in alkaline medium. *Electrochim. Acta* **59**, 310–320 (2012).

40. Jafta, C. J., Mathe, M. K., Manyala, N., Roos, W. D. & Ozoemena, K. I. Microwave-assisted synthesis of high-voltage nanostructured LiMn 1.5Ni0.5O4 spinel: Tuning the Mn3+ content and electrochemical performance. *ACS Appl. Mater. Interfaces* **5**, 7592–7598 (2013).

41. Haruna, A. B. & Ozoemena, K. I. Effects of microwave irradiation on the electrochemical performance of manganese-based cathode materials for lithium-ion batteries. *Curr. Opin. Electrochem.* **18**, 16–23 (2019).

42. Kebede, M. A., Yannopoulos, S. N., Sygellou, L. & Ozoemena, K. I. High-Voltage LiNi 0.5 Mn 1.5 O 4- δ Spinel Material Synthesized by Microwave-Assisted Thermo-Polymerization: Some Insights into the Microwave-Enhancing Physico-Chemistry . *J. Electrochem. Soc.* **164**, A3259–A3265 (2017).

43. Nkosi, F. P. *et al.* Insights into the Synergistic Roles of Microwave and Fluorination Treatments towards Enhancing the Cycling Stability of P2-Type Na 0.67 [Mg 0.28 Mn 0.72]O 2 Cathode Material for Sodium-Ion Batteries . *J. Electrochem. Soc.* **164**, A3362–A3370 (2017).

44. Yao, J., Wu, F., Qiu, X., Li, N. & Su, Y. Effect of CeO2-coating on the electrochemical performances of LiFePO4/C cathode material. *Electrochim. Acta* **56**, 5587–5592 (2011).

45. Ha, H. W., Yun, N. J. & Kim, K. Improvement of electrochemical stability of LiMn2O4 by CeO2 coating for lithium-ion batteries. *Electrochim. Acta* **52**, 3236–3241 (2007).

46. Minakshi, M., Nallathamby, K. & Mitchell, D. R. G. Electrochemical characterization of an aqueous lithium rechargeable battery: The effect of CeO2 additions to the MnO2 cathode. *J. Alloys Compd.* **479**, 87–90 (2009).

47. Links, D. A., Li, H. and Zhou, H., Enhancing the performances of Li-ion batteries by carbon-coating : present and future. Chemical Communications. 48(9), pp. 1201–1217 (2012).

48. Das, R. S. & Agrawal, Y. K. Raman spectroscopy: Recent advancements, techniques and applications. *Vib. Spectrosc.* **57**, 163–176 (2011).

49. Bumbrah, G. S. & Sharma, R. M. Raman spectroscopy – Basic principle, instrumentation and selected applications for the characterization of drugs of abuse. *Egypt. J. Forensic Sci.* **6**, 209–215 (2016).

50. Thommes, M. *et al.* Physisorption of gases, with special reference to the evaluation of surface area and pore size distribution (IUPAC Technical Report). *Pure Appl. Chem.* **87**, 1051–1069 (2015).

51. Paynter, R. XPS Theory. 2000. INRS-Énergie, Matériaux et Télécommunications. Vol (1). pp 1-39.

52. Seyama, H., Soma, M. & Theng, B. K. G. *X-Ray Photoelectron Spectroscopy*. *Developments in Clay Science* **5**, (Elsevier Inc., 2013).

53. Elgrishi, N. *et al.* A Practical Beginner's Guide to Cyclic Voltammetry. *J. Chem. Educ.* **95**, 197–206 (2018).

54. Lin, X. *et al.* Exploiting Na2MnPO4F as a high-capacity and well-reversible cathode material for Na-ion batteries. *RSC Adv.* **4**, 40985–40993 (2014).

55. Wu, L. *et al.* Synthesis of carbon-coated Na2MnPO4F hollow spheres as a potential cathode material for Na-ion batteries. *Journal of Power Sources* **374**, 40–47 (2018).

56. Zhong, Y. *et al.* Micro-nano structure Na 2 MnPO 4 F/C as cathode material with excellent sodium storage properties. *Mater. Lett.* **145**, 269–272 (2015).

57. Zhu, C. *et al.* A High Power-High Energy Na3V2(PO4)2F3Sodium Cathode: Investigation of Transport Parameters, Rational Design and Realization. *Chem. Mater.* **29**, 5207–5215 (2017).

58. Jiang, X. *et al.* Extending the cycle life of Na $_3$ V $_2$ (PO $_4$) $_3$ cathodes in sodium-ion batteries through interdigitated carbon scaffolding. *J. Mater. Chem. A* **4**, 14669–14674 (2016).

59. Muraliganth, T., Stroukoff, K. R. & Manthiram, A. Microwave-solvothermal synthesis of nanostructured Li2MSiO 4/C (M = Mn and Fe) cathodes for lithium-ion batteries. *Chem. Mater.* **22**, 5754–5761 (2010).

60. Shi, S. *et al.* Full microwave synthesis of advanced Li-rich manganese based cathode material for lithium ion batteries. *Journal of Power Sources* **337**, 82–91 (2017).

61. Arges, C. G. *et al.* Anion Exchange Membrane Fuel Cells. *Elctrochemical Soc. Interface* 31–35 (2010). doi:10.3384/ecp110571227

62. Soundharrajan, V. *et al.* Aqueous Magnesium Zinc Hybrid Battery: An Advanced High-Voltage and High-Energy MgMn2O4 Cathode. *ACS Energy Lett.* **3**, 1998–2004 (2018).

63. Fang, G. *et al.* Suppressing Manganese Dissolution in Potassium Manganate with Rich Oxygen Defects Engaged High-Energy-Density and Durable Aqueous Zinc-Ion Battery. *Adv. Funct. Mater.* **29**, 1–9 (2019).

64. Wu, X. *et al.* Green-low-cost rechargeable aqueous zinc-ion batteries using hollow porous spinel ZnMn 2 O 4 as the cathode material. *J. Mater. Chem. A* **5**, 17990–17997 (2017).

65. Alfaruqi, M. H. *et al.* Electrochemically induced structural transformation in a γ-MnO2 cathode of a high capacity zinc-ion battery system. *Chem. Mater.* **27**, 3609–3620 (2015).

66. Pan, H. *et al.* Reversible aqueous zinc/manganese oxide energy storage from conversion reactions. *Nature Energy* **1**, (2016).

67. Bak, S. M., Shadike, Z., Lin, R., Yu, X. & Yang, X. Q. In situ/operando synchrotron-based X-ray techniques for lithium-ion battery research. *NPG Asia Mater.* **10**, 563–580 (2018).

68. Zhu, W. *et al.* Application of Operando X-ray Diffraction and Raman Spectroscopies in Elucidating the Behavior of Cathode in Lithium-Ion Batteries. *Front. Energy Res.* **6**, 1–16 (2018).

69. Pietsch, P. & Wood, V. X-Ray Tomography for Lithium Ion Battery Research: A Practical Guide. *Annu. Rev. Mater. Res.* **47**, 451–479 (2017).

70. Tao, H. *et al.* Effect of adding various carbon additives to porous zinc anode in rechargeable hybrid aqueous battery. *J. Alloys Compd.* **658**, 119–124 (2016).

71. Li, W. *et al.* Advanced Low-Cost, High-Voltage, Long-Life Aqueous Hybrid Sodium/Zinc Batteries Enabled by a Dendrite-Free Zinc Anode and Concentrated Electrolyte. *ACS Appl. Mater. Interfaces* **10**, 22059–22066 (2018).

72. He, P. *et al.* Layered VS 2 Nanosheet-Based Aqueous Zn Ion Battery Cathode. *Adv. Energy Mater.* **7**, 1–5 (2017).

73. Tang, B. *et al.* Potassium vanadates with stable structure and fast ion diffusion channel as cathode for rechargeable aqueous zinc-ion batteries. *Nano Energy* **51**, 579–587 (2018).

74. Wan, F. *et al.* Aqueous rechargeable zinc/sodium vanadate batteries with

enhanced performance from simultaneous insertion of dual carriers. *Nat. Commun.* **9**, 1–11 (2018).

75. Liu, J. *et al.* Advanced Energy Storage Devices: Basic Principles, Analytical Methods, and Rational Materials Design. *Adv. Sci.* **5**, (2018).

76. Wang, J., Polleux, J., Lim, J. & Dunn, B. Pseudocapacitive contributions to electrochemical energy storage in TiO 2 (anatase) nanoparticles. *J. Phys. Chem. C* **111**, 14925–14931 (2007).

77. Jiang, Y. & Liu, J. Definitions of Pseudocapacitive Materials: A Brief Review. *Energy Environ. Mater.* **2**, 30–37 (2019).

78. Gao, H., Li, Y., Park, K. & Goodenough, J. B. Sodium extraction from NASICON-structured Na3MnTi(PO4)3 through Mn(III)/Mn(II) and Mn(IV)/Mn(III) redox couples. *Chemistry of Materials* **28**, 6553–6559 (2016).

79. Electricity, July 5, 2018, C*oal use inches lower as solar, wind and diesel ris*e, accessed 03 March 2020,<http://www.statssa.gov.za/?p=11292>

80 Pastiche Energy Solutions ISO9001:2008 Certified Company, accessed 03 March 2020, <http://www.pasticheenergysolutions.com/applications/ >

81. IMD Shield, Securing Implantable medical devices, *wireless implantable devices,* accessed 03 March 2020 , a: https://groups.csail.mit.edu/netmit/IMDShield/images/WIMD.png

82. Circuitsify, Embedded Systems: Concept Definition, accessed 03 March 2020, ,<https://encryptedtbn0.gstatic.com/images?q=tbn:ANd9GcRyN8LjJtVaZT8rW2PfvNtFi6nxMOu71sXt4EV2cIvsoTa1q6wa&s>

83. Tesla, Less Than the Cost of Gas Model S, accessed 03 March 2020, <https://media.bizj.us/view/img/10433046/section-supercharger-alt2x*750xx1778-1000-551-0.jpg >

84. C&EN, Plastic maker plot the future of the car, Volume 95, Issue 45, November 2017, accessed 03 March 2020, <https://cen.acs.org/articles/95/i45/Plastics-makers-plot-future-car.html >

85. Electrical Energy, Solar SEG-Smart Export Guarantee, accessed 03 March 2020,<http://climatechangetheneweconomy.com/wpcontent/uploads/2017/08/grid-energy-storage.jpg>

86. Hyperphysics, Bragg's Law, accessed 03 March 2020, < http://hyperphysics.phy-astr.gsu.edu/hbase/quantum/bragg.html>

87. Nanoscience, Scanninh electron microscopy, accessed 03 March 2020, <https://www.nanoscience.com/techniques/scanning-electron-microscopy/>

88. GlobalSino, Schematic diagram of TEM systems, , https://www.globalsino.com/EM/page4554.html

89. MTI Corporation, accessed 03 March 2020, <https://cdn11.bigcommerce.com/s-wepv6/images/stencil/1280x1280/products/499/3637/Slayt4__46839.1562749713.JPG?c=2?imbypass=on>

90. Michael Root, The Tab Battery Book, An In-Depth Guide to Construction, Design and Use, 2010, McGraw Hill books

91. A Brginners Guide to XPS, 2017, Teignmouth Sceince and Technology Centre

92. D.J.O'Connor, B.A.Sexton, R.St.CSmart, *Surface Analysis Methods in Materials Science*, Springer Series in Surface Sciences

93. ElPROCUS Overview of smart grid technology and its operation and application (for existing power system), viewed February 2020 https://www.elprocus.com/overview-smart-grid-technology-operation-application-existing-power-system/

94. NASA Visible earth, a catalog of NASA images and animations of our home planet, viewed February 2020, Ref to be included: Source: NASA VISIBLE EARTH, Earth Lights, visualization date: October 23, 2000, accessed 03 March 2020, <https://visibleearth.nasa.gov/view.php?id=55167>

95. SOLARGIS, 2017, Solar resource maps of Sub-Saharan Africa, World Bank, solar resource data, accessed 03 March 2020, <https://solargis.com/maps-and-gis-data/download/sub-saharan-africa>

96. Global energy library, 2000, Wind Energy Potential in Africa, accessed 03 March 2020,<https://www.geni.org/globalenergy/library/renewable-energy-resources/world/africa/wind-africa/index.shtml>

97. ALJAZEERA, 20 February 2018, mapping Africa's natural resources, accessed 03 March 2020, <https://www.aljazeera.com/indepth/interactive/2016/10/mapping-africa-natural-resources-161020075811145.html >